Combined Quartz Crystal Microweighing and Surface Plasmon Spectroscopy:

Comparison of Acoustic and Optical Properties of Polymer Interfaces

---

Dissertation
zur Erlangung des Grades eines Doktors
der Naturwissenschaften
vorgelegt von

Zhehui Wang
aus Shandong/China

genehmigt von der
Mathematisch-Naturwissenschaftlichen Fakultät
der Technischen Universität Clausthal
Tag der mündlichen Prüfung
02.07.2004

Die vorliegende Arbeit wurde am Max-Planck-Institut für Polymerforschung zu Mainz und am Institut für Physikalische Chemie der Technischen Universität Clausthal anfertigt.

Vorsitzender der Promotionskommission: Prof. Dr. D.Mayer

Hauptberichterstatter: Prof. Dr. D. Johannsmann

Berichterstatter: PD Dr. J. Adams

Acknowledgements

I want to thank the people, who supported me and contributed to my work both scientifically and personally.

Thank you to:

- My adviser Prof. D. Johannsmann, who provided the interesting topics, a forum for discussion and tutorship during my whole doctoral education.
- Prof. W. Knoll, who gave me the chance to get doctoral education in his group inside Max-Planck Institute for Polymer Research (MPIP) in Mainz.
- Dr. S. Berg, for tutorship, helpful discussions, computer work and team spirit.
- B. Menges, for help and tutorship in making corrugational gratings on the surface of quartz crystals in clean room of MPIP in Mainz.
- K. Petersen, for AFM pictures of quartz surface gratings in MPIP.
- G. Hermann, for help and tutorship in laboratory technique and room temperature evaporation of Cr, Au, Ag, and Al in MPIP in Mainz.
- A. Baba, A. Bund, J. Luebben, and S.Tian, for team work in electrochemistry.
- Dr. D. Kuckling, who provided photo cross-linkable pNIPAm samples.
- Mark Plunkett, for team work in adsorption of linear pNIPAm on gold surface.
- Anne K. Aliganga, for team work in deposition of mercury on self assembled monolayer on gold surface and the corresponding AFM pictures.
- Mr. Richter and the electronics workshop in MPIP, for all the discussions and helps about temperature controlling.
- Mr. Gesternberg and the mechanics workshop in MPIP, for all the helps about manufacturing all the liquid cells used in my measurements.
- Mr. Werner and Mr. Koch in mechanics workshop in Clausthal, for all the helps in the installation of my setup in Clausthal.
- Katrin Wondraczek, Ilshat Gubaidullin, Volker Dehnke, and many others in Clausthal, who helped me in settling down in Clausthal.

Kombination von Schwingquarz-Mikrowaage und Oberflächen-Plasmonen-Spektroskopie: optische und akustische Eigenschaften von dünnen Polymerfilmen

Zhehui Wang
- Kurzfassung der Dissertation -

Mit der Schwingquarz-Mikrowaage (quartz crystal microbalance, "QCM") wird die Masse von dünnen, an Oberflächen gebundenen Filmen bestimmt. Gleichzeitig liefert diese Technik Informationen über die viskoelastischen Eigenschaften der Filme. Auf diesem Wege lassen sich Strukturänderungen in Echtzeit verfolgen. Bei der Adsorption von Polymerfilmen in flüssiger Umgebung schließt die mit der QCM bestimmte "akustische Dicke" gebundenes Lösungsmittel mit ein. Die adsorbierte Menge (ohne mitgeführte Flüssigkeit) ist deshalb oft schwer zu bestimmen. Um die Messungen besser interpretieren zu können, wurden kombinierte optische und akustische Messungen mittels Oberflächen-Plasmonen-Resonanz (surface plasmon resonance, "SPR") und Schwingquarz-Mikrowaage durchgeführt.

Um die Erzeugung von Oberflächenplasmonen auf der Gold-Elektrode des Quarzes zu ermöglichen, wurde auf photolithographischem Weg ein optisches Gitter auf dieser Oberfläche erzeugt. Es zeigte sich, dass die beste Koppeleffizienz bei einer Gitterkonstante von 520 nm und einer vertikalen Amplitude von 25 – 40 nm (peak-to-peak) erreicht wird. Mit derart modifizierten Quarzscheiben können SPR Messungen und QCM Messungen an ein- und derselben Probe in-situ kombiniert werden. Während die Scherbewegung des Quarzes keinen Einfluss auf die Bestimmung der optischen Schichtdicke hat, zeigt sich ein kleiner Einfluss der Laserstrahlung auf die Resonanzfrequenz des Quarzes. Dieser Einfluss wird einem Temperatur-Effekt in Kombination mit der Relaxation von Spannungen in den Elektroden zugeordnet.

Der Nutzen dieser Apparatur wurde an drei verschiedenen Experimenten demonstriert:

- *Adsorption von Poly-(N-isopropyl-acrylamid) (pNIPAm) auf Gold Oberflächen.*
  Die Adsorption von linearem pNIPAm auf einer Gold Oberfläche wurde bei 31°C mit QCM und SPR untersucht. Der SPR Koppelwinkel (optische Dicke) und die Frequenzverschiebung (akustische Dicke) steigen in etwa proportional zu einander an. Die Dissipationsänderung ist ebenfalls in etwa proportional zur Frequenzverschiebung. Diese Ergebnisse widersprechen der intuitiven Vorstellung, dass sich zunächst eine verdünnte Polymerlage mit einer Dicke entsprechend dem Knäueldurchmesser bildet, welche sich später verdichtet. In diesem Fall würde man erwarten, dass die akustische Dicke und die Dämpfung zunächst stark ansteigen und dann in etwa konstant bleiben, während die optische Dicke weiter ansteigt. Die Ergebnisse sprechen im Gegenteil für ein Lagenwachstum, bei dem die Polymerkonzentration in der Schicht konstant ist und die Schichtdicke wächst.
- *Temperatur-induzierte Quellung und Entquellung von vernetzten pNIPAm-Gelen in Wasser.*
  Es zeigt sich der erwartete Quellungsübergang bei etwa 33°C, der dem im Bulk beobachteten Kettenkollaps entspricht. Die Optimierung des Vernetzungsgrades im Hinblick auf sensorische Anwendung wurde untersucht.
- *Elektropolymerisation und Doping / Dedoping Verhalten von leitenden Polymerschichten.*
  Am Beispiel von Polyanilin und Polypyrrol wurde gezeigt, dass sich auch die Elektropolymerisation mit dieser Technik verfolgen lässt. Der Film-Brechungsindex ändert sich stark bei variiertem Potential.

Contents

1 INTRODUCTION

The increasing thin polymer film applications have spurred a surge of activities aimed at improving our understanding of their properties. The structure and dynamics of polymers on the mesoscopic scale have increasingly come into the focus of scientific interest in the past years. The use of polymer or other organic thin films deposited onto solid samples constitutes a considerable challenge for the experimentalist in aiming at characterizing the properties of these coatings, because the systems we concern with are, in some cases, only a monomolecular layer thick. Polymers in thin film configurations have different physical properties from those of the bulk material due to interfacial interactions and molecular confinement. This means that extremely sensitive experimental techniques are required that allow the measurement and evaluation of these structural and dynamic changes in thin samples and the determination of how these variations modify their various thermal, mechanical, electrical and optical properties.

The Quartz Crystal Microbalance (QCM) [LC84] [Sch90] [Joh99] and SPR (surface plasmon resonance) spectroscopy [Kno91] [AIS^{+}94] are common techniques for measuring film thicknesses in the range of a few monomolecular layers. Both techniques are based on the reflection of a wave at the substrate–film interface and share common principles. [HKN^{+}] The existence of standing waves in the layer system defines a resonant condition (frequency or coupling angle), the shift of which is used to probe film thickness growth.

The QCM is designed to measure the mass as well as the viscoelastical properties of thin films deposited onto its electrode surface. It is used to monitor the structural changes of thin films in situ during physical and chemical changes. However, since the acoustic thickness of polymer films inside liquid measured by QCM technique contains a certain amount of solvent; the exact amount of polymer adsorbed onto the electrode surface is usually difficult to be determined by QCM technique. In order to get a better understanding of the QCM measurements, we use a combined QCM and SPR measurement technique. SPR spectroscopy measures the optical film thickness, and it can provide more information. If the refractive index of the dry film material is constant, even if the film swells in solvent, i.e. the film contains much more solvent, its refractive index of the total film shall also change, and the optical thickness shall remain about the same level. Swelling therefore effectively increases the acoustic thickness, while it affects the optical thickness to a much lesser degree.

The following work was finished during my Ph. D. period:

(1) Make shallow gratings with 520 nm in period and 25 -40 nm in depth on bare quartz wafer surfaces using photolithographic technique in clean room;

(2) Measure elastic shear modulus of evaporated metal films like gold and silver on QCM surface using bare quartz crystal wafer excited across an air gap;

(3) Monitor chitosan film swelling in different pH buffer solutions using combined QCM and SPR techniques: the measured optical thickness decreases with pH rise, while the acoustic thickness measurement shows a maximum value at a middle pH value;

(4) Detect the adsorption of mercury vapor on thiol covered gold surface and monitor the freezing and melting process of mercury droplets using QCM: around phase transformation, there is a strong noise signal in quartz damping measurement;

(5) Measure the adsorption process of linear pNIPAm on gold surface in water at 31°C: acoustic and optical thicknesses increase in parallel, which shows that the polymer concentration inside the film is constant during film growth;

(6) Measure the temperature effect on cross linked pNIPAm film in water using combined QCM and SPR techniques: pNIPAm gel collapses above ca. 33°C;

(7) Electrochemical polymerization of polypyrrol and polyaniline films on gold surfaces and their properties studied by SPR and QCM techniques: film refractive index have a large jump when they undergo a transfer from reduced state to oxidized state;

(8) Multilayer formation of polyelectrolyte PSS/PAA using traditional layer by layer method detected by combined QCM and SPR techniques: acoustic thickness as well as optical thickness increase in parallel.

2 THEORETICAL BACKGROUNDS

2.1 Quartz Crystal Microbalance

2.1.1 QCM introduction

Quartz Crystal Microbalance (QCM), based on coin-shaped or square shaped quartz crystals onto which metallic electrodes are evaporated, has played important roles in probing interfacial processes at surfaces and thin films. The operation of QCM relies on an alternating strain field induced by an alternating electric field applied across the quartz wafer due to piezo-effect. For an AT-cut quartz crystal thickness shear mode this acoustic vibration results in the propagation of a transverse acoustic wave across the crystal thickness. The QCM resonance frequency decreases with increasing crystal thickness according to equation (2.1.1.1).

$$f_0 = \frac{v}{\lambda} = \frac{v}{2t_q} \tag{2.1.1.1}$$

$$v = \sqrt{\frac{G_q}{\rho_q}} \tag{2.1.1.2}$$

with f_0 the fundamental frequency, λ wavelength and ν the velocity of sound in the quartz crystal, and t_q is the crystal thickness. The velocity ν is given in equation (2.1.1.2), where ρ_q and G_q are the density (ρ_q = 2.648×10³ kg/m³) and shear modulus (G_q = 29.47 GPa) of the quartz material. The calculated sound velocity is ν = 3350 m/s. For a quartz crystal with a fundamental frequency of 5 MHz, its calculated thickness is 0.335 mm. This mode of thickness shear motion does not radiate longitudinal sound into the ambient medium. Only odd harmonics can be excited electrically because the integral polarization between the electrodes vanishes for symmetric strain patterns.

When the thickness of QCM plate increases due to the addition of a film the resonance frequency decreases according to Sauerbrey equation,

$$\frac{f - f_n}{f_n} = -\frac{\delta m}{m_q} = -\frac{2f_0}{Z_q}\delta m \tag{2.1.1.3}$$

where $f - f_n$ is the frequency shift in n-th harmonic overtone, f_n is the n-th reference resonance frequency, δm is the deposited mass per unit area, m_q is the mass of the quartz plate per unit area, the acoustic impedance of AT-cut quartz Z_q = 8.8×10^6 kg/m²s . The Sauerbrey equation

holds for films in air, provided that the film thickness is much smaller than the sound wavelength.

2.1.2 Derivation of a generalized Sauerbrey equation for films in liquids[1]

For more complicated situations one has to resort to acoustic modeling. We first rephrase eqn. 2.1.1.3, still assuming that the quartz is operated in air and that the acoustic properties of the film are the same as those of the quartz. One can then easily see that the fractional decrease in frequency is equal to the fractional increase in thickness of the quartz–film composite resonator. Using the wave picture, one can derive that the fractional frequency shift $\delta f/f$ is proportional to the phase shift $\delta\varphi = 2\, k_f\, d_f$ acquired by the shear wave as it passes through the film (Fig. 2.1):

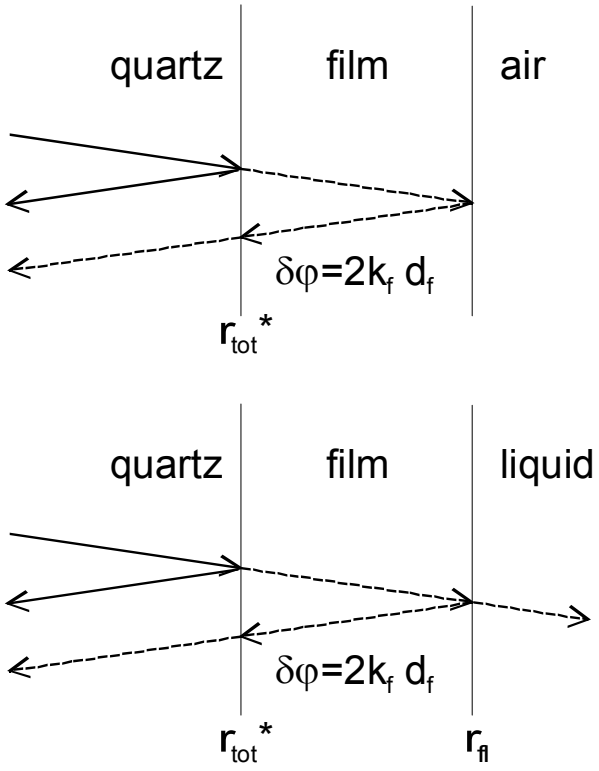

Figure 2.1: Schematic description of the acoustic model underlying the calculation of complex frequency shifts.

$$\frac{\delta f}{f} = -\frac{\delta\varphi}{2\pi} = -\frac{2\, k_f\, d_f}{2\pi} \qquad (2.1.2.1)$$

Here k is the wave number, d is the thickness, and the index f labels the film.

[1] Partly adapted from: M.A. Plunkett, Z. Wang, M.W. Rutland, D. Johannsmann Adsorption of pNIPAm layers on hydrophobic gold surfaces, measured in-situ by QCM and SPR Langmuir 19 (2003) 6837.

In case the film's acoustic impedance is not the same as that of the quartz, one has to consider two reflected waves: the first one reflected at the quartz –film interface and the second reflected at the film –air interface. The complex coefficient of reflectivity, r, at an interface is given by $r = (Z_1 - Z_2) / (Z_1 + Z_2)$, where Z_1 and Z_2 are the acoustic impedances of the two materials. One can calculate an overall reflectivity at the quartz –film interface, r_{tot}, either by the matrix formalism or by an iteration procedure as described in Ref. [AB87]. The calculation proceeds in exactly the same way as the calculation of reflectivity of optical multilayers, where the acoustic impedance takes the role of the refractive index. It turns out that the fractional frequency shift is given by:

$$\frac{\delta f^*}{f} \approx \mathrm{i}\,\frac{r_{tot}^* - 1}{2\pi} \qquad (2.1.2.2).$$

The asterisk (*) indicates complex quantities, where the complex resonance frequency is given by $f + i\,\Gamma$, with Γ the half-band-half-width. Eqn. 2.1.2.2 is more general than eqn. 2.1.2.1. It accounts for impedance mismatch and dissipation in the film. For thin films, the imaginary part of the reflection coefficient is the phase φ. In this limit eqn. 2.1.2.1 is recovered.

An alternative treatment of the frequency shift in quartz resonators is possible in the frame of equivalent circuits and the transmission line theory. In this context it is helpful to define generalized impedance via the relation

$$r^* = \frac{Z_q - Z^*}{Z_q + Z^*} \qquad (2.1.2.3)$$

Eqn. 2.1.2.3 is the usual condition for the reflection coefficient at interfaces with an impedance mismatch. If the medium contacting the quartz surfaces is a semi-infinite liquid, then Z^* is just the acoustic impedance of this liquid $Z_l = Z^* = (i\,\omega\rho\eta)^{1/2}$. For more complicated situations, namely layer systems, one defines Z^* as the ratio of stress, σ, and lateral speed, $\partial u/\partial t$ just above the quartz surface. Here $u(z, t)$ is the displacement pattern of the acoustic wave. Z^* is *not* a material property like the acoustic impedance. It is defined in analog to the electrical impedance, where stress takes the role of voltage and lateral speed takes the role of current. For a given equivalent circuit, Z^*, is calculated from the individual circuit elements by application of the Kirchhoff rules. [Ros88] Inserting eq. 2.1.2.3 into eqn. 2.1.2.2 and assuming $Z_q >> Z^*$ (which is true for most organic adsorbates) one finds

$$\frac{\delta f}{f_0} = \frac{i}{\pi}\frac{Z^*}{Z_q} \qquad (2.1.2.4)$$

Eqn. 2.1.2.4 is also proven by application of the Thiersten equivalent circuit [Thu84] in ref. [JMW+92]. This leaves the problem of calculating the ratio of stress, σ, and the lateral speed, $\partial u/\partial t$ just above the quartz surface for a viscoelastic film in a liquid. We write

$$\begin{aligned} Z^* &= \frac{\sigma}{\partial u/\partial t} = \frac{G_f\,\partial u/\partial z}{\partial u/\partial t} = \frac{G_f\,k\left(u^+ - u^-\right)}{\omega\left(u^+ + u^-\right)} \\ &= \frac{G_f\,k\left(1 - u^-/u^+\right)}{\omega\left(1 + u^-/u^+\right)} = Z_f \frac{\left(1 - \exp\left(-2\mathrm{i}\,k_f d_f\right)\dfrac{Z_f - Z_l}{Z_f + Z_l}\right)}{\left(1 + \exp\left(-2\mathrm{i}\,k_f d_f\right)\dfrac{Z_f - Z_l}{Z_f + Z_l}\right)} \\ &= Z_f \frac{\left(Z_f + Z_l\right)\exp\left(2\mathrm{i}\,k_f d_f\right) - \left(Z_f - Z_l\right)}{\left(Z_f + Z_l\right)\exp\left(2\mathrm{i}\,k_f d_f\right) + \left(Z_f - Z_l\right)} \end{aligned} \qquad (2.1.2.5)$$

Here G_f is the shear modulus of the film. u^+ and u^- are amplitudes of the waves traveling in the forward and the backward direction. The indices *f* and *l* denote the film and the liquid, respectively. The term $(Z_f - Z_l) / (Z_f + Z_l)$ is the reflectivity of the film–liquid interface. The factor $\exp(-2i\,k_f d_f)$ accounts for the travel across the film. In the second line we have used $G_f\,k_f / \omega = G_f(\rho_f/G_f)^{1/2} = (\rho_f G_f)^{1/2} = Z_f$. With Eqn. 2.1.2.4 this translates to

$$\frac{\delta f^*}{f_0} = \frac{i}{\pi}\frac{Z^*}{Z_q} = \frac{i}{\pi}\frac{Z_f}{Z_q}\frac{\left(Z_f + Z_l\right)\exp\left(2\mathrm{i}\,k_f d_f\right) - \left(Z_f - Z_l\right)}{\left(Z_f + Z_l\right)\exp\left(2\mathrm{i}\,k_f d_f\right) + \left(Z_f - Z_l\right)} \qquad (2.1.2.6)$$

Eqn. 2.1.2.6 predicts the complex frequency shift for films of arbitrary thickness in liquids. In case the film is much thinner than the wavelength of sound ("long-wavelength-limit") one may linearize the exponential and write

$$\begin{aligned} \frac{\delta f^*}{f_0} &\approx \frac{i}{\pi}\frac{Z_f}{Z_q}\frac{\left(Z_f + Z_l\right)\left(1 + 2\mathrm{i}\,k_f d_f\right) - \left(Z_f - Z_l\right)}{\left(Z_f + Z_l\right)\left(1 + 2\mathrm{i}\,k_f d_f\right) + \left(Z_f - Z_l\right)} \\ &\approx \frac{i}{\pi}\frac{Z_f}{Z_q}\frac{\left(Z_f + Z_l\right)\mathrm{i}\,k_f d_f + Z_l}{\left(Z_f + Z_l\right)\mathrm{i}\,k_f d_f + Z_f} \\ &\approx \frac{i}{\pi}\frac{Z_f}{Z_q}\frac{\left(Z_l + \left(Z_f + Z_l\right)\mathrm{i}\,k_f d_f\right)\left(Zf - \left(Z_f + Z_l\right)\mathrm{i}\,k_f d_f\right)}{Z_f^2} \\ &\approx \frac{i}{\pi}\frac{Z_l}{Z_q} + \frac{i}{\pi}\frac{Z_f}{Z_q}\frac{\left(Z_f - Z_l\right)\left(Z_f + Z_l\right)\mathrm{i}\,k_f d_f}{Z_f^2} \\ &\approx \frac{i}{\pi}\frac{Z_l}{Z_q} - \frac{\omega m_f}{\pi Z_q}\frac{{Z_f}^2 - {Z_l}^2}{Z_f^2} \end{aligned} \qquad (2.1.2.7)$$

In the last line we have used $Z_f k_f d_f = (\rho_f G_f)^{1/2} \omega (\rho_f / G_f)^{1/2} d_f = \omega m_f$. The first term in eqn. 2.1.2.7 is the frequency shift induced by the presence of the liquid. It is absent when the quartz in liquid is chosen as the reference state (assuming that the liquid used for reference has the same viscosity as the liquid used in the experiment).

2.2 Surface Plasmon Resonance (SPR) Spectroscopy[2]

An interface in the x,y-plane between two half-infinite spaces, 1 and 2, of materials is described optically by their complex frequency dependent dielectric functions $\varepsilon_1(\omega)$ and $\varepsilon_2(\omega)$, respectively. Surface polaritons can only be excited at an interface if the dielectric displacement **D** of the electromagnetic mode has a component normal to the surface (i.e. parallel to z) that can induce a surface charge density σ.

$$(D_2 - D_1) \cdot z = 4\pi\sigma \qquad (2.2.1)$$

S-polarized light propagating along the x-direction possesses only electric field components, $\mathbf{E}_i$, parallel to the surface (parallel to the y-direction), i.e. transverse electric (**TE**) waves have **E**=(0, Ey, 0), hence are unable to excite surface polaritons. Only p-polarized light (transversal magnetic, **TM**) modes with **E**= (Ex, 0, Ez) or, equivalently, the magnetic component, **H**= (0, Hy, 0), can couple to such surface plasmon modes.

The resulting surface electromagnetic wave, therefore, will have the following general form:

$$A_1 = A_{10} \exp i(k_{x1} x + k_{z1} z - \omega t) \quad \text{in medium 1} \quad (2.2.2a)$$

$$A_2 = A_{20} \exp i(k_{x2} x + k_{z2} z - \omega t) \quad \text{in medium 2} \quad (2.2.2b)$$

where **A** stands for **E** and **H**; k_{x1} and k_{x2} are the wave vectors in the x-direction; k_{z1} and k_{z2} those in z-direction, i.e. normal to the interface; and ω is the angular frequency. Both fields must fulfill the Maxwell equations:

$$\nabla \cdot H = 0 \qquad (2.2.3)$$

$$\nabla \cdot E = 0 \qquad (2.2.4)$$

$$\nabla \times E + \frac{1}{c} \frac{\partial H}{\partial t} = 0 \qquad (2.2.5)$$

[2] Partly adapted from: E.F. Aust, S. Ito, M. Sawodny and W. Knoll, Investigation of Polymer Thin Films Using Surface Plasmon Modes and Optical Waveguide Modes Trends in Polymer Science, TRIP vol. 2 No.9 **(1994)** 313.

$$\nabla \times H - \frac{\varepsilon}{c}\frac{\partial E}{\partial t} = 0 \qquad (2.2.6)$$

where c is the speed of light in vacuum and ε the material dielectric function. The tangential components of **E** and **H** have to be equal at the interface, that is:

$$E_{x1} = E_{x2} \qquad (2.2.7)$$

$$H_{y1} = H_{y2} \qquad (2.2.8)$$

From eqn. 2.2.7 it follows that $k_{x1}=k_{x2}=k_x$. On the other hand, from Eqn. 2.2.2 and 2.2.6 it follows that:

$$k_{z1}H_{y1} = \frac{\omega}{c}\varepsilon_1 E_{x1} \qquad (2.2.9)$$

and

$$k_{z2}H_{y2} = -\frac{\omega}{c}\varepsilon_2 E_{x2} \qquad (2.2.10)$$

This only leads to a nontrivial solution if

$$\frac{k_{z1}}{k_{z2}} = -\frac{\varepsilon_1}{\varepsilon_2} \qquad (2.2.11)$$

It shows that surface electromagnetic modes can only be excited at interfaces between two media with dielectric constants of opposite sign. For the coupling of collective plasma oscillations of the nearly free electron gas in a metal to an electromagnetic field, according to Drude model, [Gro79] these excitations result in a strongly negative dielectric function for metals with ε_m.

$$\varepsilon_m = 1 - \frac{\omega_p^2}{\omega^2} \qquad (2.2.12)$$

ε_m is negative from ω=0 throughout the visible range up to a maximum frequency given by:

$$\omega_{max} = \omega_p \qquad (2.2.13)$$

where ω_p is the plasma frequency of the metal and is typically in the deep UV range.

At interface between a metal (with complex dielectric function $\varepsilon_m = \varepsilon_m' + i\,\varepsilon_m''$) and a dielectric material ($\varepsilon_d = \varepsilon_d' + i\,\varepsilon_d''$), we obtain from eqns. 2.2.5, 2.2.6, 2.2.9 and 2.2.10:

$$k_x^2 + k_{zd}^2 = (\frac{\omega}{c})^2 \varepsilon_d \qquad \text{or} \quad k_{zd} = \sqrt{\varepsilon_d (\frac{\omega}{c})^2 - k_x^2} \qquad (2.2.14)$$

With Eqn 1.2.11 this leads to the dispersion relationship (i.e. energy momentum relation) for plasmon surface polaritons (PSPs) at a metal-dielectric interface:

$$k_x = \frac{\omega}{c}\sqrt{\frac{\varepsilon_m \cdot \varepsilon_d}{\varepsilon_m + \varepsilon_d}} \qquad (2.2.15)$$

In the usual treatment, ω is taken to be real; since $\varepsilon_m = \varepsilon_m' + i\,\varepsilon_m''$ is complex, $k_x = \frac{\omega}{c}\sqrt{\frac{\varepsilon_m \cdot \varepsilon_d}{\varepsilon_m + \varepsilon_d}}$ is also complex: $k_x = k_x' + i\,k_x''$. [RK88] As a consequence, PSP waves propagating along a metal-dielectric interface exhibit a finite propagation length, L_x, given by $L_x = 1/k_x''$.

In the frequency (spectral) range of interest, we have

$$\sqrt{\frac{\varepsilon_m \cdot \varepsilon_d}{\varepsilon_m + \varepsilon_d}} \geq \varepsilon_d \qquad (2.2.16)$$

Eqns 2.2.14 and 2.2.16 show that the z-component of the PSP wave vector is purely imaginary. From Eqn 2.2.2 we see that the surface plasmon is a bound, nonradiative evanescent wave with a field amplitude, the maximum of which is at the interface ($z = 0$) and is exponentially decaying into the dielectric (and into the media). Propagation is as a damped oscillatory electromagnetic mode along the x-direction, coupled to a surface charge density wave. Eqn 2.2.16 shows that the momentum of a free photon, k^{ph} propagating in a dielectric medium, according to equation 2.2.17 is always smaller than the momentum of a surface plasmon waves propagating along an interface between the same medium and metal (Fig. 2.2).

$$k^{ph} = \frac{\omega}{c}\sqrt{\varepsilon_d} \qquad (2.2.17)$$

The dispersion of photons is described by the light line, $\omega = c_d k$ (fig.2.2, curve a), with $c_d = c/\sqrt{\varepsilon_d}$. For the excitation of surface plasmons only the projection of photon wave vector onto the x-direction is the relevant parameter. For a simple reflection of photons (with energy $\hbar\omega_L$, i.e. from a laser) at a planar dielectric-metal interface, this means that by changing the angle of incidence θ, $k_x^{ph} = k^{ph} \sin\theta$ can be tuned from zero at normal incidence (point 1 in Fig. 2.2) to the full wave vector k^{ph} at grazing incidence (point 2 in Fig.2.2). Eqns. 2.2.15 and 2.2.16 tells us that it is not always possible to fulfill, in addition to the energy conservation, the momentum matching condition for resonant PSP excitation because, for very low energies, the PSP dispersion curve (Fig.2.2 curve b) asymptotically approaches the light line

(curve a), whereas for higher energies, it approaches the cutoff angular frequency, ω_{max}. In any way the PSP wave vector is too large. There are two ways to overcome this problem: one way is using a prism. Photons are not directly coupled to the metal-dielectric interface, but via the evanescent tail of light total internally reflected at the base of the high index prism (with $\varepsilon_p > \varepsilon_d$). This light is characterized by a larger momentum (curve c) which, for a certain spectral range, can exceed the momentum of the PSP to be excited at the metal surface. So by choosing the appropriate (inner) angle of incidence θ_0 (see point 3), resonant coupling between evanescent photons and surface plasmons can be obtained.

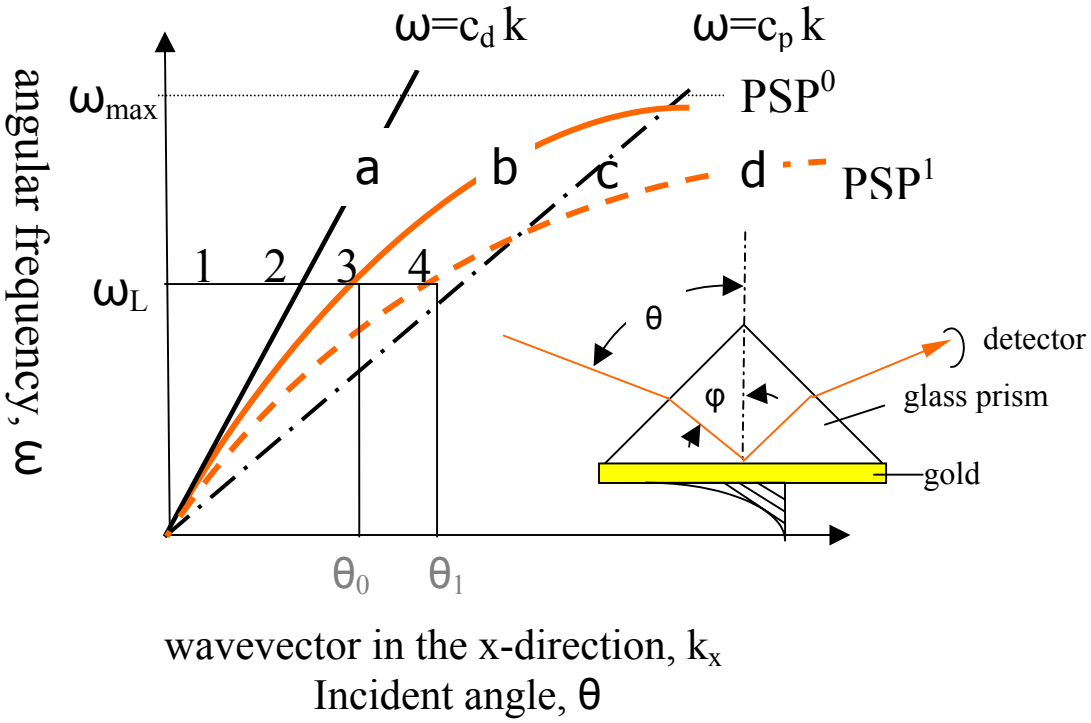

Figure 2.2: Dispersion relation: angular frequency ω versus wavevector in the x-direction k_x, of PSPs at a metal-dielectric (e.g. air) interface (PSP^0, curve b) and at a metal-coating-dielectric interface (PSP^1, curve d), respectively. Given also are the light lines of photons propagating in the bulk dielectric material ($\omega = c_d k$, curve a) and in a prism material ($\omega = c_p k$, curve c). Laser light of energy $\hbar\omega_L$ couples to PSP states at angles θ_0 and θ_1 (points 3 and 4, respectively), given by the energy- and momentum–matching condition. (In the right lower corner is the Kretschmann configuration with a ~50 nm thick metal film for PSP excitation.)

The most widespread technique for surface plasmon spectroscopy is based on the experimental configuration introduced by Kretschmann. (see Fig. 2.2) In Kretschmann

configuration, a very thin metal layer (typically ~45 – 50 nm) is evaporated onto the base of the prism, and the high momentum photons in the prism couple through this metal layer to the PSP states at the other side in contact with the dielectric medium.

Another way to get resonant coupling between evanescent photons and surface plasmons is to use shallow gratings. For more information about diffraction gratings, see http://www.spectra-physics.com/eThermo/CMA/PDFs/Various/File_22446.pdf. Up to now, the mechanism of using gratings to get PSP coupling is not completely understood.

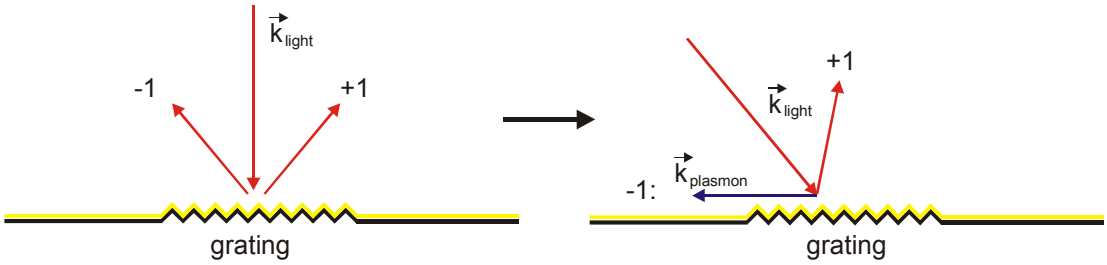

Figure 2.3: Schematic of refractive gratings in excitation of plasmon surface polaritons.

2.3 Combination of QCM and SPR[3]

Quartz Crystal Microbalance (QCM) is designed to measure the mass as well as the viscoelastical properties of thin films deposited onto its electric surface. We can use QCM to monitor the structural changes of thin films in situ during physical and chemical processes. However, the acoustic thickness of polymer films inside liquid measured by QCM technique contains certain amount of solvent; the exact amount of polymer adsorbed onto the electrode surface is usually difficult to be determined by QCM technique. In order to get a better understanding of the QCM measurements, we use a combined measurement technique, i.e. QCM and SPR (Surface Plasmon Resonance Spectroscopy).

We now turn to the influence of the presence of thin films. Provided that the layer is much thinner than the wavelength of light, [Lek78] the shift of the plasmon coupling angle is to first order in film thickness given by [Poc78]

$$\frac{n\omega}{c}\Delta(\sin\theta_c) = \Delta k_x \approx \frac{\omega}{c}\frac{2\pi}{\lambda}\left(\frac{\varepsilon_m\varepsilon_a}{\varepsilon_m+\varepsilon_a}\right)^2 \frac{1}{\sqrt{-\varepsilon_m\varepsilon_a}\left(\varepsilon_a-\varepsilon_m\right)} \frac{\left(\varepsilon_f-\varepsilon_a\right)\left(\varepsilon_f-\varepsilon_m\right)}{\varepsilon_f} d_f \qquad (2.3.1)$$

[3] partly adapted from: M.A. Plunkett, Z. Wang, M.W. Rutland, D. Johannsmann Adsorption of pNIPAm layers on hydrophobic gold surfaces, measured in-situ by QCM and SPR Langmuir 19 **(2003)** 6837.

with n the refractive index of the ambient medium, θ_c the coupling angle, ε the dielectric constant, d_f the film thickness, and λ the wavelength. The indices "a", "f" and "m" denote the ambient medium, the film, and the metal substrate, respectively. Eqn. 2.3.1 can be generalized to account for continuous refractive index profiles, for example created by a dilute adsorbate:

$$\Delta(\sin\theta_c) \approx \frac{2\pi}{n\lambda} \left(\frac{\varepsilon_m \varepsilon_a}{\varepsilon_m + \varepsilon_a}\right)^2 \frac{1}{\sqrt{-\varepsilon_m \varepsilon_a}\,(\varepsilon_a - \varepsilon_m)} \int_0^\infty \frac{(\varepsilon_f(z) - \varepsilon_a)(\varepsilon_f(z) - \varepsilon_m)}{\varepsilon_f(z)} dz \qquad (2.3.2)$$

where the integral is termed the "ellipsometric moment". This is the quantity determined in any technique based on optical reflectometry, including ellipsometry and SPR spectroscopy. When working with metal surfaces, one can further assume that $\varepsilon_f(z) - \varepsilon_m \approx \varepsilon_a - \varepsilon_m$ and pull this quantity out of the integral, leading to

$$\Delta(\sin\theta_c) \approx \frac{2\pi}{n\lambda} \left(\frac{\varepsilon_m \varepsilon_a}{\varepsilon_m + \varepsilon_a}\right)^2 \frac{1}{\sqrt{-\varepsilon_m \varepsilon_a}} \int_0^\infty \frac{\varepsilon_f(z) - \varepsilon_a}{\varepsilon_f(z)} dz \qquad (2.3.3)$$

We define the "optical thickness" d_{opt} as the thickness of an equivalent compact layer generating the same shift of the surface plasmon as the film under study. One has

$$d_{opt} = \Delta(\sin\theta_c) \left[\frac{\varepsilon_{dry} - \varepsilon_a}{\varepsilon_{dry}}\right]^{-1} \left(\frac{2\pi}{n\lambda} \left(\frac{\varepsilon_m \varepsilon_a}{\varepsilon_m + \varepsilon_a}\right)^2 \frac{1}{\sqrt{-\varepsilon_m \varepsilon_a}}\right)^{-1} \qquad (2.3.4)$$

where ε_{dry} is the dielectric constant of the adsorbate in its dry state. The parameters related to the film have been collected in the square brackets. The term in square brackets is a weight function, describing how strongly a film with a given thickness and dielectric constant affects the coupling angle.

Similar equations hold for quartz crystal resonators. In the long-wavelength-limit ($d_f << \lambda$, λ the wavelength of shear sound) one has

$$\frac{\delta f^*}{f} = -\frac{m_f}{m_q}\left[1-\left(\frac{Z_q^2}{Z_f^2}-1\right)\frac{Z_a^2}{Z_q^2}\right] \approx -\frac{m_f}{m_q}\left[1-\frac{Z_a^2}{Z_f^2}\right] = -\frac{m_f}{m_q}\left[\frac{Z_f^2-Z_a^2}{Z_f^2}\right] \qquad (2.3.5)$$

The quantity δf^* is the complex frequency shift $\delta f + i\,\delta\Gamma$, where f is the frequency and Γ is the half-band half-width. m_f and m_q are the mass per unit area of the film and quartz plate, respectively. One has the relation $m_q = Z_q / (2f_0)$ with f_0 the fundamental frequency. Z_a, Z_f, and Z_q are the acoustic impedances of the ambient medium (the liquid), the film, and the quartz, respectively. One has $Z_q = 8.8 \times 10^6\ kg\ m^{-2}\ s^{-1}$. The acoustic impedance is given by $Z = (\rho G)^{1/2}$ with ρ the density and G the shear modulus. The second line makes use of the relation $Z_q >> Z_f$, which is true for soft adsorbates. In soft matter experiments, G varies much stronger than ρ. The acoustic impedance is to a large extent governed by the material's shear modulus. For liquids one has $G = i\omega\eta$ with $\eta = \eta' - \eta''$ the viscosity. The acoustic impedance is the acoustic analog of the refractive index; Z is the analog of the dielectric constant. Because eqn. 2.3.5 is linear in mass, it also holds in an integral sense:

$$\frac{\delta f^*}{f} \approx -\frac{1}{m_q}\int_0^\infty\left[\frac{Z_f^2(z)-Z_a^2}{Z_f^2(z)}\right]\rho(z)\,\mathrm{d}z \approx -\frac{\rho}{m_q}\int_0^\infty\left[\frac{G_f(z)-G_a}{G_f(z)}\right]\mathrm{d}z \qquad (2.3.6)$$

The integral could be called "acoustic moment". The term in square brackets is again a weight function, describing how much a film of given thickness and acoustic impedance affects the resonance frequency. We define the acoustic thickness d_{ac} as the thickness of a hypothetical compact layer ($G_f >> G_a$) inducing the same frequency shift as the layer of interest:

$$d_{ac} = -\frac{\delta f}{f}\frac{m_q}{\rho} \qquad (2.3.7)$$

Eqn. 2.3.7 is the well-known Sauerbrey equation. [Sau64] The acoustic thickness is the Sauerbrey mass divided by the density of the film.

Comparing eqns. 2.3.4 and 2.3.7, one might assume that the information contained in surface plasmon resonances and quartz crystal resonances should be essentially the same. However, this is very often not the case. Firstly, the contrast in acoustics is usually much larger than that in optics. While refractive indices generally vary in the range of a few

percentages, the shear modulus may easily increase over orders of magnitude even for rather dilute adsorbates. In optics the weight function (square brackets in eqn. 2.3.4) is smaller than unity and roughly proportional to the concentration. Therefore, the plasmon shift is approximately proportional to the *adsorbed amount*. In acoustics, on the contrary, the weight function (square brackets in eqn. 2.3.6) easily saturates to a value of one even for dilute adsorbates if the shear modulus of the adsorbate is much higher than that of the liquid. [DPJ+97] The acoustic thickness reaches the *geometric thickness* at rather low coverage and does not increase much further upon densification of the film by prolonged adsorption. More pictorially speaking, if the adsorbate drags some solvent along in its shear movement, the trapped amount of solvent appears as a part of the film. [MSR93] Swelling therefore effectively increases the acoustic thickness, while it affects the optical thickness to a much lesser degree, see Fig. 2.4. As a side remark we note that a rough substrate can also lead to differences between optical and acoustic thickness though the effect of roughness should be small here.

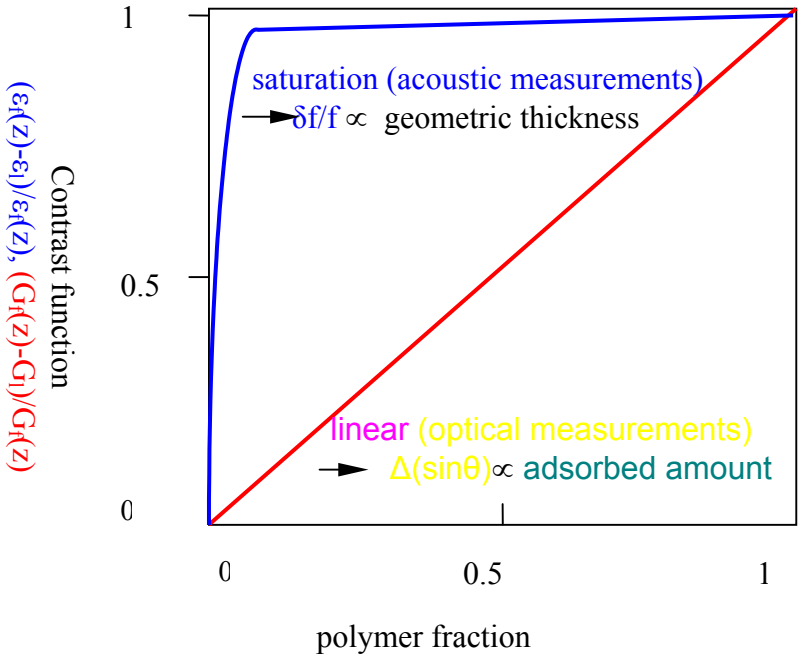

Fig. 2.4: Schematic comparison of optical and acoustic thickness of polymer films with different polymer content.

3 EXPERIMENTAL

An AT-cut quartz crystal with good gratings and evaporated gold electrodes on both sides is the fundamental part for combined measurement of QCM and SPR. The appropriate gratings are used to couple optical wave vector to produce surface plasmons, while the original quartz plate is for the QCM measurement.

3.1 Preparation of quartz wafer with shallow gratings

Blank quartz wafers were purchased from Maxtek Inc. (http://www.maxtekinc.com). To make gratings on a quartz surface, the following operations are performed:

(1) clean quartz wafers;

(2) evaporate a 10 nm thick chromium layer onto quartz surface;

(3) spin coat photo resist onto the chromium layer;

(4) make gratings into photo resist film (expose photo resist to laser beam interference pattern and develop this film);

(5) ion etching to transfer the grating pattern into the quartz wafer;

(6) electrode evaporation onto quartz surface.

The preparation of gratings on quartz surface requires an extremely clean environment; even very tiny dust may spoil the gratings, so the whole process is finished in a clean room of class 100.

3.1.1 Quartz plate cleaning procedure

A clean surface is very important for producing good gratings on a quartz surface. For new quartz wafers, it is easier to perform the cleaning process. The detailed procedure is:

- ultrasonic bath in 2%-Hellmanex for 15 min,
- rinse 15 times with MilliQ-water ,
- ultrasonic bath in 2%-Hellmanex for another 15 min,
- rinse 20 times with MilliQ-water;
- rinse 2 times with ethanol (or acetone, THF, cyclohexane, etc.)
- and dry with N_2.

For old quartz wafers with electrodes it is recommended to use chemical methods to remove gold and chromium first.

- An aqueous solution of iodine and potassium iodide (composition: I_2 : KI : H_2O = 10 : 40 : 50, weight ratio) is used for removing gold.
- Alternatively aqua regia (a 1:1 mixture of concentrated HCl (36%) and HNO_3 (65%) diluted in equal amount of Milli-Q water) can be used to remove gold and other kinds of metal, but not suitable for chromium.
- A freshly prepared aqueous solution of 2% ammonium cerium (IV) nitrate is used to remove chromium.

Usually it is not so easy to remove completely the metals from quartz surface, and it is recommended to repeat the metal removing procedure several times or use a long time of chemical treatment.

After the chemical cleaning process there should be no visible contamination on the quartz surface. Before chromium evaporation it is recommended to use plasma cleaning for 5 min.

3.1.2 Evaporation of a 5-10 nm thick chromium layer onto quartz surface

The purpose of this chromium layer is to improve the adhesion of the photo resist film to quartz surface, so that this film does not detach from the quartz surface during photo resist film development and ion etching. A much thicker chromium layer may increase the surface roughness of the quartz and make it difficult to prepare good gratings in the subsequent procedures.

3.1.3 Spin coating of photo resist film onto chromium layer

Photo resist S1805 (Microposit®, Shipley European Limited, U.K.) is recommended. This photo resist is diluted with EC-solvent (Microposit®, Shipley European Limited, U.K.) or Ma-T 1401 (Mikro-Technik Verduenner für Micro-negativ, MICRO TECHNIK GMBH, Berlin) in a ratio of 3 : 5, in order to get an appropriate film thickness. The photo resist film is spin coated onto the quartz surface with 10 nm thick chromium layer. The spinning parameters are 2500 rpm for 60 sec, and the acquired film thickness is 140 – 150 nm as measured using an α-profilometer. This photo resist film was then soft baked at 90°C for 30 minutes before it is exposed to laser beams.

3.1.4 Exposure of photo resist to laser beams.

He-Cd laser ($\lambda = 441.6\ nm$) is recommended. The laser power after adjustment should be larger than 1 mW/cm^2 as determined with a power meter after the pinhole. The grating constant g is calculated according to:

$$g = \frac{\lambda_{He-Cd}}{2\sin\alpha} \qquad (3.1)$$

Where α is the incidence angle of parallel laser beams. For example, $\alpha = 15\ °$, $g = 853\ nm$; $\alpha = 17\ °$, $g = 770\ nm$; $\alpha = 25.17\ °$, $g = 520\ nm$.

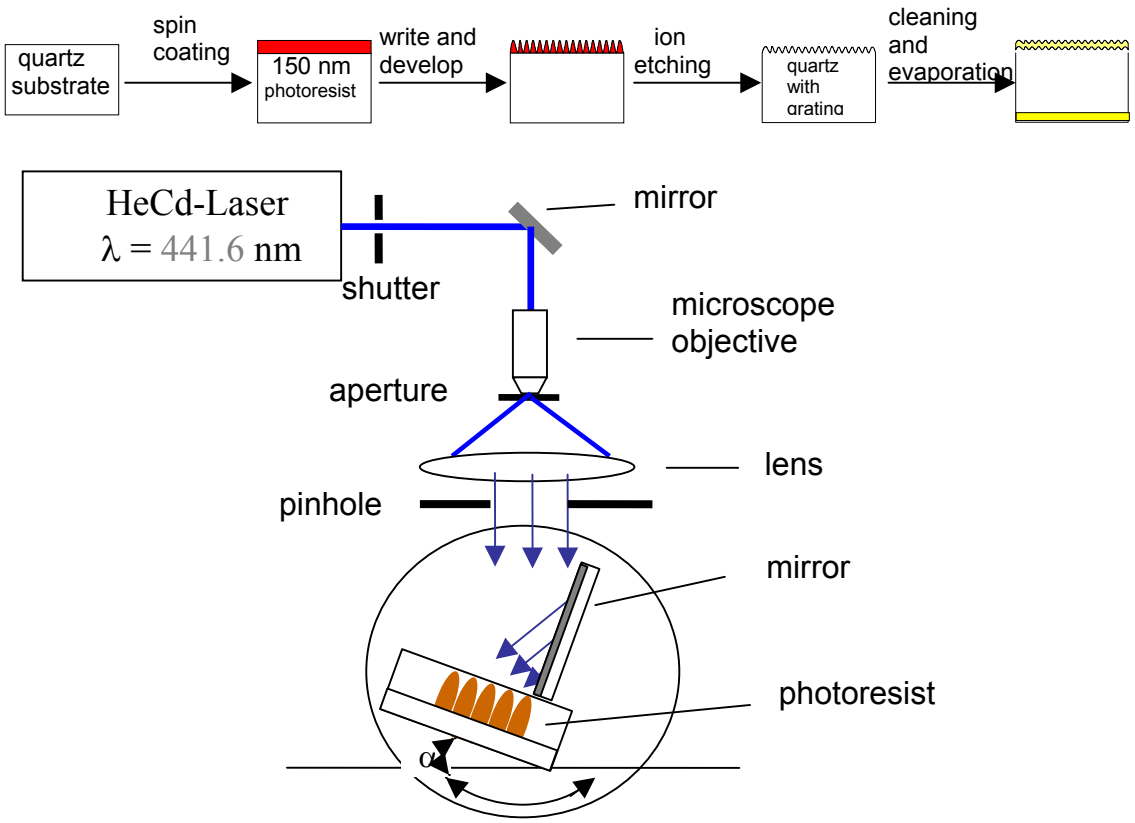

Figure 3.1: Preparation of surface corrugational gratings onto quartz surface and exposure of photo resist to produce an interference pattern for gratings.

The exposure time of photo resist film should be as long as possible, so that the film grating as a mask is thoroughly exposed to the bottom of the photo resist film and still remains close to the quartz surface; certainly the exposure time should not be unlimitedly long, otherwise the film may be completely or partly washed away during development. If the exposure time is short, the grating looks not good: sometimes it looks less colorful, sometimes there seems to be some kind of stripes like finger prints or parallel straight lines, and it shall

pose a serious problem in ion etching process, because the developed pattern does not completely reach the quartz surface and some unexposed photo-resist particles remain in the way for proper ion etching.

After exposure it should be developed in a kind of chemical solution (tetra methyl ammonium hydroxide, trade name: Microposit MF® CD-26, Shipley Europe Ltd. U.K., or Entwickler für Photoresist Ma-D 330, micro resist technology GmbH, Berlin) for 30 sec, then it should be washed in Milli-Q water for 10 sec, after that it should be blow dried with nitrogen gas, and then it should be hard baked at 110°C for 30 minutes.

3.1.5 Ion etching of the quartz surface with photo resist mask

The ion etching setup (Fig. 3.2) used in the preparation of gratings is home made equipment in Max-Planck Institute of Polymer Research, with main elements MICROMIX 4000 from ION TECH INC. and vacuum system from ROTH & RAU OBERFLÄCHEN TECHNIK GmbH. Usually two ion etching methods are used for these gratings into the quartz surface: physical and chemical methods.

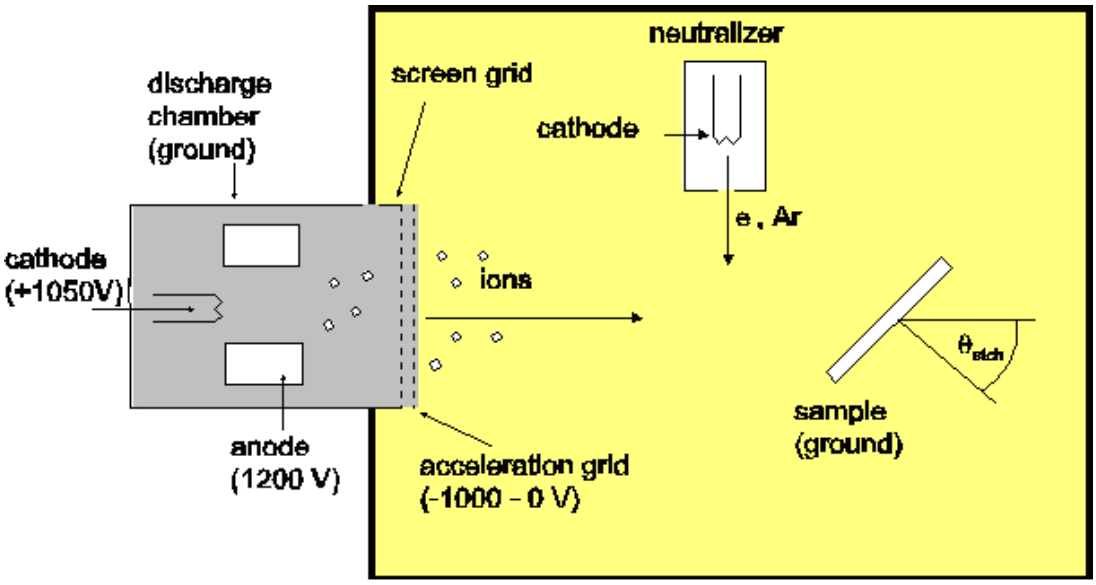

Fig: 3.2 Schematic of ion etching quartz surface. Here it is $\theta_{etch}=0°$ for perpendicular gratings. (Adapted from webpage http://www.mpip-mainz.mpg.de)

For physical ion etching (only argon is used), the following parameters were used: argon gas flow rate $\nu = 3.1\ ml/min$, cathode filament current $I = 9.75\ A$, accelerator voltage $U = 500\ V$, beam voltage $U_b = 200\ V$, PBN current $I_{PBN} = 47\ m\ A$. Ion etching time is $3 \times 20\ sec$. Ion etching time should not exceed 30 seconds, otherwise the photo resist film may be burnt and the grating pattern may be ruined. After each etching run the ion beam should be shielded

with a shutter for at least 30 seconds before another ion etching period begins. Under this condition the ion etching rate is 7 – 9 nm/min for chromium, 30 – 40 nm/min for gold, 30 – 40 nm/min for quartz.

Chemical ion etching (argon, oxygen and carbon tetra fluoride are used): gas flow rate for (1) argon, ν =1.6 ml/min, (2) O_2, ν = 0.8 ml/min, (3) CF_4, ν =1.2 ml/min, cathode filament current $I = 9.41\ A$, accelerator voltage $U = 600\ V$, beam voltage $U_b = 200\ V$, PBN current $I_{PBN} = 51\ m\ A$. Ion etching time is 3 × 15 sec. Ion etching time should be limited to 20 seconds in order to avoid chemical burning. Under this condition the ion etching rate is 20 – 30 nm/min for quartz material.

During the operation of the ion etching machine, the nitrogen valve should always stay in open state, and the ventilation handle should be loosely closed for security reasons, so that the machine can be automatically ventilated in case of power shut down incident. Before the vacuum pump works in a stable high speed running state (830Hz), don't leave the machine in case of accidents (mainly air leakage or nitrogen ventilation). Before ion etching the chamber pressure should be below 5×10^{-6} bar. The quartz surface should be perpendicular to ion beam inside the chamber in order to achieve vertical steps between the exposed and the unexposed portions of the quartz plate. The grating depth is very important for generating a good surface plasmon resonance, and 25 – 40 nm depth of grating is desirable for measurements in liquid.

3.1.6 Electrode evaporation

After ion etching, the wafers should be thoroughly cleaned: ultrasonic bath in acetone for 10 min to remove the remaining photoresist film, 15 min pure oxygen plasma cleaning to remove the surface organic contaminants, 10 min ultrasonic bath in a freshly prepared aqueous solution of 2% ammonium cerium (IV) nitrate to remove the excess chromium layer. After cleaning and drying, a new layer of chromium (2nm) and gold electrodes (front side 150nm, back side 300nm) should be evaporated onto the quartz surfaces. In order to improve the QCM resonance quality for measurements in liquids it is helpful to evaporate an additional small particle gold onto the center of the back electrode, in our case 50 nm gold (a very small spot ca. 1mm in diameter) was evaporated onto the center of the back side quartz wafer. By doing so, we find the resonance peak is far separated from its side bands of various overtones measured in liquid and we can get a stable base line. The front side of the quartz

wafer is the working area and is usually grounded; while for electrochemical measurements the potential shall be controlled by a potentiostat.

Fig.3.3 shows QCM with gratings used in our measurements. These 1 inch diameter wafers are the key components needed for in-situ combination measurement of QCM and SPR. In Fig.3.3 (a) the 150nm thick front electrode of 14 mm in diameter is shown, on which the half moon shaped pattern indicates the surface corrugation gratings. In Fig.3.3 (b) the 300 nm thick back electrodes are shown. The small round back electrode in the center is ca.300 nm thick and ca.5 mm in diameter for better energy trapping. The front electrode is connected to the back side by using a kind of silver paste (Demetron GmbH) on the edge of the quartz. So both electrodes are connected to impedance analyzer from the back side of the quartz. The little point in the center shows the additional evaporated gold particle of 50 nm thick and ca.1 mm in diameter for higher measurement quality in liquid. In Fig.3.3 (c) is the actual picture of a piece of QCM with shining gratings. In Fig.3.3 (d) 2 kinds of Maxtek plastic holders are shown: the white one is made of Teflon, while the grey one is made of PVC.

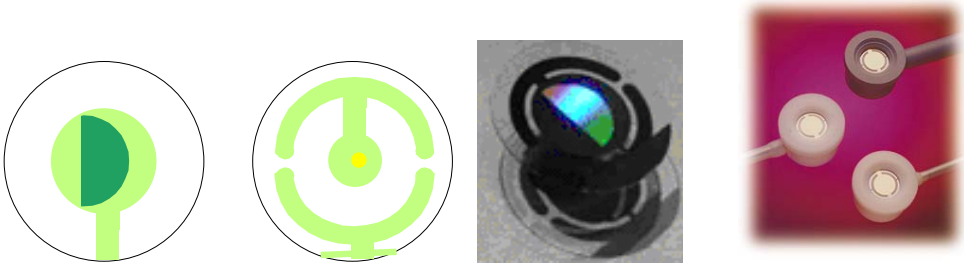

(a) front side (b) back side (c) photograph (d) holder

Figure 3.3: Quartz crystal Microbalance with gratings. (a) Front side electrode (working area, usually grounded); (b) back side electrode; (c) photographic picture of QCM with gratings; (d) QCM Maxtek holder with quartz.

Small quartz of 14 mm diameter with a 5 nm thick chromium layer and a 150nm thick photo resist film mask was exposed to He-Cd laser interference beam at an angle of 17°, and later ion etched for 3 × 30 sec in physical method and 3 × 20 sec in chemical method according to the above stated methods. After gold electrode evaporation surface plasmon resonance angle scan was measured in air, and the result is shown in Fig. 3.4. From this graph, we can read the plasmon angle in air is around 12°, and the width of the peak is about 5°, very sharp.

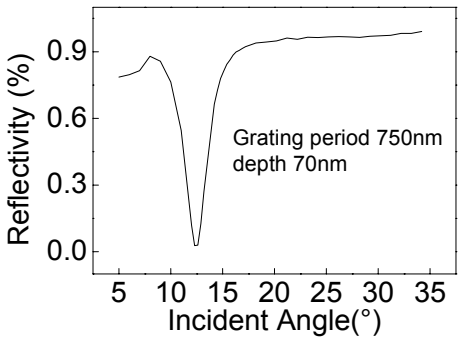

Figure 3.4: Example of SPR angle scan in air.

This SPR angle scan shows that the gratings are too deep for a good SPR minimum angle tracking measurement, because the reflectivity at the plasmon angle is too low. Usually we expect that the reflectivity at the plasmon angle is around 0.5 for a good SPR angle tracking measurement. Kirstin Petersen made the corresponding AFM measurement, and the result is shown in Fig. 3.5. The measured grating depth was about 67 nm and the grating constant was 750 nm. The AFM picture shows that there are some contaminations in the gratings and the gratings are not perfectly regular.

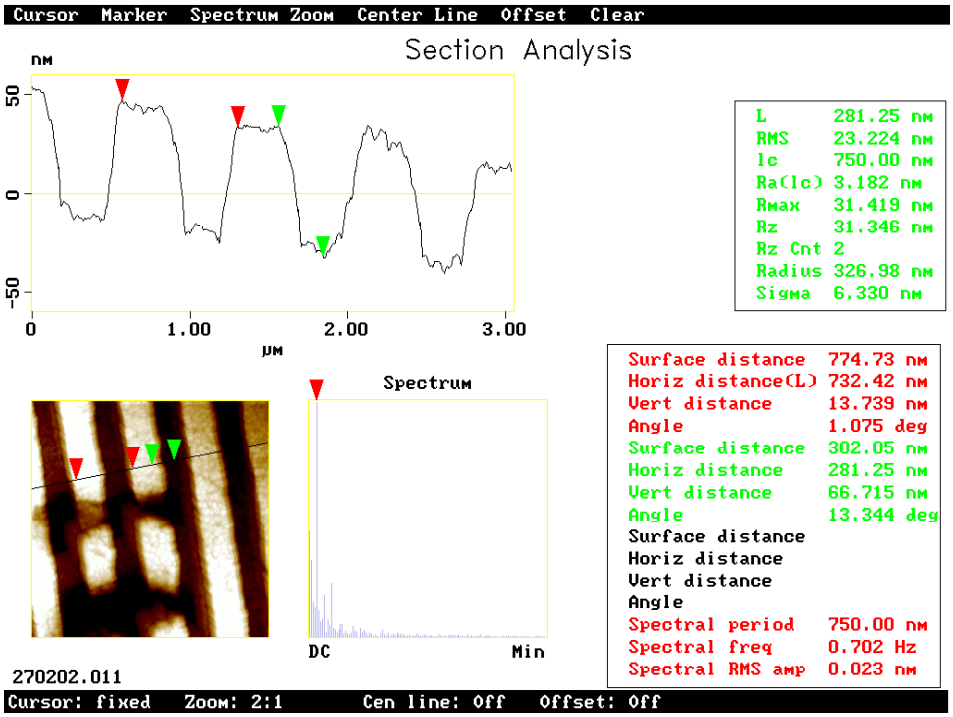

Figure 3.5: AFM image of gratings on the surface of quartz crystal microbalance.

3.2 Experimental setup of combined SPR and QCM

This setup consists of two independent systems: SPR system and QCM system, in terms of both hardware and software. The SPR system and the QCM system can work also independently. Both SPR and QCM computer programs are written by Prof. Johannsmann. Fig. 3.6 shows the combined SPR and QCM setup and the corresponding mechanism.

3.2.1 Surface plasmon setup

As shown in Fig. 3.6 (a) , the SPR system includes laser source (class IIIb, 10 mW), light chopper model 197(EG&G 15Hz – 3kHz), lock-in amplifier (EG&G model 5210), 2 × polarisator, 2 × pin hole, Lenz, photodiode detector, goniometer (Huber), motor controller and other small parts.

3.2.1.1 Angle Tracking

The best choice in monitoring film change as a function of time is angle tracking. There are two modes: basic mode and advanced mode. In the basic mode, the system always moves the goniometer around the minimum and records the angle value. The simple mode has a large noise. There is an advanced mode, which uses 3 or more data points and shifts the experimental plasmon curve in order to match the data alternatively; it fits a parabola through these three or more data points and considers the apex of the parabola the coupling angle. This mode assumes that the plasmon looks like a parabola close to the minimum. The advanced mode has a smaller noise but also is much slower than the simple mode.

3.2.1.2 Reflectivity Tracking

A measurement of the coupling angle involves the movement of the goniometer and therefore is inherently slow. An alternative is "reflectivity tracking". Here, one monitors the intensity at the detector at one single angle on the slope of the plasmon.

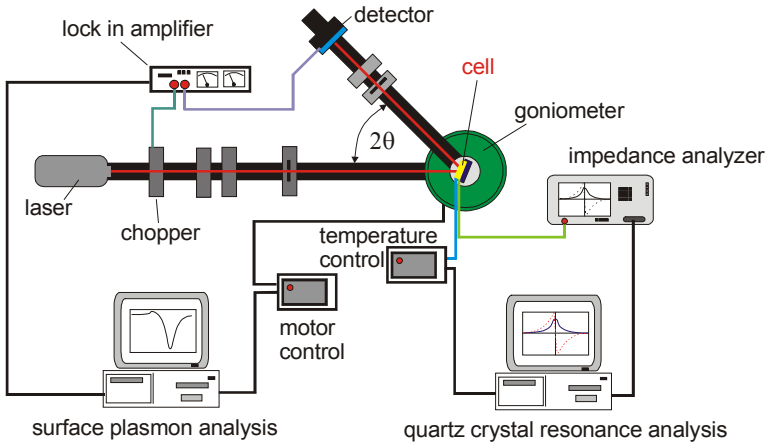

(a)

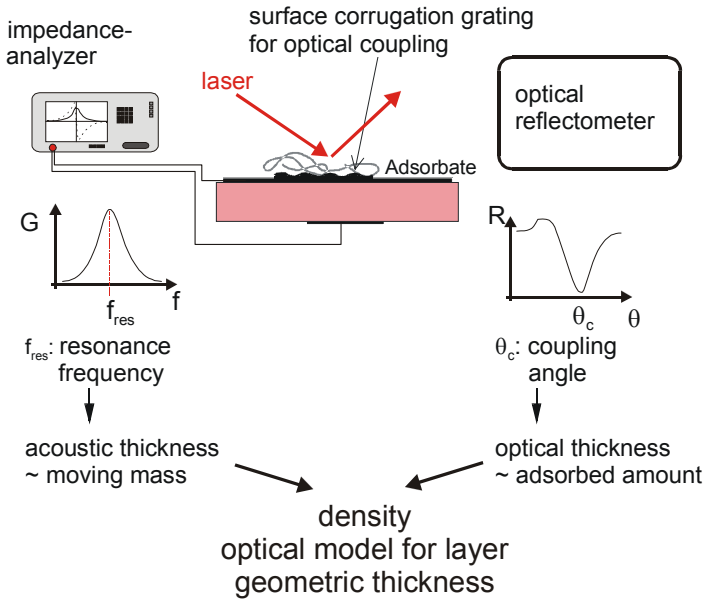

(b)

(c) liquid cell

(d) temperature control unit

Figure 3.6: Schematic of experimental setup of combined QCM and SPR. (a) experimental setup; (b) Principle schematic of combined QCM and SPR measurement; (c) liquid cell and (d) temperature control unit.

3.2.2 Network analyzer for QCM measurement

We use network analyzer (Hewlett Packard E5100A, 10 kHz - 300MHz, Agilent technologies) in QCM measurement. (See Fig. 3.7)

Figure 3.7: Network analyzer (Hewlett Packard E5100A, from Agilent technologies) for QCM measurement. (adapted from webpage http://cp.literature.agilent.com/litweb/pdf/5965-4972E.pdf)

3.2.2.1 Normal mode

With full frequency sweeps, the time for data acquisition per data point is typically 1 second or more. With this instrument, there are a few parameters can be adjusted: number of points, driving power, and system bandwidth. The number of points can be set at 801, 401, 201, 101, 51, 21, 11, 5, 3; the larger the number of points is, the slower is data acquisition, but with a higher accuracy; usually it is set at 201. Driving power can be set between -7.5 dBm and 7.5 dBm; it is recommended that for measurements in liquid, the driving power be set at 7 dBm for accuracy. System bandwidth can be set at 10 Hz, 30 Hz, 100 Hz, 300 Hz, 1 kHz, 3 kHz, 10 kHz, and 30 kHz; the larger the IF Bandwidth is, the quick is data acquisition; usually it is set at 3 kHz.

3.2.2.2 Fast Mode

In the "Fast Mode" the impedance analyzer goes to fixed frequency on the center of the resonance and keeps measuring conductance, G, and susceptance, B, on just this one frequency. It can do so with a data acquisition rate of about 50 Hz (HP E5100). From the shifts of G and B the software estimates the shifts in f and Γ. Certainly there is a sacrifice in accuracy of measurements.

3.2.3 Temperature control

The temperature controller (-100°C -- +200°C) was made by electronics workshop in Max-Planck-Institute of Polymer Research, see Fig. 3.6 (c) and (d). We use a temperature control program, which can perform different ramps and steps in temperature scan.

3.2.4 Experimental explanation

The surface plasmon coupling angle depends slightly on the depth of the grating. With regard to *shifts* of the coupling angle upon adsorption this effect cancels. Importantly, the

grating used for coupling is very shallow (typical aspect ratio < 1/10). Due to the low aspect ratio, the effect of trapped liquid in the corrugated structures can be neglected. A gold layer (~150 nm with a 2 nm chromium adhesion promoter) was evaporated over the grating (maintaining the corrugation), which simultaneously acts as the QCM electrode and the SPR coupling layer. The back electrode was keyhole-shaped and much thicker (300 nm) than the front electrode in order to achieve energy trapping. The resonance properties were measured passively with an impedance analyzer (HP E5100 from Agilent technologies). Resonance frequency and bandwidth were determined by fitting resonance curves to the conductance spectra (Lorentz fitting). The quartz plate usually operates in liquid at the 1^{st}, 3^{rd}, 5^{th}, 7^{th}, and 9^{th} harmonic (i.e. at 5, 15, 25, and 35, 45 MHz), respectively.

The quartz plate was placed in a holder from Maxtek Inc. (Torrance, CA). (See Fig.3.3(d)) The liquid cell had a volume of about 1 ml. The quartz surface is accessible to the laser beam through the front glass window. Special care must be taken with regard to the cell design in order to deal with compression waves. [LW95] AT-cut quartz plates with key-hole shaped back electrodes emit compression waves in addition to the dominant shear contribution. Longitudinal sound can be detrimental because it propagates in liquids and can be reflected from the opposing cell surface. The measurement suffers from a cell design where the opposing surface is planar and parallel to the quartz plate, because the cell in this case can form an acoustic cavity. When ramping the temperature, the effective size of the cavity is tuned via the speed of sound and one observes a set of secondary resonances ("cuvette resonances") occurring whenever the cell thickness equals an integer multiple of the wavelength. It is therefore essential that the cell is irregularly shaped. The cell used in this study had the front window *inclined* with respect to the quartz plate. Although such an inclination certainly complicates the optical analysis, it proves necessary to avoid the cuvette resonances.

3.3 Effect of laser beam on QCM resonance

Quartz crystal microbalance is a very sensitive instrumental measurement method. A lot of environmental factors can change the resonance frequency of quartz crystals, like clamping force, deformation of the quartz, changes in the electric contact points, contact media, temperature, air pressure, etc. So each time the quartz crystal is installed inside the same quartz holder, there are some changes in its resonance frequency and bandwidth. Even some tiny dust particles on the quartz surface may change its resonance a lot. For combined measurement of QCM and SPR, the laser beam falling on the quartz surface can change its resonance: increase the resonance frequency while decrease the bandwidth.

For 5 MHz QCM without gratings, laser beam can cause some noise in QCM resonance at the moment of starting the laser on and/or off. But for QCM with gratings, the resonance frequency f can be a little higher with laser beam falling on the grating area in air: several Hz to 100 Hz; while the half band half width Γ becomes a little smaller. For QCM crystal with deep gratings the laser beam has an obvious effect on QCM resonance in air. It suggests that one can measure the SPR coupling angle using QCM resonance frequency shift instead of the signal from SPR diode detector. Certainly there are some technical difficulties in data collection using one computer.

Fig. 3.8(a) shows that at an incident angle of 4.5°, the laser beam has a little effect on QCM resonance: the laser beam makes the resonance frequency 3 Hz larger, while the HBH width Γ stays almost at the same level (in the graph it shows a noise signal). At SPR plasmon angle 8.6°, the laser effect is the largest, and the frequency shift at third harmonic is about 14 Hz. As the laser effect on fundamental harmonic is not as large in air as on higher harmonics, the graph for 5 MHz is not shown. Sometimes we can also get a good curve in bandwidth shift with laser (see Fig. 3.8(b)). Our measurements show that for all harmonic overtones of QCM with gratings, the resonance frequency gets a little larger, while the bandwidth gets a little smaller; and the higher the overtone is, the larger is the resonance frequency shift with laser exposure.

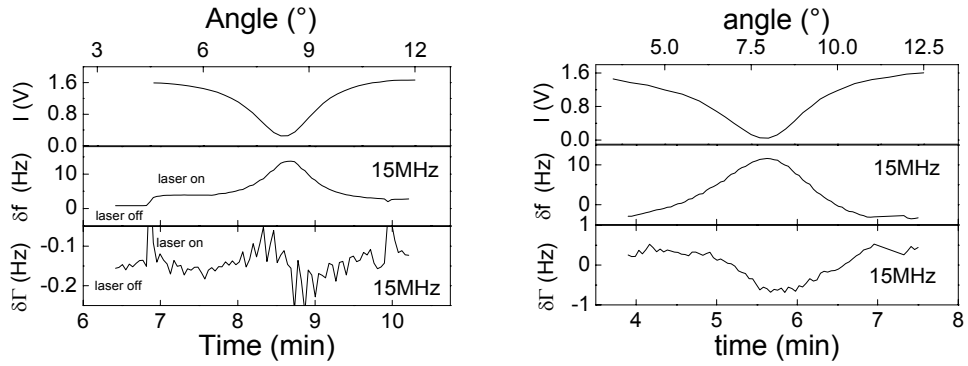

(a) **(b)**

Figure 3.8: Effect of laser beam and SPR angle scan on QCM resonance in air (quartz with deep gratings, grating constant 520nm)

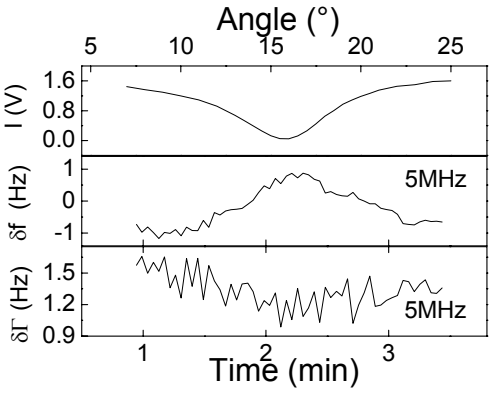

Figure 3.9: Effect of laser and SPR angle scan on QCM resonance in water (quartz with deep gratings, grating constant 520nm)

The effect of laser beam on QCM resonance in liquid is not as obvious as that in air, only 1 Hz, within measurement error (See Fig. 3.9). At plasmon angle 16°, the frequency is only 2 Hz higher, and the bandwidth shift is not stable. The resonance frequency shift at higher harmonics induced by laser in water is not as obvious as that at fundamental overtone, so their measurement results are not shown here. This result suggests that laser induced temperature variations and the thermally induced stress relaxation may be part of the explanation. Since the liquid removes laser induced heat very efficiently, and/or the energy dissipation in liquids is much larger than in air, the laser effect on QCM measurements is much smaller in liquids than it is in air.

Generally speaking, for quartz crystals with gratings, the resonance frequency increases with laser exposure, while the half-band-half-width decreases. We don't understand the mechanism of laser effect on QCM. But we have also found some similar abnormalities in Maxtek quartz crystals: for the first 3 overtones, the resonance frequency increases with laser; while for higher overtones, the resonance frequency decreases with laser.(See Fig. 3.10) For this quartz crystal, it seems that resonance frequency shift depends on different cut-type of the quartz and may change with different overtones. We may think that this behavior is caused by complex stress relaxation coupled with temperature change in the electrode at the laser point.

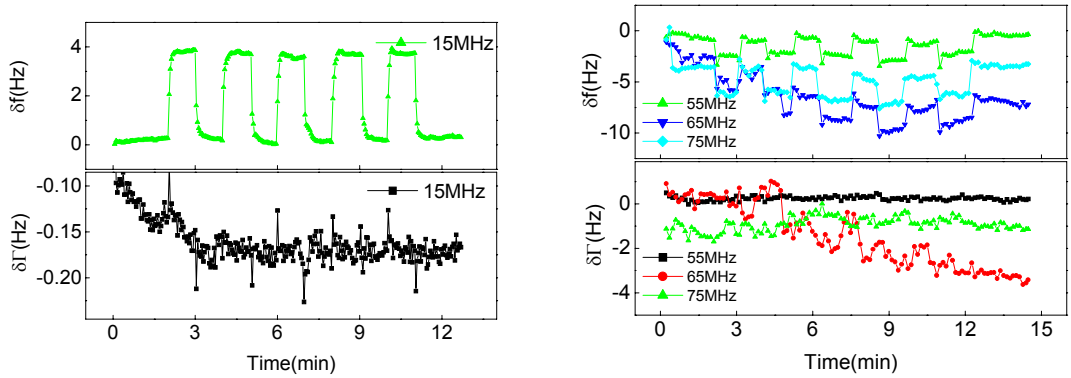

(a) **(b)**

Figure 3.10: Effect of laser exposure on QCM (without gratings) resonance. Both (a) and (b) are data from the same Maxtek Quartz crystal.

For the combined measurement with shallow gratings in liquid using QCM and SPR, the effect of laser beams on QCM resonance should be much smaller, within allowable instrumental errors. On the other hand, we didn't see any effect of QCM on plasmon resonance measurement. So we may think that during the combined measurement of QCM and SPR, both instruments work separately and reliably, and there is little influence on each other.

4 Measurement of elastic shear modulus of metal films (Au, Ag) using QCM

Elastic effects contribute to the shift in resonance frequency of quartz crystal resonators induced by deposition of thin films on the resonator surface. In turn, the mechanical stiffness of the film can be experimentally determined from a comparison of the resonance shifts on different harmonics. When the film is much thinner than the wavelength of shear sound, a series expansion of the elastic effects to third order in film thickness leads to rather simple equations. When we plot the fractional frequency shift $\delta f / f$ versus the square of the overtone order n^2 , we find a linear relationship, where the slope is determined by the film's elastic compliance.

4.1 Introduction[4]

Quartz crystal resonators have been used extensively to monitor the physical properties of thin layers on their surfaces.[LC84] In commercial applications, film thickness determination is usually of main interest. For a thin film the frequency shift is a function of the mass alone; its acoustic properties may be ignored. In this approximation the well known Sauerbrey equation holds, stating that the frequency shift is proportional to the deposited mass.[Sau64]

The determination of shear compliance of a film from shifts of the resonance frequency has recently been addressed by a number of workers. [Joh99] [MF91] [JMW+92] [FSR+98] [BHB+97] [LH97] The elastic parameters are derived from a comparison of the frequency shifts on different overtones. ‘‘Overtone quartzes’’ with polished, planar surfaces are employed for these measurements. Generally speaking, elastic effects are negligible whenever the film thickness is much less than the acoustic wavelength. In this case the film is essentially located in an antinode of the standing shear wave. Since the film does not experience shear, the frequency shift is independent of the film's elastic properties. If, on the other hand, the film thickness is comparable to one quarter of the wavelength of sound, the elastic effects are rather dramatic. The film itself then forms a resonator. The ‘‘film resonance’’ couples to the quartz crystal resonance and a rather complicated picture emerges. [MF91] [JMW+92] [MBC+00][MF91]The frequency shift is described by transcendental equations which can only be solved numerically. There is a rather interesting regime between

[4] Partly adapted from: D. Johannsmann, Derivation of the shear compliance of thin films on quartz resonators from comparison of the frequency shifts on different harmonics: a perturbation analysis J. Appl. Phys. 87 **(2001)** 4182

the Sauerbrey limit and the film resonance, where the elastic effects are small but still significant. In this regime a perturbation analysis may be carried out and a rather simple scheme for determining the shear compliance emerges.

In terms of algebraic complexity, the easiest case is given by two identical films on both sides of the quartz plate. We provide the derivation for this case in full detail (Section III). Asymmetric situations with a film on just one side of the quartz are of more practical interest. The extension to this case is straightforward, although the equations become clumsier. Geometry with two films situated one above the other is interesting for two reasons: First, the analysis can serve to elucidate the role of the electrodes whose finite elasticity affects the results in some cases. Second, if a film is sandwiched between the quartz and the second layer, this film's stiffness can be derived even if the film is very thin because the film has been moved away from antinode of the standing wave by addition of the cover layer.

4.1.1 Equivalent circuits

The analysis starts out from the Mason equivalent circuit depicted in Fig. 4.1.

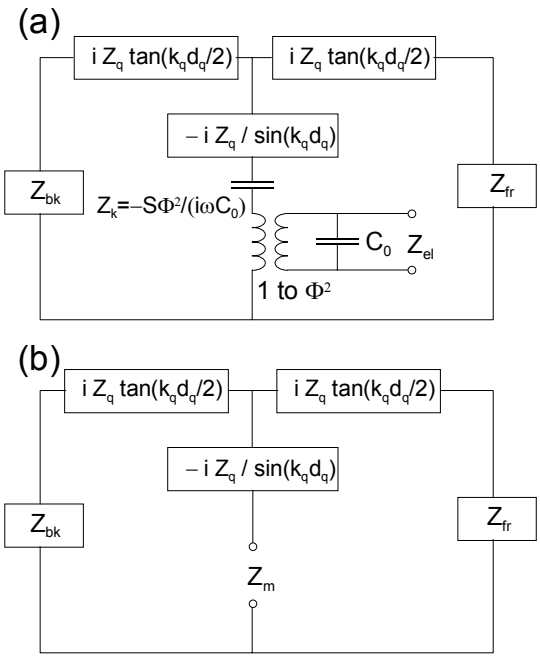

Figure 4.1: The Mason equivalent circuit. Part (b) shows the circuit without the electrical capacitance and the element Z_k accounting for piezoelectric stiffening. The resonance condition used in the calculations is $Z_m=0$.

The transformer represents piezoelectric coupling. The ratio Φ is given by $\Phi = Se_{26}'/d_q$ with S the active surface area, $e_{26}' = 9.65 \times 10^{-2}\ C\ m^{-2}$ the relevant piezoelectric coefficient, and d_q the thickness of the resonator. Note that acoustic impedances are normalized to unit area, whereas electric impedances are not. The acoustic impedance Z_q of AT-cut quartz is $Z_q = 8.8 \times 10^6\ kgm^{-2}s^{-1}$, $k_q = \omega/v_q$ is the wave number of transverse sound, with $v_q = 3350\ m/s$ the speed of sound. d_q is the resonator thickness. $C_0 = \varepsilon\varepsilon_0 S/d_q$ is the electric capacitance with $\varepsilon = 4.54$ the relative dielectric permittivity. The loads on either side are represented as single elements Z_{fr} and Z_{bk}.

Note that the Mason circuit assumes a one-dimensional model, that is, laterally infinite piezoelectric plates. Stevens and Tierstein have provided a three-dimensional (3D) analytical calculation for the resonance frequencies of plane–convex quartz plates without films. [ST86] We are not aware of a 3D analytical treatment of quartz plates covered with a film. Presumably, one will have to resort to a numerical finite element analysis. [WYI99]

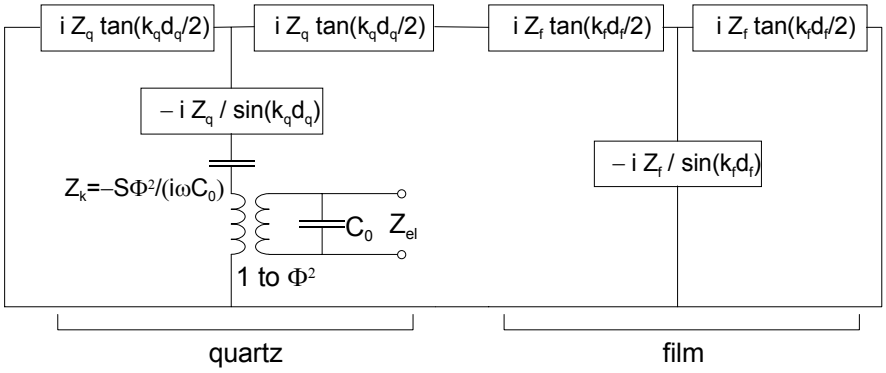

Figure 4.2: An explicit representation of a resonator loaded with a single film. Multilayer can be modeled by multiple sets of circuit elements such as shown on the right-hand side.

If one is interested in sensor applications rather than frequency control, a load has to be included in the model. The load could be a film, a liquid, a tip touching the surface, or any other object interacting with the oscillating quartz. Here we are concerned with stratified layers and layer systems coated onto the quartz surfaces. The loads are represented by generalized impedances, $Z_{fr}(\omega)$ and $Z_{bk}(\omega)$, on the front and the back side of the plate. Note that these elements are not to be understood as simple-valued quantities in the ‘‘lumped-element’’ sense.[CMH+98] Their frequency dependence may be arbitrarily complex. Z_{fr} and Z_{bk} are defined as the ratio of stress, σ, and lateral velocity, du/dt (u the displacement), at the quartz surface. This ratio can be calculated either from application of the Kirchhoff rules to

equivalent circuits like the one shown in Fig. 4.2 [Ros88] or from a multilayer matrix formalism based on reflectivity as it is known from optics. [JMW+92][AB87]

With given loads, $Z_{fr}(\omega)$ and $Z_{bk}(\omega)$, the circuit is fully specified and the electrical impedance, Z_{el}, across the electrical port can be straightforwardly calculated. Note, however, that the impedance itself is of minor interest in the context of sensor applications. Rather, one determines the resonance frequencies where the amplitude of motion and the current through the electrodes become large. The resonance condition is given by $Z_{el}(\omega) = 0$. While frequencies can be easily measured with a relative accuracy down to $\delta f/f \sim 10^{-7}$, the impedance can routinely only be determined with an accuracy of about 1%. Viscous losses are accounted for in the calculation via complex wave numbers, k. The complex frequency which solves the equation $Z_{el}(\omega) = 0$ is to be understood in the sense that the imaginary part is the half-band half-width of the resonance. Without further assumptions, the resonance frequencies of the Mason circuit can be found with a numerical search of the zeros of $Z_{el}(\omega)$. This procedure can be integrated into automated routines for the analysis of experimental data. The fitting routines would involve the search of these zeros, which shift on the frequency scale as the parameters of the circuit shift as an intermediate step. At this level the neglect of 3D effects is the only simplification. When checking the validity of the various approximations introduced below, comparison with this numerical solution of $Z_{el}(\omega) = 0$, therefore, is a perfectly adequate method.

Figure 4.3 shows the outcome of three such numerical searches for $Z_{el}(\omega) = 0$. The fractional frequency shift, $\delta f / f$, induced by 100 nm films with three different mechanical stiffness, is plotted versus the square of the overtone order, n². (For the generalized impedance, $Z_{fr}(\omega)$, of a single film see Eqn.(4.6) below.) For high harmonics, the dependence of $\delta f / f$ on n² approaches a linear relationship. The slope of this line, S_n, contains the elastic compliance J_f'. At low harmonics one finds a systematic positive deviation from the linear relationship. It is caused by piezoelectric stiffening as given by the term Z_k in Fig. 4.1. Since Z_k scales as ω^{-1}, its effect is most prominent on low harmonics. Piezoelectric stiffening is not accounted for in the analysis given below, that is, the term Z_k has been neglected. In practice, we have so far just excluded harmonics lower than $n=7$ from the analysis of experimental data. A correction scheme seems possible as well.

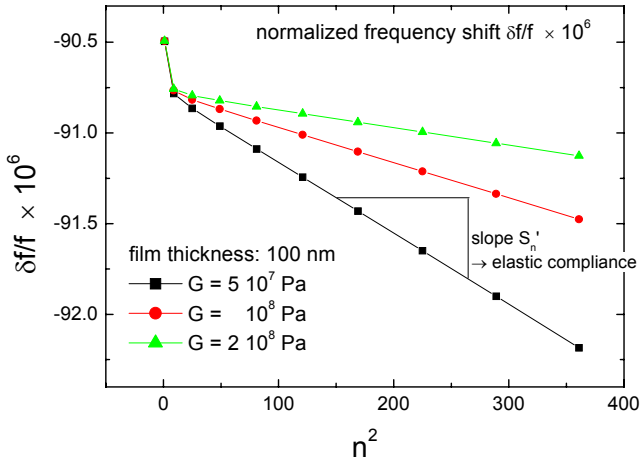

Figure 4.3: Calculations of fractional frequency shifts $\delta f/f$ versus n^2 (n the overtone order) obtained by numerically searching the zeros of the imaginary part of the electrical impedance Z_{el} (see Fig. 4.1 (a)). The quartz blank is assumed to be covered with a 100 nm film of density $\rho = 5 \times 10^3$ kg/m^3. The shear modulus G is indicated in the figure. For high harmonics, the data approach a straight line, whose slope S_n, contains the information on elasticity. The upward curvature on low harmonics is caused by the piezoelectric stiffening Z_k (see Fig. 4.1). Neglecting Z_k, one can calculate the slope S_n by a perturbation analysis.

At high harmonics, one also finds a slight deviation from the linear relationship. The linear relationship is the consequence of a series expansion of the load to third order in film thickness (see below). As the ratio between the film thickness and the wavelength of sound increases, this expansion becomes invalid. Also not contained in the calculation displayed in Fig. 4.3 is a possible dependence of the shear modulus G on frequency ω (''elastic dispersion''). Especially for polymers, the shear modulus is a function of frequency.

In the MHz range, G smoothly increases with frequency with a power law exponent between 0 and 1/2. While one might be tempted to experimentally derive the dispersion $G(\omega)$ from the nonlinearity in plots of $\delta f/f$ versus n^2, this is dangerous because of the other sources of nonlinearity. However, elastic dispersion can be straightforwardly included into the Mason circuit via the corresponding nontrivial frequency dependence of the wave number k. The Mason circuit accounts for all other sources of nonlinearity as well. A numerical search of the zeros of $Z_{el}(\omega)$ of the Mason circuit should therefore be employed whenever nonlinearities in the plot of $\delta f/f$ versus n^2 are expected or observed.

4.1.2 Two identical films on both surfaces

We now turn to the calculation of the impedance across the electrical port Z_{el} . In the following we neglect the electrical capacitance C_0 since it does not affect the position of the series resonance frequency (which we term ‘‘resonance frequency’’). Also, we neglect the impedance Z_k accounting for piezoelectric stiffening as discussed above. This amounts to considering mechanical impedance Z_m rather than Z_{el} as indicated in Fig. 4.1(b). We first discuss the symmetric situation with $Z_{bk}=Z_{fr}$. From Fig. 4.1(b) one reads the condition

$$0 \approx Z_m = -\frac{iZ_q}{\sin(k_q d_q)} + \left[\left(iZ_q \tan(\frac{k_q d_q}{2}) + Z_{fr} \right)^{-1} + \left(iZ_q \tan(\frac{k_q d_q}{2}) + Z_{bk} \right)^{-1} \right]^{-1}$$
$$= -iZ_q \frac{1+\tan^2(\frac{k_q d_q}{2})}{2\tan(\frac{k_q d_q}{2})} + \frac{1}{2}\left(iZ_q \tan(\frac{k_q d_q}{2}) + Z_{fr} \right) = -\frac{iZ_q}{2}\cot(\frac{k_q d_q}{2}) + \frac{Z_{fr}}{2} \qquad (4.1)$$

where we have used the relation $1/\sin(2x)=(1+\tan^2(x))/(2\tan(x))$ in the second line. d_q is the thickness of the quartz plate and k_q is the wave number. $Z_q=8.8\times10^6\ kgm^{-2}s^{-1}$ is the acoustic impedance of AT-cut quartz. Note that Z_q is not generalized impedance like Z_{fr} and Z_{bk} but a material constant. Because the load impedance Z_{fr} is much smaller than the impedance of the quartz Z_q, resonances occur close to the poles of the tangent. We write the argument of the tangent as

$$\frac{k_q d_q}{2} = \frac{n\pi}{2}(1+\varepsilon), \quad n=1, 3, 5, \ \ldots . \qquad (4.2)$$

With ε a small complex number and n the overtone order. The resonances correspond to standing waves with antinodes at the quartz surface. For the fundamental, the wavelength is just twice the quartz thickness. Only odd harmonics are electrically excited because the total shear induced polarization vanishes for symmetric strain patterns.

For the resonance frequency ω_r one has

$$\omega_r = \omega_{n,u}(1+\varepsilon) = nk_{q,1}v_q(1+\varepsilon) = \frac{n\pi}{d_q}\sqrt{\frac{G_q}{\rho_q}}(1+\varepsilon), \qquad (4.3)$$

with $\omega_{n,\mu}$ the nth resonance frequency of the unloaded quartz, $k_{q,l}=2\pi/\lambda_{q,l}=\pi/d_q$ the wave number of shear sound on the fundamental, G the shear modulus, ρ the density, m the mass per unit area, $\upsilon=(G/\rho)^{1/2}$ the speed of sound, and $Z=\rho\upsilon=(G\rho)^{1/2}$ the acoustic impedance. The index q denotes the quartz. ε is equal to the fractional complex frequency shift $\delta f^*/f=\delta f/f + i\,\delta\Gamma/f$, where Γ is the half-band half-width of the resonance.

Inserting $cot(n\pi(1+\varepsilon)/2)=-tan(n\pi\varepsilon/2)$ into Eqn.(4.1) one derives the resonance condition

$$0 = iZ_q \tan(\frac{n\pi\varepsilon}{2}) + Z_{fr} \qquad (4.4)$$

The generalized impedance Z_{fr} is the ratio between the shear stress σ and the velocity du/dt at the quartz surface. One has

$$Z_{fr} = \frac{\sigma}{du/dt} = \frac{G_f(du/dz)}{du/dt} = \frac{G_f ik_f(u_+ - u_-)}{i\omega(u_+ + u_-)} = \sqrt{\rho_f G_f}\frac{1-r}{1+r} = Z_f\frac{1-r}{1+r} \qquad (4.5)$$

where z is the vertical coordinate, u_+ and u_- are the amplitudes of the waves traveling in the upward and the downward direction, $r=u_-/u_+$ is the reflection coefficient evaluated just above the quartz surface, and the index f denotes the medium in contact with the quartz surface. As Eqn. (4.5) shows, the calculation of the generalized impedance amounts to a calculation of reflection amplitude, which can be done analogously to the matrix formalism in optics.[AB87] Alternatively, one could apply the Kirchhoff rules to equivalent circuits such as shown in Fig.4.2.

We now assume that the load Z_{fr} is given by a film with a thickness d_f and acoustic impedance Z_f. Here and in the following the index f denotes a film. With a perfectly reflecting film–air interface and a phase factor of $exp(ik_fd_f)$ between the film surface and the quartz–film interface one arrives at [JMW$^+$92]

$$Z_{fr} = Z_f\frac{1-\exp(2ik_fd_f)}{1+\exp(2ik_fd_f)} = iZ_f\tan(k_fd_f) = iZ_f\tan(n\pi(1+\varepsilon)\frac{Z_q}{m_q}\frac{m_f}{Z_f}) \qquad (4.6)$$

where Eqn. (4.3) has been used for $k_f=\omega/\upsilon_f$ and the thickness d_f was converted to mass per unit area, m_f, by the relation $d_f=m_f/\rho_f=m_f\nu_f/Z_f$. The poles of the tangent correspond to the film resonance. [MF91] [JMW$^+$92] Note that the approximation $Z_{fr}<< Z_q$ breaks down close to the film resonance. As a consequence the resonant frequencies do not go to infinity. Rather, one has two separate branches at frequencies above and below the resonance frequency of the bare quartz. Inserting Eqn.(4.6) into Eqn. (4.4) one arrives at the relation:

$$0 = Z_q\tan(\frac{n\pi\varepsilon}{2}) + Z_f\tan(n\pi(1+\varepsilon)\frac{Z_q}{m_q}\frac{m_f}{Z_f}) \qquad (4.7)$$

or equivalently

$$0 = \tan(\frac{n\pi\varepsilon}{2}) + \frac{1}{\xi}\tan(n\pi\mu\xi(1+\varepsilon)) \qquad (4.8)$$

where we have introduced the dimensionless parameters $\mu=m_f/m_q$ and $\xi=Z_q/Z_f$. The parameter ξ contains the elastic information. The parameter μ is a dimensionless mass per unit area. Eqn. (4.8) was first derived by Lu and Lewis [LL72] and is often used to correct for elastic effects in commercial thickness monitors. The parameter ξ is the same as the ‘‘*Z*-

ratio'' frequently used in this context. Eqn. (4.8) is an implicit equation in the fractional frequency shift $\delta f/f = \varepsilon$. For $\mu = 0$ it is trivially solved by $\varepsilon_0 = 0$. Since μ is a small number it can serve as a perturbation parameter. One can write $\varepsilon = \varepsilon_1 + \varepsilon_2 + \varepsilon_3 + \ldots$ and iteratively solve for the different perturbation orders. Series expansion of the tangents in Eqn. (4.8) to first order ($\tan x \approx x$) results in

$$0 = \frac{n\pi\varepsilon}{2} + n\pi\mu(1+\varepsilon) \tag{4.9}$$

Solving for $\varepsilon = \delta f/f$ one finds

$$\varepsilon \approx -\frac{2\mu}{1+2\mu} \approx -2\mu \tag{4.10}$$

Elasticity has dropped out and the Sauerbrey equation was recovered. The factor of 2 arises because we consider films on both surfaces. In order to capture the elastic effects one has to expand the tangent to third order. Using

$$\tan x \approx x + \frac{x^3}{3} \tag{4.11}$$

the resonance condition reads

$$0 \approx \frac{n\pi\varepsilon}{2} + \frac{1}{3}\left(\frac{n\pi\varepsilon}{2}\right)^3 + n\pi\mu(1+\varepsilon) + \frac{1}{3}(n\pi\mu)^3\xi^2(1+\varepsilon)^3 \tag{4.12}$$

Expanding Eqn. (4.12) to first order in ε one finds

$$0 \approx n\pi\mu + \frac{1}{3}(n\pi\mu)^3\xi^2 + \varepsilon\left(\frac{n\pi}{2} + n\pi\mu + (n\pi\mu)^3\xi^2\right) \tag{4.13}$$

By solving Eqn. (4.13) for ε and expanding the solution to third order in n and μ find the first order perturbation result

$$\begin{aligned}\varepsilon_1 &= -\left(n\pi\mu + \frac{1}{3}(n\pi\mu)^3\xi^2\right)/\left(\frac{n\pi}{2} + n\pi\mu + (n\pi\mu)^3\xi^2\right) \\ &\approx -2\mu + 4\mu^2 - 8\mu^3 - \frac{2}{3}(n\pi)^2\mu^3\xi^2\end{aligned} \tag{4.14}$$

The Sauerbrey equation corresponds to the first term on the right-hand side. As anticipated, Eqn. (4.14) contains a viscoelastic term scaling as the square of the overtone order, n^2. However, Eqn. (4.14) is at variance with intuition: if a material is added to the quartz surface which has the exact same acoustic properties as the quartz plate $\xi = 1$ the elastic effects must vanish. In terms of acoustics, this layer only increases the thickness of the quartz plate and the fractional frequency shift on all harmonics equals the fractional increase in thickness. On the other hand, elastic effects would not disappear in this case if Eqn. (4.14) was the full result. This inconsistency is caused by the fact that we have so far only considered terms linear in ε,

while the nontrivial elastic effects appear in third order in n and μ. In order to consistently treat elasticity, one has to proceed to a third order perturbation. One replaces ε by $\varepsilon = \varepsilon_1 + \varepsilon_2$ in Eqn. (4.12):

$$0 \approx \frac{n\pi}{2}(\varepsilon_1+\varepsilon_2) + \frac{1}{3}(\frac{n\pi}{2}(\varepsilon_1+\varepsilon_2))^3 + n\pi\mu(1+\varepsilon_1+\varepsilon_2) + \frac{1}{3}(n\pi\mu)^3\xi^2(1+\varepsilon_1+\varepsilon_2)^3 \qquad (4.15)$$

Expanding Eqn.(4.15) to first order in ε_2, the analog of Eqn.(4.13) reads

$$\begin{aligned} 0 \approx\ & n\pi\mu + \frac{1}{3}(n\pi\mu)^3\xi^2 + \varepsilon_1\left[\frac{n\pi}{2} + n\pi\mu + (n\pi\mu)^3\xi^2)\right] \\ & + \varepsilon_1{}^2(n\pi\mu)^3\xi^2 + \varepsilon_1{}^3\left[\frac{(n\pi)^3}{24} + \frac{1}{3}(n\pi\mu)^3\xi^2\right] \\ & + \varepsilon_2\left[\frac{n\pi}{2} + n\pi\mu + (n\pi\mu)^3\xi^2) + 2\varepsilon_1(n\pi\mu)^3\xi^2 + \varepsilon_1{}^2(\frac{(n\pi)^3}{8} + (n\pi\mu)^3\xi^2)\right] \end{aligned} \qquad (4.16)$$

Solving Eqn. (4.16) for ε_2 and expanding the result to third order in n and μ yields

$$\begin{aligned} \varepsilon_2 =\ & -2\mu + 4\mu^2 - 8\mu^3 - \frac{2}{3}(n\pi)^2\mu^3\xi^2 - \varepsilon_1 + \varepsilon_1{}^2(n\pi)^2(\frac{\mu}{2} - 2\mu^2 + 6\mu^3 + 2\mu^3\xi^2) \\ & + \varepsilon_1{}^3(n\pi)^2(\frac{1}{6} - \frac{\mu}{3} + \frac{2}{3}\mu^2 - \frac{4}{3}\mu^3 + \frac{4}{3}\mu^3\xi^2 \end{aligned} \qquad (4.17)$$

Inserting ε_1 from Eqn. (4.14) and again expanding to third order in n and μ one finds that most terms cancel. The result is

$$\varepsilon_2 = \frac{2}{3}(n\pi)^2\mu^3 \qquad (4.18)$$

The sum $\varepsilon_{2,tot}$ of ε_1 and ε_2 is

$$\varepsilon_{2,tot} = \varepsilon_1 + \varepsilon_2 = -2\mu + 4\mu^2 - 8\mu^3 - \frac{2}{3}(n\pi)^2\mu^3(\xi^2 - 1) \qquad (4.19)$$

For the third order perturbation one goes back to Eqn. (4.16), where one replaces ε_2 by ε_3 and ε_1 by $\varepsilon_{2,tot}$. Inserting $\varepsilon_{2,tot}$ from Eqn. (4.19) and again expanding to third order in n and μ one finds

$$\varepsilon_3 = 0 \qquad (4.20)$$

The perturbation calculation breaks off at third order and $\varepsilon_{2,tot}$ is the full result. Note that the elastic effects now vanish if $\xi = 1$, as is required from physical intuition. ξ is related to the elastic compliance by

$$\xi^2 = \frac{Z_q^2}{Z_f^2} = J_f\frac{Z_q^2}{\rho_f} \qquad (4.21)$$

Where $J=1/G$ is the elastic compliance. When deriving the shear compliance one plots the fractional frequency shift $\delta f/f\,(=\varepsilon)$ and the fractional shift of half-band half-width $\delta\Gamma/f$ versus the square of the overtone order n² and fits straight lines according to

$$\varepsilon' = \delta f/f \approx A + S_n' n^2 \qquad (4.22a)$$

$$\varepsilon'' = \delta\Gamma/f \approx S_n'' n^2 \qquad (4.22b)$$

From the offset in the plot of the fractional frequency shifts, A, one obtains the film's mass. From Eqns. (4.19) and (4.21) one reads that the film's elastic compliance J_f' is related to the slope in the plot of $\delta f/f$, S_n', by

$$J_f' = \frac{\rho_f}{Z_q^2}\left(1-\frac{3S_n'}{2\pi^2\mu^3}\right) \qquad (4.23)$$

In the following we extend the above analysis to more complicated configurations. It turns out that the equations are much clumsier if, for instance, the loads on both sides are not equal. However, with the formal procedure established, one will not bother with algebraic complications and just perform the series expansions by programs capable of formal algebra like MATHEMATICA. The above steps can be formalized and more complicated geometries are easily covered by just replacing Z_{fr} and Z_{bk} with the appropriate functions.

The essential steps of the perturbation calculation are:

(1) Expand the total impedance Z_m to third order in μ (cf. Eqn. (4.12).

(2) Expand the result from step (1) to first order in ε (cf. Eqn.(4.13).

(3) Set the result from step (2) equal to zero and solve for ε to obtain the first order perturbation result ε_1 (cf. Eqn. (4.14)).

(4) Expand ε_1 to third order in n and μ (cf. Eq. (4.14).

(5) Replace ε by $\varepsilon_1+\varepsilon_2$ in step (1) (cf. Eq.(4.15))

(6) Expand the result from step (5) to first order in ε_2 (cf. Eqn.(4.16).

(7) Set the result from step (6) equal to zero and solve for ε_2 (cf. Eqn.(4.17).

(8) Expand ε_2 to third order in n and μ. The second order perturbation result is $\varepsilon_{2,tot} = \varepsilon_1+\varepsilon_2$. (cf. Eqns.(4.18) and (4.19).

(9) Go back to step (5) and replace ε_2 by ε_3. Also replace ε_1 by ε_{2tot}.

(10) Repeat steps (6) – (9) incrementing the perturbation order until the calculation breaks off, that is, until the resulting ε_i is zero. This will usually happen at third order.

If one is interested in a more accurate calculation, one may replace all expansions to third order by expansions to fifth (or higher) order.[WJ00] The fifth order result for the symmetric situation (both surfaces covered with films of the same kind) is

$$\varepsilon \approx -2\mu + 4\mu^2 - 8\mu^3 + 16\mu^4 - 32\mu^5 + \frac{2}{3}(\pi n)^2(-\mu^3 + 8\mu^4 - 40\mu^5)$$
$$(\xi^2 - 1) + \frac{2}{15}(\pi n)^4 \mu^5(-2\xi^4 + 5\xi^2 - 3) \qquad (4.24)$$

For a single film on just one surface (cf. Sec. IV) the fifth order result is

$$\varepsilon \approx -\mu + \mu^2 - \mu^3 + \mu^4 - \mu^5 + \frac{1}{3}(\pi n)^2(-\mu^3 + 4\mu^4 - 10\mu^2)(\xi^2 - 1)$$
$$+ \frac{1}{15}(\pi n)^4 \mu^5(-2\xi^4 + 5\xi^2 - 3) \qquad (4.25)$$

By expanding all terms to an order higher than three, a nonlinear dependence of $\varepsilon = \delta f/f$ on n^2 can be captured. In general, it seems more reasonable to address this problem by numerical solution of the equation $Z_m = 0$. In this way piezoelectric stiffening and elastic dispersion are covered as well.

4.1.3 SINGLE FILM ON ONE SURFACE

The symmetric case was treated in full detail because it is arithmetically the simplest one. In practice, one will usually have to deal with just one film, that is, with an asymmetric situation. When the back side is not covered ($Z_{bk} = 0$), the total impedance cannot be simplified as in Eqn. (4.1). However, the formalism works the same way. The resonance condition now is (cf. Eqn.(4.4))

$$0 = \frac{Z_{fr} \tan(\frac{n\pi\varepsilon}{2}) - Z_{fr} \cot(\frac{n\pi\varepsilon}{2}) - 2iZ_q}{Z_{fr} - 2iZ_q \cot(\frac{n\pi\varepsilon}{2})} \qquad (4.26)$$

Inserting Eqn. (4.6) for Z_{fr} and expanding to third order in n and μ results in

$$0 = \frac{n\pi\varepsilon}{2} + \frac{(n\pi\varepsilon)^3}{24} + \frac{n\pi\mu(1+\varepsilon)}{2} + \frac{(n\pi)^3\mu^2\varepsilon}{8}(1+\varepsilon)^2 + \frac{(n\pi\mu)^3(1+\varepsilon)^3}{6}\xi^2 \qquad (4.27)$$

Expanding to first order in ε yields (cf. Eqn.(4.12))

$$0 = \frac{n\pi\mu}{2} + \frac{(n\pi\mu)^3}{6}\xi^2 + \varepsilon\left(\frac{n\pi}{2} + \frac{n\pi\mu}{2} + \frac{(n\pi)^3\mu^2}{8} + \frac{(n\pi\mu)^2}{2}\xi^2\right) \qquad (4.28)$$

Solving Eqn. (4.28) for ε and expanding the result to third order in n and μ yields

$$\varepsilon = -\mu + \mu^2 - \mu^3 - (n\pi)^2 \mu^3 (\frac{\xi^2}{3} - \frac{1}{4})$$

(4.29)

Replacing ε by $\varepsilon_1 + \varepsilon_2$ in Eqn. (27), expanding to first order ε_2, and solving for ε_2 yields

$$\varepsilon_2 = -\mu + \mu^2 - \mu^3 + \frac{(n\pi)^2 \mu^3}{4} \xi^2$$
$$+ \varepsilon_1 [((n\pi)^2 \mu^3 - 1) + \varepsilon_1^2 (n\pi)^2 (\frac{\mu}{4} + \mu^3 (\xi^2 + 1))$$
$$+ \varepsilon_1^3 \frac{(n\pi)^2}{6} (1 - \mu + 4\mu^2 + 4\mu^3 (\xi^2 - 1)]$$

(4.30)

Inserting Eqn.(4.29) into Eqn.(4.30) and expanding the result to third order in *n* and μ yields

$$\varepsilon_2 = \frac{1}{12} (n\pi)^2 \mu^3 \qquad (4.31)$$

and

$$\varepsilon_{2,tot} = -\mu + \mu^2 - \mu^3 - \frac{1}{3} (n\pi)^2 \mu^3 (\xi^2 - 1) \qquad (4.32)$$

Again, the perturbation calculation breaks off at third order *($\varepsilon_3 = 0$)* and Eqn. (4.32) is the full result, which we use later for the calculation of elastic shear modulus (see Fig. 4.6).

4.2 Experimental

Quartz crystal resonance can be excited across an air gap, i.e. the quartz resonance can also oscillate in an electric field applied externally (see Fig.4. 4). Both of the copper electrodes are about 0.5 mm above or below the quartz crystal.

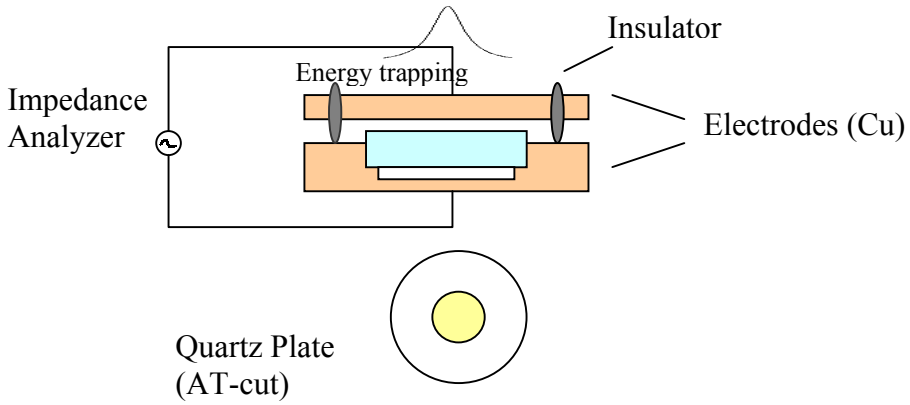

Figure 4.4: Schematic of experimental setup for quartz crystal resonance excited across an air gap.

The rate of gold evaporation can be controlled quite easily while that for silver fluctuates a lot. Three types of metal evaporation configuration are used: (1) only one side of the quartz crystal is covered with metal film, and the metal film is almost the same size as the quartz; (2) only one side of the quartz crystal is covered with metal film, and the metal film is much smaller , about 2 mm in diameter; (3) one side of the quartz is covered with a small area (2mm in diameter) but large thickness metal film (for energy trapping), while the other side is covered with a large area (10 mm in diameter) metal film. Whether the evaporated metal film is on the upper side or on the lower side of the quartz wafer has a small effect on the quartz resonance: When the film is on the top side of the quartz, the resonance frequency is a little higher than that with the film on the lower side of the quartz.

4.3 Results and discussion

Elastic effect is negligible whenever the film thickness is much less than the wavelength of sound. In this case the film is essentially located in an antinode of the standing shear wave. Since the film does not experience shear, the frequency shift is independent of the film's elastic properties. In this case the shear elastic modulus cannot be calculated: either the higher harmonic overtones cannot be detected because of weak signal, or its calculated shear elastic modulus value is not reasonable (negative or very large), which depends on quartz wafer quality.

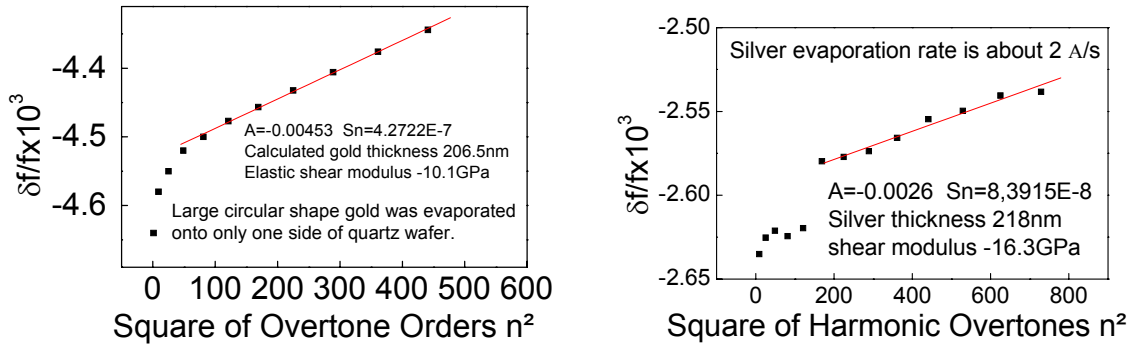

Figure 4.5: Measurement of elastic shear modulus of thin metal films. In these graphs the elastic shear modulus cannot be calculated or the calculated value is not reasonable (negative) because of their smaller thickness.

With a layer of much too thin evaporated metal film on the quartz surface, no change in resonance frequency shift at different harmonic overtones could be measured. In this case the ideal Sauerbrey equation holds. Fig. 4.5 shows, for gold film of 10 mm diameter evaporated onto quartz crystal at a thickness of 206.5 nm, the calculated elastic shear modulus is not reasonable, -10.1 GPa. While for silver film of the same size at a thickness of 218nm, its calculated shear modulus is -16.3 GPa, unreasonable. Usually the shear elastic modulus cannot be rationally measured when the evaporated metal film is too thin, i.e. for gold film the thickness is below 50 nm, and for silver film the thickness below 250nm.

If the evaporated metal film is thick enough, but much thinner than the sound wave length inside the quartz material, we can get a rational value of elastic shear modulus by comparing the resonance frequency shift at different harmonic overtones. For evaporated gold film at a thickness larger than 100nm, and for silver at a thickness larger than 250nm, we can usually get a straight line of $\delta f/f \sim n^2$ and calculate a reasonable elastic shear modulus value. (See Fig. 4.6)

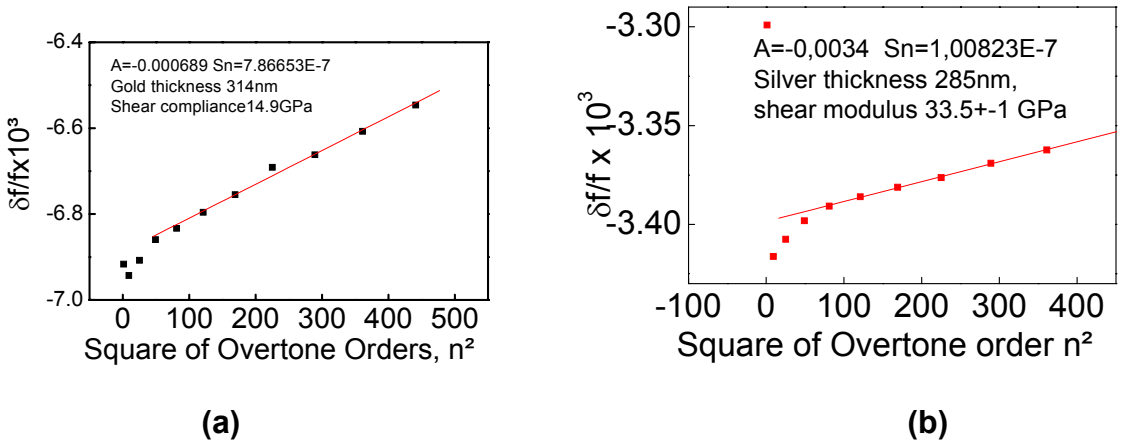

Figure 4.6: Calculation of elastic shear modulus of gold and silver films in large circular form evaporated onto single quartz surface. (a) Gold was evaporated onto quartz plate at a rate of 8A/s. (b) Silver was evaporated onto quartz plate at a rate of 1- 2 A/s.

Fig. 4.7 compared the effect of different gold configurations and evaporation rates on the measured elastic shear modulus. Fig. 4.7 (a) shows that gold configuration has a small effect on the measured elastic shear modulus: when gold was evaporated in a larger area, with or without back electrode, the measured elastic shear modulus is a little larger than that of small area gold. When gold thickness is below 200nm, this effect is much larger; but the chance to get a reasonable positive value is not so large because of the much thinner film.

Fig.4.7 (b) shows that gold evaporation rate has no effect on the measured elastic shear modulus. We may think that evaporation rate doesn't change the structure of evaporated gold. Both (a) and (b) show that the measured elastic shear modulus gets a little smaller with film thickness. With a much thicker film (>500nm) the quartz resonance (at the smallest resonance frequency) becomes bad and the computer fitting is also not good, and the resonance signal looks very bad and not stable and has a hairy look.

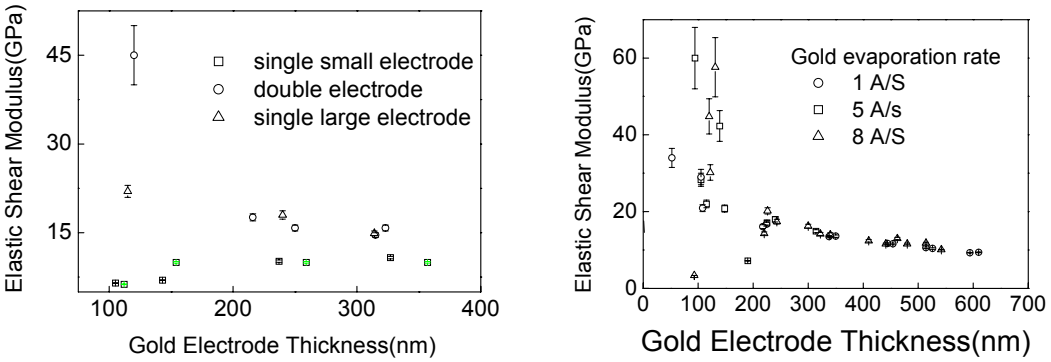

(a) Gold evaporation at different configurations; (b) Gold was evaporated at different rates.

Figure 4.7: Shear modulus measurement results of gold films on small quartz wafers (of 10mm diameter). (a) Gold was evaporated at a rate of 5 A/s, but with different configurations; (b) Gold was evaporated at a large single configuration but at different rates (1, 5, and 8 A/s).

For the measurement of silver elastic shear modulus, the chances of getting a reasonable positive value are much smaller than that of gold. Fig. 4.8 shows that only a few data points can be collected for silver elastic shear modulus measurements in the single circular form. In general, there is a similar trend as that for gold film: the measured elastic shear modulus decreases with increasing thickness.

After metal evaporation the quartz surface roughness enlarges, which can be confirmed by AFM measurements. Maybe the increased roughness is the main reason for the decrease of measured elastic shear modulus. This can also be confirmed by the fact: for the first layer of evaporated gold, the calculated gold thickness using our method is the same as that detected by the evaporation machine; but for the metal film with two or more layers, the calculated thickness is larger than the sum of machine readings of every time evaporation.

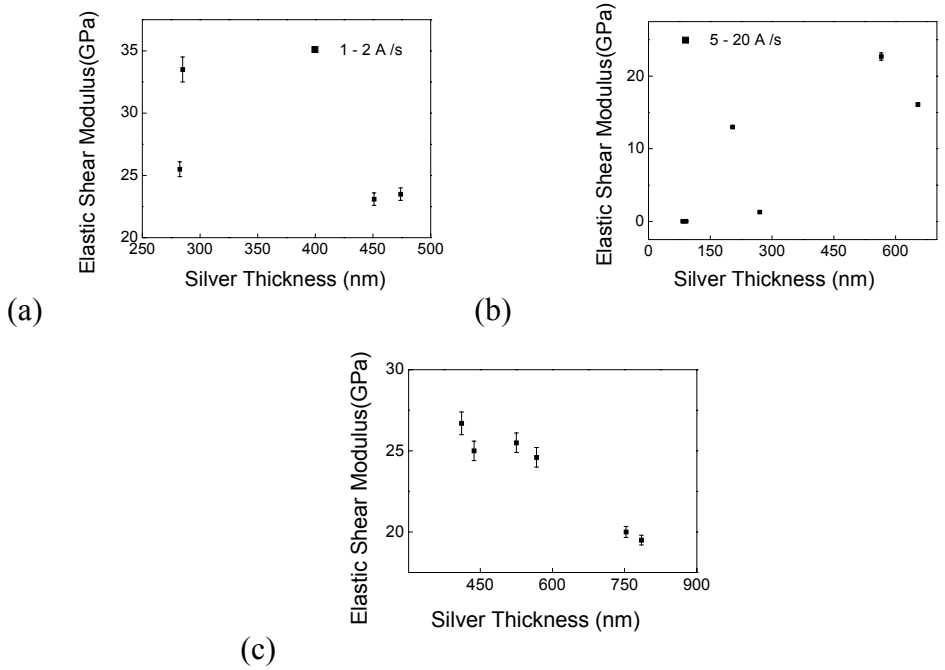

Figure 4.8: Shear modulus measurement results of silver films on 5 MHz 14mm diameter quartz wafers: (a) silver was evaporated onto the blank quartz wafer at a rate of 1-2 A/s in a single large circular form; (b) silver was evaporated onto the blank quartz wafer at a rate of 5-20 A/s in a single small circular form; (c) silver was evaporated onto the quartz wafer with 600nm thick back electrode at a rate of 5-20 A/S in a single large circular form.

Table 4.1 summarizes the theoretical and measured values of shear elastic modulus for gold, silver, copper, aluminum and quartz. The measured elastic shear modulus is smaller than the theoretical bulk value, which shows the difference between thin films (several hundred nanometers) and bulk materials. Maybe this is because of the surface roughness, or surface defect of thin metal films.

Table 4.1: Comparison of elastic shear modulus values of some evaporation materials[5]

	gold	silver	copper	aluminum	SiOx
Density (10^3 kg/m^3)	19.3	10.5	8.9	2.7	2.65
Velocity of Sound (m/s)	1740	2600	3570	5100	3325
Acoustic Impedance (10^6 kgm^{-2}s^{-1})	23.6	16.7	20.3	8.22	8.8
Slope Sn	> 0	> 0	> 0	< 0	~ 0
Elastic Shear Modulus (GPa)	28.9	26.6	46.0	25.0	35.2
Experimental value (GPa)	~15	~20	-	-	-

4.4 CONCLUSIONS

The elastic compliance of thin films deposited on quartz resonators can be inferred from comparison of the shifts in frequency on various overtones. While the full analysis requires the numerical solution of $Z_{el}(\omega)=0$, considerable insight can be gained from approximate solutions. When plotting the fractional frequency shift $\delta f / f$ versus the square of the overtone order n^2 a linear relationship emerges. The slopes contain the elastic compliance J'.

It is found that the metal evaporation rate and configuration of metal evaporation don't have an obvious influence on the elastic shear compliance J'. In this way the measured elastic shear modulus values of gold and silver are much smaller than their theoretical values, which imply that the material properties at nanometer level differ greatly from those of bulk material.

[5] data adapted from web page http://www.webelements.com, and Handbook of Chemistry and Physics, 74th ed. 1993 -1994.

5 Deposition of Mercury on Self-Assembled Monolayers (SAMs) Covered Gold Surface

This chapter presents the deposition of mercury (Hg) on alkanethiol and alkanedithiol SAMs on Au (111). The work was primarily conceived from finding ways to easily characterize the binary mixtures of SAMs of 1-octanethiol and 1,8-octanedithiol. The first idea was to use the selectivity of the physical vapor deposition (PVD) process to determine the distribution of SH- group in the matrix of CH_3- head groups by depositing an atomic layer of Hg on the mixed SAM. Instead of serving for its original purpose, the AFM results obtained posed an interesting question regarding the physical state of Hg deposited on top of SAMs: does Hg form nano-droplets (liquid) or nano-particles (solid crystal) under ambient conditions? In other words, is there long range order or short range order inside mercury nano sized particles at room temperature? Whether it is liquid or solid plays an important role in vast field of research on Hg applications.

5.1. Introduction

5.1.1. Redox catalytic property of Hg nanoparticle

Mercury has been the subject of several electron transfer studies. [JP01][BHM98] Electron transfer mechanism plays an important role in many homogeneous and heterogeneous reactions. [WGM87][Com89] In this process, a large barrier for the electron transfer between donor and acceptor may occur, which might restrict the passage of an electron. An effective catalyst with an intermediate redox potential value of the donor-acceptor pair helps the transfer of electrons from donor to acceptor and acts as an electron relay medium. [ZGS86] [HPH94] [SS94] [Sch92] [LEW93]

Metal ions or metal particles are well known examples of this type of redox catalyst. Jana *et al*. have successfully demonstrated the redox catalytic properties of small mercury particles using methylene blue as a redox probe. [JP01] They showed the possibility of electron transfer from the reducing agent to the dye via the Hg nanoparticles which act as electron transfer catalyst (Fig. 5.1).

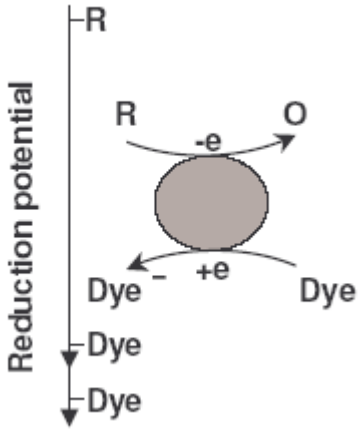

Figure 5.1: Proposed mechanism for Hg nanoparticle catalyzed redox reaction, Adapted from Reference [JP01])

5.1.2. Liquid Hg: a useful metal in molecular electronics

Another important application of Hg is to aid the flow of electrons through organic matter, which is important in a number of applications, such as electron transfer in biological molecules, fabrication of microelectronic devices and sensors and development of molecular electronics. In these aspects Hg has been commonly used as a metallic substrate [HHC^{+}01] [RSW98] [HHI^{+}99] [HRW98] [BHM98] or simply as an electrode. [HRH^{+}99] [KMT00]

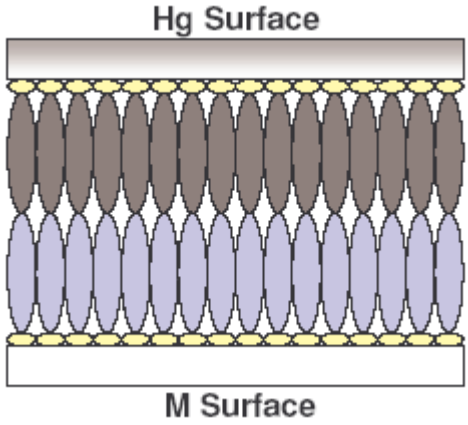

Figure 5.2: Schematic representation of M (Ag or Au)-SAM (1) SAM (2)-Hg junction.

Mercury offers several advantages; first, it allows to readily forming self assembled monolayers of alkanethiols which have been structurally characterized. Second, it is a liquid at room temperature. A liquid Hg surface supporting a SAM is compliant and can conform to the topography of a solid surface with which it is brought in contact. This ability to conform minimizes the effects of irregularities of the solid surface on the structure of the SAMs. This further provides the SAMs with better passivating properties (much smaller number of

defects) and stability making them a suitable candidate for application in nano- and molecular scale electronic devices (Figure 5.2).

Hg nano-particles were usually prepared via solution chemistry by the reduction of Hg_2Cl_2 solution with $NaBH_4$. In this work, preparation of Hg on SAMs was done under ambient conditions employing similar sample preparation method used by Grunze and co-workers. [THZ+98] The main difference was that Grunze *et al.* used only alkanethiol SAMs since their study focused on the changes of molecular structure of methyl terminated alkanethiol SAMs on polycrystalline gold resulted from exposure to Hg vapor, in which an increasing lateral chain density in SAMs of alkanethiols on Au was realized after exposure of alkanethiol monolayer to Hg vapor and subsequent immersion inside the thiol solution. Whereas, in this work, the deposition and phase study of Hg on alkanedithiol SAMs were focused after it formed a covalent bond with the thiol head groups. SAMs of alkanethiol and alkanedithiol on atomically flat Au (111) surface were used as matrix for Hg. The deposited Hg on SAMs was first characterized with AFM techniques and its liquid-solid phase transition was monitored by Quartz Crystal Microbalance (QCM).

5.2 Experimental Section[6]

5.2.1. Preparation of SAMs

Self assembled monolayers of alkanethiol and alkanedithiol were prepared by dipping the freshly prepared Au (111) surface on mica inside 1 mM solution of 1-octanethiol and 1,8-octanedithiol in ethanol for 15 hours, respectively. For QCM experiments, clean gold electrode surface on quartz crystals was used as substrate for SAMs.

5.2.2. Deposition of Hg on SAMs of 1-octanethiol and 1, 8-octanedithiol

A drop of pure Hg was placed inside a small capped Petri dish and kept at room temperature for 30 minutes to reach a saturation of mercury vapor in air. Then the prepared SAM sample was put inside the closed Petri dish with the mercury drop. The prepared SAM samples were exposed to mercury vapor at room temperature for a period ranging from 20 min to 2 days in an atmosphere saturated with mercury vapor. At room temperature (25 °C) the saturated vapor pressure of Hg in air is 0.0017 mbar (0.17 Pa). This corresponds to a mercury vapor concentration of 13.6 mg/m^3 in air. [FR92]

5.2.3. Atomic Force Microscopy (AFM)

AFM images were acquired using a Nanoscope™ IIIa Atomic Force Microscope (Digital Instruments, Santa Barbara, California). Imaging was done in contact mode under ambient conditions. Silicon nitride cantilevers of 100 μm length (spring constant 0.1 N/m) with integrated sharpened tips (Olympus, Tokyo, Japan) were used.

5.2.4. Quartz Crystal Microbalance Measurement

The experiment was performed using the Impedance Analyzer HP E5100A (100 kHz – 300 MHz). The quartz crystals used were purchased from LUNE GmbH and had a diameter of 14 mm and a fundamental resonance frequency of 4 MHz. The measuring cell (a brass chamber) with temperature control from –100 °C to 200 °C was customer made in the Mechanical and Electronics Workshops at Max-Planck Institute for Polymer Research (MPIP) in Mainz. Low temperature was achieved by using dry ice, which has a melting point of –56.6 °C (5.11 atm) and a sublimation point of –78.5 °C (at 1 atm).

The deposition of Hg on alkanedithiolate SAMs was performed in time from 20 minutes to 2 days and monitored on line at room temperature by QCM using various possible harmonics. The experimental procedure was as follows: a small drop of pure Hg was placed about 1 cm directly under the horizontally installed quartz wafer inside the measurement cell. The working electrode of the QCM wafer was downwards and facing the mercury drop. Then, after a certain deposition time, a QCM temperature scan from room temperature to –75^{o}C and reversed from -75°C to room temperature was performed.

5.3. Results and Discussion

5.3.1. Particle-like behavior of Hg on SAMs by AFM

AFM analysis was performed to determine the surface morphology of the deposited Hg on SAMs. Fig. 5.3 shows AFM images of Hg on SAMs at different exposure times. Relatively flat surfaces were shown in Fig.5.3 (a) and 5.3(b) with only a SAM on the surface before mercury exposure. The terraces of Au (111) around 200-300 nm thick on mica substrate are clearly observed. Exposure of 1,8-octanedithiolate SAMs to saturated Hg vapor for 20 min gave particle like morphologies on the surface (Fig. 5.3(c)). The structures have an elongated spherical shape, which is independent of the scanning direction, and a height ranging from 1 to 5 nm (Figure 5.4A).

[6] in cooperation with Anne K. Aliganga in MPIP in Mainz.

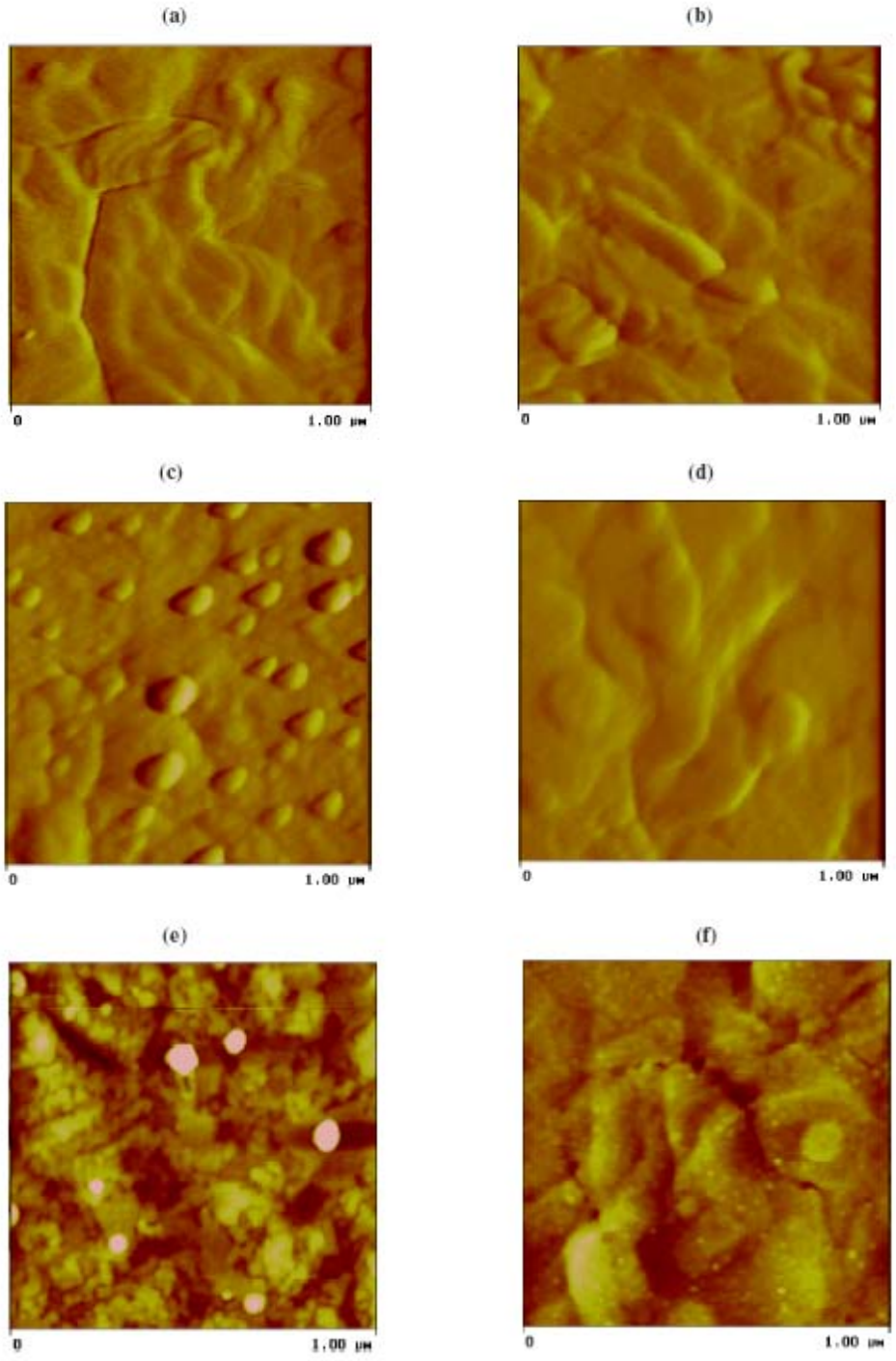

Figure 5.3: AFM images of SAMs of (a) 1,8-octanedithiol (C8-DT), and (b) 1-octanethiol (C8-T) on Au (111), and AFM images of PVD Hg on SAMs of (c) C8-DT and (d) C8-T after 20 minutes, and PVD Hg on SAMs of (e) C8-DT and (f) C8-T after 48 hours exposure.

To further confirm the selectivity of the PVD process, a parallel deposition experiment of Hg on 1-octanethiol with CH_3– head groups was performed, and the AFM image is shown in Fig.5.3 (d). There were, this time, no particulate structures found in Figure 5.3(d), compared to the structures observed in Fig. 5.3(c).

However, increasing the deposition times of Hg to 2 days gave well-packed aggregates of particle like structures for the dithiol head groups (Fig.5.3(e)); whereas, spherical particle-like structures with height ranging from 6Å to 2 nm (Fig. 5.4B) were obtained for the 1-octanethiol SAM with CH_3- head groups (Fig.5.3(f)). At this point, it would have been tempting to say that nano-particles of Hg were deposited onto the 1,8-octanedithiol SAM surface, wherein Hg is covalently bonded to SH- group. Otherwise the structures would have been removed or destroyed after several scans with the AFM needle on the surface. However, the high surface tension of Hg, which kept the nanostructures intact on the surface while scanning with the AFM needle, could not be ignored in this case. The interfacial tension of Hg in air is 485.48 × 10^{-3} N/m under laboratory conditions, which is approximately 7 times higher than the surface tension of water (71.99 × 10^{-3} N/m), and 10 times larger than that of common liquids. [Lid93]

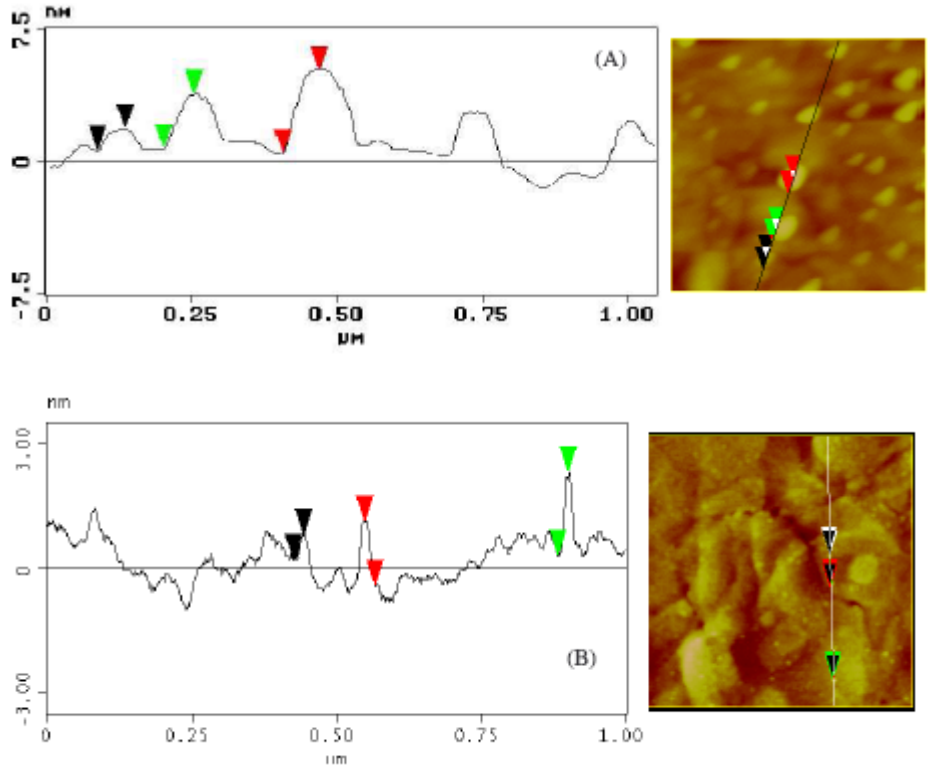

Figure 5.4: Section analysis of the flattened AFM image of (A) PVD Hg on C8-DT and (B) PVD Hg on C8-T after 48 hours exposure to saturated mercury vapor. (Representative of at least 5 analyses.)

From the AFM results of the PVD Hg on SAMs of 1-octanethiol and 1,8-octanedithiol, it is difficult to distinguish whether Hg nano-particles or nano-droplets were deposited onto the SAM surface. In this regard, QCM experiments were employed to reveal the phase state of Hg on SAMs.

5.3.2. The liquid-solid phase transition of mercury on SAMs monitored by QCM

In QCM measurements, the bandwidth can be used to interpret the energy dissipation of various physical or chemical processes occurring on the quartz electrode surface. [KSC91] The resonance of the quartz crystal microbalance is dampened by a liquid in contact to its surface much more than by a solid film adsorbed onto its surface in air. The first few molecule layers of the liquid in contact of the QCM surface may undergo acoustic shear movement induced by quartz resonance, and the QCM measurement embodies the typical viscous property of the liquid. The viscosity of liquid in contact to the quartz surface can be calculated according the following equation (5.1).

$$\eta' = -\frac{\pi Z_q^2}{n\rho f_0^3}\delta f \delta\Gamma \qquad (5.1a)$$

$$\eta'' = -\frac{\pi Z_q^2}{n\rho f_0^3}(\delta f^2 - \delta\Gamma^2) \qquad (5.1b)$$

where complex viscosity $\eta^* = \eta' - i\,\eta''$, n is the overtone number, ρ is the density of the liquid, f_0 is the fundamental resonance frequency, $Z_q = 8.8\times10^6\ kg/m^2s$, is the acoustic impedance of the quartz material, δf is the resonance frequency shift, and $\delta\Gamma$ is the half-band-half-width shift. For ideal liquids, $\delta f = \delta\Gamma$, according to equ. (5.1b), the complex part of viscosity is 0, which means no elastic but only pure viscous property.

The viscous drag of liquids results in a frequency shift, which is a priori not separable from the effect of deposited mass, or a few molecule layers adsorbed onto QCM surface. [Joh99] For an ideal liquid the viscosity leads to an increase in bandwidth as large as the resonance frequency shift, which allows in principle for a separate determination of adsorbed mass and viscosity. [LW95] Solid films adsorbed onto QCM surface can decrease the resonance frequency, but the change in half-band-half-width is not as significant as compared to that in liquid, because of their elastic properties. Based on this concept, the melting point (or freezing point) of a number of materials can be measured by detecting the transition point in the fractional half-band-half-width shift in QCM resonance measurement.

Quartz resonators themselves may display time dependent behavior such as slow response or overshooting on the time scale of fractions of a second when they are subjected to rapidly changing environmental conditions. These effects are particularly evident when the process of interest is accompanied by gradients of temperature or pressure. To account these effects in our QCM measurement, a blank QCM temperature scan in air was performed before QCM temperature scan measurement with Hg on SAMs (Fig.5.5). The quartz resonators used in this experiment displayed good quality since its overtone spectrum could be well examined

beyond $n = 20$, which is characteristic for good quartz blanks. Fig. 5.5(b) shows the fractional frequency shift (δf/f) and the fractional half-band-half-width shift (δΓ/f) of blank quartz on different harmonics as a function of temperature. The resonance frequency of the quartz crystals behaved in a linear way with temperature. The frequency shift decreases smoothly with decreasing temperature. The fractional half-band-half-width (δΓ/f) changes of different harmonics differ slightly with temperature. A remarkable noise, which was observed at 0 °C in half-band-half-width shift for 195 MHz harmonic, was caused by the water vapor in air freezing on the quartz surface.

The temperature was well recorded throughout the experiments as shown in Fig. 5.5 (b) and Fig.5.7 (b), as the low temperature was made possible by the natural melting of dry ice. Sometimes, when the temperature decreased too much in a second because of too much dry ice was kept in contact of the measurement cell, the temperature sensor (PT 100) might be out of order, and the whole measurement would be ruined.

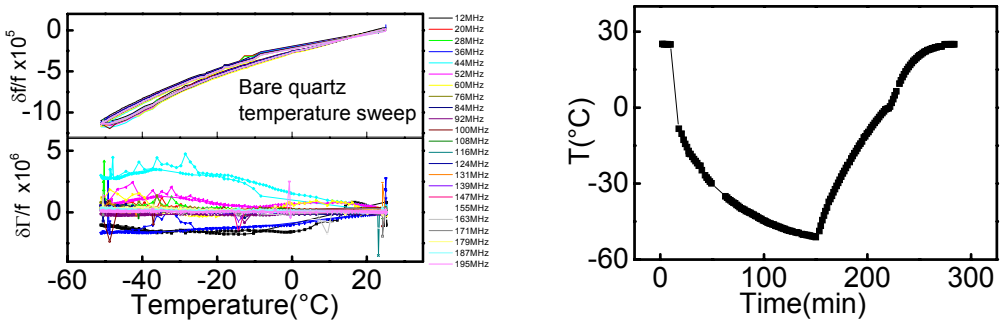

(a) (b)

Fig. 5.5: Temperature sweep of bare quartz crystal: (a) fractional resonance frequency shift and fractional half-band-half-width change with temperature; (b) temperature change with time.

The deposition of mercury was shown by the decrease in resonance frequency and the slight broadening in half-band-half-width (Fig. 5.6), which is usually observed in normal membranes. [AAK94][YFL00][SB93]

Using the Sauerbrey equation (equation 2.1.1.3), the adsorbed mass of Hg, δm, can be deduced from a linear relation between adsorbed mass and measured changes in the resonance frequency, δf, i.e. an approximately 3 nm thickness of Hg was deposited onto the quartz surface after 21 hours. This thickness means that there is mercury with an equivalent thickness of 3 nm deposited onto quartz surface, but the exact mercury configuration cannot

be detected with QCM. The plot of fractional half-band-half-width vs. time shows the dissipation change in energy, which further describes the viscoelastic property of the material. Figure 5.6 shows no obvious increase in bandwidth with time. It seems that a solid Hg was deposited onto the surface. But, when calculating the viscosity, the value obtained for its lower limit is 2.1 mPaS, which differs remarkably from the literature value of 1.5 mPaS. [Lid93] At this point, there is no proof on whether deposited Hg is liquid or solid. A QCM temperature scan measurement was needed to show the liquid-solid phase transition of Hg, if existing.

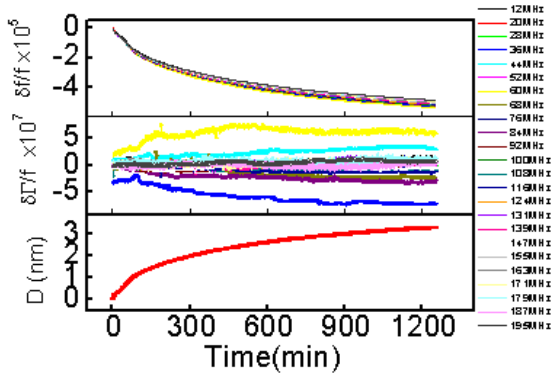

Fig. 5.6: Deposition of Hg on SAMs as monitored by QCM at 25 °C for 21 hours. (a) Fractional frequency shift $\delta f/f$ and (b) fractional half-band-half-width shift $\delta\Gamma/f$ versus time. (c) Real time monitor of the thickness of the deposited Hg.

Fig. 5.7 shows the QCM temperature sweep of Hg on 1,8-octanedithiol SAM covered gold electrode surface. During the whole temperature scan period, the mercury was kept below the quartz surface, to make sure that the measurement environment is saturated with mercury. There are no abnormalities revealed in the frequency shift measurement, and it shows an almost smooth linear relationship with temperature as observed in Fig.5.7(a) and (c). There seems to be no difference in fractional frequency measurements before and after mercury was deposited onto the SAM covered quartz surface. At the beginning temperature (25 °C) and end temperature (-76 °C) the noise signals observed in fractional half-band-half-width shift measurement were also observed for the bare quartz measurement as shown in Fig. 5.5. This is probably an inherent response of the quartz crystal caused by an abrupt temperature change. The step down in fractional half-band-half-width shift at 0 °C was consistently observed, which was attributed to the phase transition of water (freezing and melting of water). However, there was a strong signal at about -58.6 °C (in the cooling down

process) and -34.3 °C (in the warming up process) as revealed in the plot of fractional half-band-half-width shift versus temperature (Fig. 5.7(b)). We may take these temperature points as the measured transitional temperature. Around transition points, the bandwidth becomes much larger than normal, and later it gets normal again.

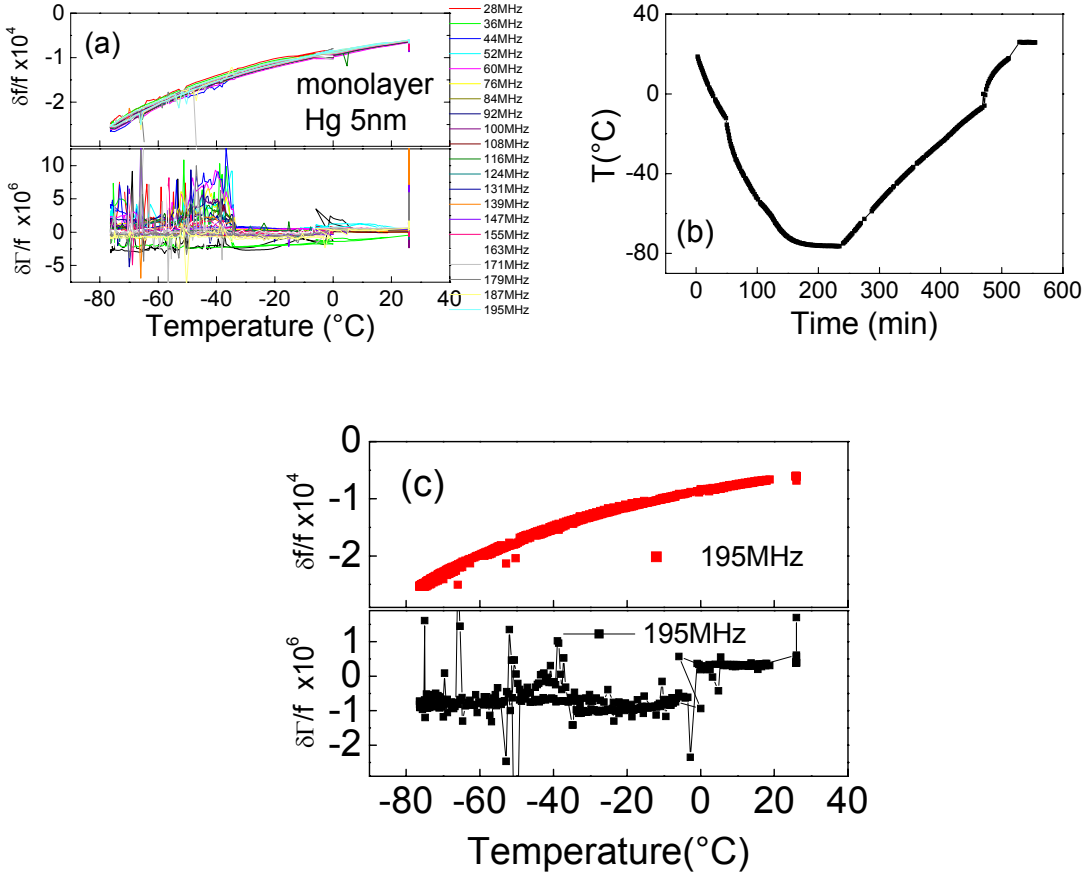

Figure 5.7: QCM temperature sweep of Hg on a SAM of 1,8-octanedithiol on Au-coated quartz surface: (a) fractional frequency shifts and half-band-half-width change at various harmonics, (b) temperature program, (c) fractional frequency shifts and half-band-half-width at 195 MHz.

Taking a closer look at the fractional frequency shifts and half-band-half-width at 195 MHz (Fig. 5.7(c)), the phase transition of Hg is observed at a temperature of -34.3 °C (literature melting point of Hg is -38.83 °C). [Lid93] This observed transition point of Hg could explain the remarkable difference in the dissipation energy on the surface from -58.6 °C (cooling down) to -34.3 °C (warming up). The behavior at around -58.6 °C is possibly a characteristic response of solid Hg on the surface to the shear stress applied. In the measurement at temperatures below -20 °C a discrepancy of –4 °C of the measured transition temperature

from the true value was observed (see ice-water transition at 0°C). This was proved to be dependent on the cooling and/or warming up rate after several repeat measurements. An improvement of the measurement system to make the difference between the measured melting temperature and the actual value of Hg negligible and less dependent of the temperature sweeping rate will be a much too difficult work.

The temperature change with time is shown in Fig. 5.7(b). At 195 MHz harmonic, it is clearly shown how the half-band-half-width fluctuates with the change in temperatures as shown in Fig. 5.7(c). During the transition of the material from liquid to solid, molecules begin to arrange in a crystalline order and release the heat of crystallization. This arrangement from short range order in liquid to long range order in single crystalline and energy transfer process produce a strong noise signal in QCM half-band-half-width shift, revealing further change in energy dissipation of the QCM, thus, showing the phase transition of the material.

In liquids there is a short range order long range disorder in molecule arrangement. Inside nanometer sized droplets, there are chaotic movements of molecule groups. Mercury atomic radius is 1.5 Ångstrom, and a 3 nm large Hg droplet has about 10 atoms in one direction, as it is in our experiment confirmed by both QCM and AFM measurements. In such a mesoscopic phase, some Hg atoms may get away from the droplet surface and meanwhile some Hg atoms from the environment deposit onto the droplet, it is really not easy to detect the difference between the solid and liquid nanometer sized particles. For mercury nano particles below melting point, the Hg atoms are difficult to get away from the particle surface, and they are fixed in their positions in a long range order, but it is sure that there are still weak movements of the atoms. There is no obvious difference in the fractional half-band-half-width shift with temperature between much above the melting point and much below the melting point. Because of the short range order in liquid nano droplet, there is no relative movement between adjacent atomic layers induced by quartz resonance, and the QCM measurement shows only the elastic properties instead of the viscous properties of the adsorbate. However, a QCM temperature scan may show that there is really a phase transition around its melting point because of molecule rearrangement and the corresponding energy involved. We have performed the similar measurement for phenol with a similar result.

It is here worthwhile noting that laser beam may make a much larger change in resonance frequency shift than in bandwidth shift of QCM measurements, because of thermally induced stress relaxation in the gold electrode; while the phase change between nano-droplets and

naon-particles occurring on the gold surface makes a much more obvious change in bandwidth than in resonance frequency shift, because of molecule rearrangement and the corresponding energy transformation occurring on quartz surface.

5.4 Conclusions

Deposition of Hg on 1,8-octanedithiol SAM under ambient laboratory conditions was successfully demonstrated. The deposition process showed selectivity at a deposition time of 20 min producing nano sized droplets of Hg. The physical state of the deposited Hg could not primarily be determined with AFM technique because the high surface tension of Hg keeps the droplets undistorted by the scanning of the AFM needle.

However, based on the QCM temperature measurement results, the deposited Hg could be taken as liquid. The QCM temperature sweep with mercury on a 1,8-octanedithiol SAM covered Au (111) surface shows the phase transition points of Hg from liquid to solid or vice versa around -58.6°C (from liquid to solid) and –34.3 °C (from solid to liquid). The QCM technique was an excellent tool in this study to determine the physical state of the deposited Hg. Around the phase transition points of mercury, there was almost no change in QCM resonance frequency shift, but there was actually a strong signal in its half-band-half-width shift.

The phase transition of water was also observed from the fractional half-band-half-width shift, wherein atmospheric vapor freezes onto quartz surface and ice droplets adsorbed onto the quartz surface melt around 0 °C. This further confirmed the sensitivity of the QCM technique.

Around phase transition point, there is a strong signal in bandwidth shift, and the bandwidth may get much larger than normal, while the resonance frequency remains almost the same.

6 Swelling of chitosan film in different PH solutions

Chitosans are a family of linear, cationic polymers [Muz73] [Muz88] obtained by deacetylating the biopolymer chitin, which is found in the skin or shell of anthropods. As the degree of deacetylating (DD) of chitinous material exceeds 50%, it becomes soluble in acidic aqueous solution and is called chitosan. It is a random copolymer of 1,4 linked 2-acetamide-2-deoxy-β-D-glucopyranose and 2-amino-2-deoxy-β-D-glucopyranose residues. This biopolymer is polycationic, i.e. positively charged at pH<6. Due to the protonated amino groups (the amino group in chitosan has a pKa of 6.5) [PCB83] [RD89], chitosan in dilute acid aqueous solution exhibits a polyelectrolyte character at low pH. The physical chemical properties of chitosan solutions depend on temperature, pH, ionic strength, surfactant concentration and DD. Its chain flexibility can be manipulated by changing its charge density along the chain by controlling DD. Chitosan has a numerous applications in industry, pharmacology and biotechnology.

6.1 Experimental--Preparation of buffer solutions and chitosan film[7]

Phosphate and citrate buffer solutions were prepared according to the recipes listed in Tables 6.1 and 6.2. At room temperature (22.7°C), the refractive indexes of milli-Q water, citric buffer (pH=5.8) and phosphate buffer are 1.3333, 1.3358 and 1.3338, respectively.

The chitosan sample had a degree of N-deacetylation of 84%, and it was dissolved in 1% acetic acid, yielding a pH of 3. The weight average molecular weight of the sample is approx. $4x10^5$ and the polydispersity index Mw/Mn=2.7.

Table 6.1: Phosphate buffers with pH range 5.8 – 6.8 used in the measurement were prepared with 0.2M Na_2HPO_4 and 0.2M NaH_2PO_4 solutions.

Buffer No.	1	2	3	4
0.2M Na_2HPO_4 (ml)	92	81.5	73.5	51
0.2M NaH_2PO_4 (ml)	8	18.5	26.5	49
pH value	5.8	6.2	6.4	6.8

[7] in cooperation with Steffen Berg in MPIP.

Table 6.2: Citrate buffers with pH range 7.1 – 4.0 used in the measurement were prepared with 0.1M $C_6H_8O_7$ and 0.2M Na_4HPO_4 solutions.

Buffer No.	5	6	7	8	9	10	11	12
$0.1MC_6H_8O_7$(ml)	60	54	48	44	40	34	26	12
$0.2MNa_2HPO_4$(ml)	40	46	52	56	60	66	74	88
pH value	4	4.5	5.1	5.4	5.8	6.2	6.6	7.1

Chitosan film was spin coated onto a clean quartz at 3000 rpm for 1 min, and dried in air for one hour, then the film was immersed inside borate buffer (pH=9.22) for one hour; after it was dried with nitrogen the film was kept in a ventilator for overnight drying. After that the quartz with chitosan film was installed inside the liquid cell and the film swelling was measured in different buffer solutions.

6.2 Results and Discussion

An illustration of chitosan structure is depicted in Fig. 6.1.

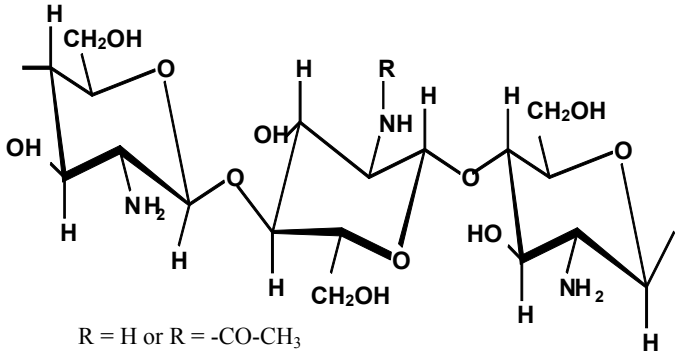

Figure 6.1: Molecular structure of chitosan, a random copolymer of 1,4 linked 2-acetamide-2-deoxy-β-D-glucopyranose and 2-amino-2-deoxy-β-D-glucopyranose residues. $\overline{MW} = 4 \times 10^5$, Mw/Mn=2.7.

As a linear polyelectrolyte, chitosan has both reactive amino groups and hydroxyl groups, thus we expect that the physical and solution properties of chitosan change with the surrounding chemical environment. At pH values above 6.5, which is approximately the pKa value of the amino group in chitosan, chitosan solutions exhibit phase separation. When the pH value is less than approx. 6.5, chitosan in solution carries positive charges along its backbone; at pH values below 4, most of the amino groups of chitosan are supposed to be

protonated, and this protonation strengthens electrostatic repelling between charged groups along the backbone, and it leads to enhanced swelling of the polymer network.

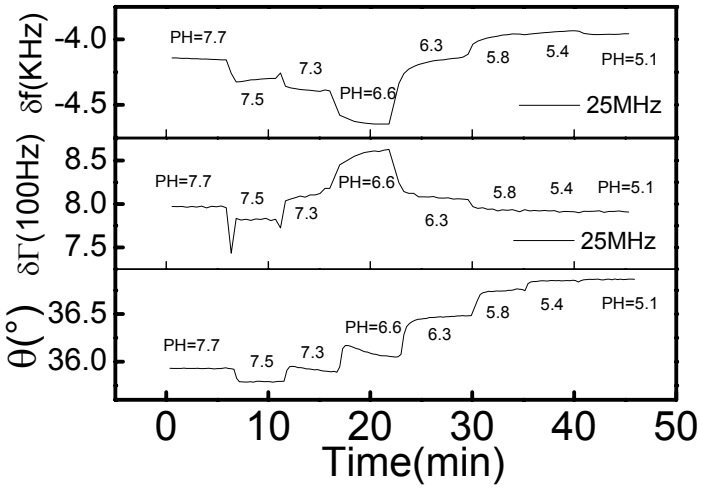

Figure 6.2: Swelling of an 80 nm thick (dry) chitosan film as a function of pH values.

From the SPR graph, we can notice that the chitosan film optic thickness gets larger with decreasing pH values, i.e. chitosan film swells a lot in lower pH buffer solutions. This corroborates the fact that chitosan is hydrophobic and dissolvable at higher pH values; while at lower pH values it becomes hydrophilic and soluble. But the QCM measurement shows a different picture: at high pH values, the film thickness increases with decreasing pH; at pH=6.6, the chitosan film thickness is the largest; and then it deswells with decreasing pH values. It is possible, that some of the chitosan film on quartz surface may dissolve into the buffer solution at pH values below 6.6, but the SPR and QCM measurements show that chitosan film is still remaining adsorbed onto the quartz surface.

6.3 Conclusions

QCM and SPR measurements show different results in the swelling of chitosan film in different pH buffer solutions. Chitosan film swelling dependent on pH and there are other effects such as ion strength, temperature and surfactant. The QCM measurement shows that the swelling behavior of Chitosan has an isoelectric point (pH value between 6.3 and 6.6).

7 Adsorption of linear pNIPAm in water on gold surfaces monitored in situ by SPR and QCM[8]

Interest in the poly (N-isopropyl acrylamide) (pNIPAm) system stems from the fact that it has a fully reversible lower critical temperature (LCST) in water at around 31°C. [Sch92] Since this temperature lies between room temperature and body temperature it is foreseen that pNIPAm could be of interest in biological applications. Above the critical temperature the polymer phase separates from solution, while below LCST, the polymer becomes soluble in water. The lower critical temperature is a result of the entropy gain for the dehydration of the amide moieties with increasing temperature and can be affected by additives such as salt, alcohol, and surfactants and by the variation of the solution pH. [Gra00]

When attached to a solid surface the pNIPAm layer swells and deswells with temperature. In this way one can tune the thickness of the layer and its softness. [AKR00] Gels of pNIPAm show temperature induced shape transformations, which makes them useful as sensors or actuators. [KVW02]

In this work, the properties of pNIPAm layers physisorbed to solid substrates were studied with combined Surface Plasmon Resonance (SPR) [Kno97] measurements with a Quartz Crystal Microbalance (QCM) [HRB$^+$98] [LMJ00] in order to gain structural information on these layers. Both techniques are capable of monitoring the kinetics of adsorption. However, the two techniques are sensitive to different aspects of the process, and hence in-situ comparison can lead to a greater understanding of the mechanisms.

For example, SPR probes a certain combination of thickness and refractive index sometimes also termed the "ellipsometric moment" of the density profile. [CG83] The ellipsometric moment is largely (but not strictly) proportional to the adsorbed amount. The QCM, on the other hand, probes a combination of acoustic impedance and thickness which can be termed "acoustic moment". Importantly, the QCM is sensitive to any adsorbed mass, including solvent associated with the films. In addition, the QCM provides information on the dissipation inside the layer and hence on its viscoelastic properties.

[8] text partly adapted from: M.A. Plunkett, Z. Wang, M.W. Rutland, D. Johannsmann Adsorption of pNIPAM layers on hydrophobic gold surfaces, measured in-situ by QCM and SPR Langmuir 19 **(2003)** 6837.

7.1 Materials and experimental

In this investigation we have monitored the adsorption of the temperature sensitive pNIPAm onto a hydrophobic substrate. The substrate was a gold coated quartz crystal which was hydrophobized by the self-assembly of dodecanethiol. Such self assembled monolayers (SAMs) provide a reliable and convenient way to form stable hydrophobic surfaces. The pNIPAm was purchased from Polymer Source Inc. and was reported to be of an average molecular weight (M_w) of 275 kg / mol (determined via intrinsic viscosity measurements in methanol) with a polydispersity index of $M_w / M_n = 2.75$ (determined via size exclusion chromatography). The pNIPAm was subsequently dialyzed with molecular weight cut-off 10 000 g / mol dialysis tubing to remove any possible low molecular weight contamination before being freeze dried and stored ready for use. The molecular structure of pNIPAm is represented in Fig. 7.1.

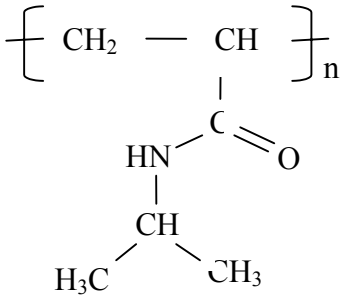

Figure 7.1: Schematic of pNIPAm structure, where *n* is the degree of polymerization.

Adsorptions were conducted in milli-Q water at 31°C. This temperature was chosen as it lies just below the critical point and hence maximizes adsorption without causing a phase separation in the bulk.

Before introduction of the pNIPAm to the system, baselines for both QCM and SPR were measured in milli-Q water. At time zero the polymer was introduced at a bulk concentration of 20ppm and the adsorption process was monitored simultaneously by both techniques. The concentration of 20 ppm is small enough to avoid precipitation of bulk material. Low concentrations are also desirable in order to avoid turbidity of the solution when the phase transition is approached. For turbid solutions, the reflectance minimum of the SPR curve cannot be determined.

The effect of temperature on the conformation of pNIPAm is interesting, however since quartz crystals are affected by variations in temperature we must remove the inherent crystal effects from the measured response in order to investigate the effect of temperature on the

pre-adsorbed polymer layer. This was achieved by measuring the inherent temperature effects on the crystal (14 mm small quartz) prior to the addition of polymer to the system. The temperature was linearly cycled, up and down, between 24°C and 36°C in milli-Q water. It was noted that for constant rate of temperature change there was a reproducible hysteresis between the increasing and decreasing temperature runs for the frequency. We believe this hysteresis to be mainly related to instrument system error. However, the dissipation does *not* show hysteresis because the temperature effect on bandwidth is not obvious. Temperature affects the frequency much more than the dissipation. The rate of increase and decrease in temperature was kept constant at 12°C/hr in this measurement with a special temperature control system (precisely controlled cooling) from Sweden. At this rate the dissipation shows no hysteresis, being a roughly linear variation over the explored temperature range.

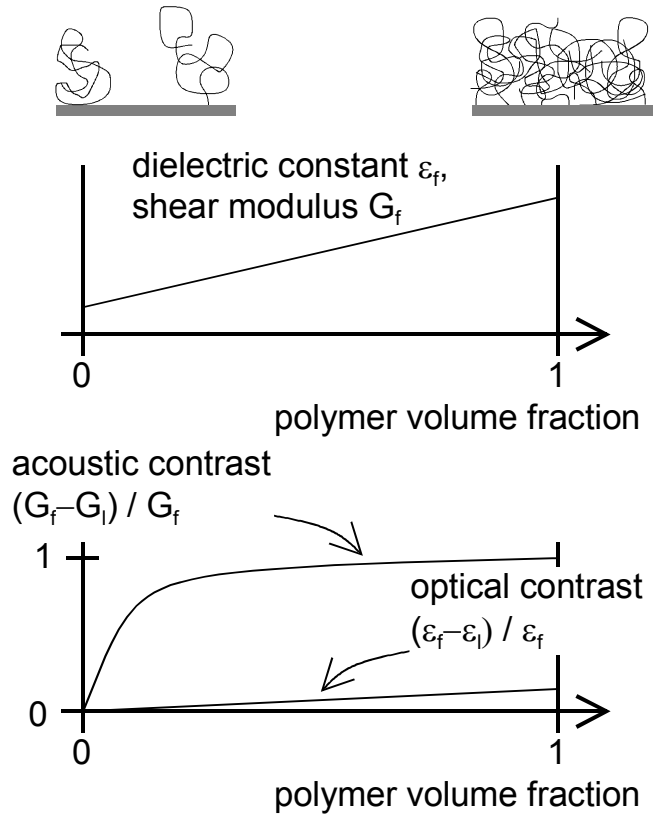

Figure 7.2: Schematic illustration of the qualitative difference between optical and acoustic reflectometry.

When a polymer layer of constant thickness grows in density, its optical contrast is roughly proportional to the polymer volume fraction. The acoustic contrast, on the other hand, saturates to a value of unity.

To minimize the effect of phase separation in the system, the bulk fluid was exchanged with twice the volume of milli-Q water prior to the temperature variation measurements. To

find the effect of the polymer on the complex frequency change, the corresponding temperature variation measurements were subsequently made after the adsorption of the polymer. In order to remove the effect of the hysteresis, all measurements were conducted at the same rate of temperature increase and decrease. The polymer related complex frequency change was then determined by subtracting the calibration (no polymer) result from that obtained in the presence of the polymer. We emphasize that the term "polymer related" in this context can include an increased viscosity of the bulk in addition to polymer adsorption.

7.2 Results

The phase transition temperature of linear pNIPAm was around 32°C as determined by monitoring the desorption of a thick, spin-cast pNIPAm film in water upon lowering the temperature from above the phase transition temperature. (See Fig. 7.3)

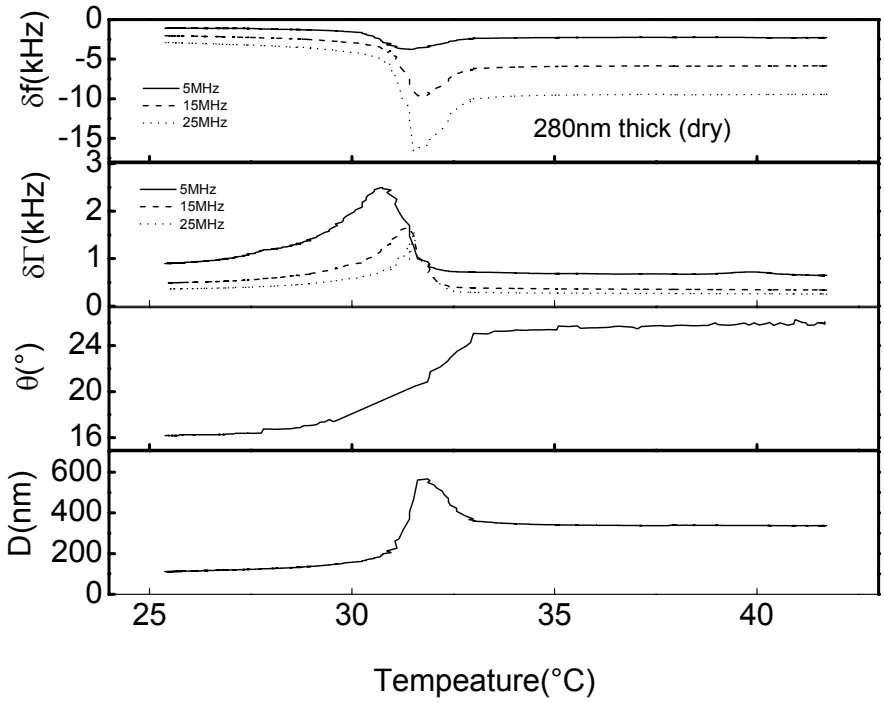

Figure 7.3: Temperature effect of linear pNIPAm film in water monitored by SPR and QCM

7.2.1 Adsorption at 31°C

A hydrophobized gold substrate was kept in contact with milli-Q water at 31°C until both the QCM and SPR signals were stable. A baseline was recorded for both instruments simultaneously, before the introduction of polymer to the system, and the resulting adsorption was monitored. The results of the adsorption are shown in Fig. 7.4, where the changes are plotted in both the resonance frequency (δf) and half-band-half-width (δΓ) from the QCM as well as the SPR coupling angle as a function of time as a direct comparison of the adsorption kinetics. The final frequency shift of –340 Hz at a resonance of 35 MHz corresponds to a Sauerbrey thickness of 12 nm; the shift in coupling angle of 0.4° yields an optical thickness of 4 nm. In the derivation of these numbers a d*n*/d*c* of pNIPAm in water of 0.167 cm^3/g [GW97] and the bulk density of 1 g/cm^3 were assumed. As usual, the acoustic thickness exceeds the optical thickness.

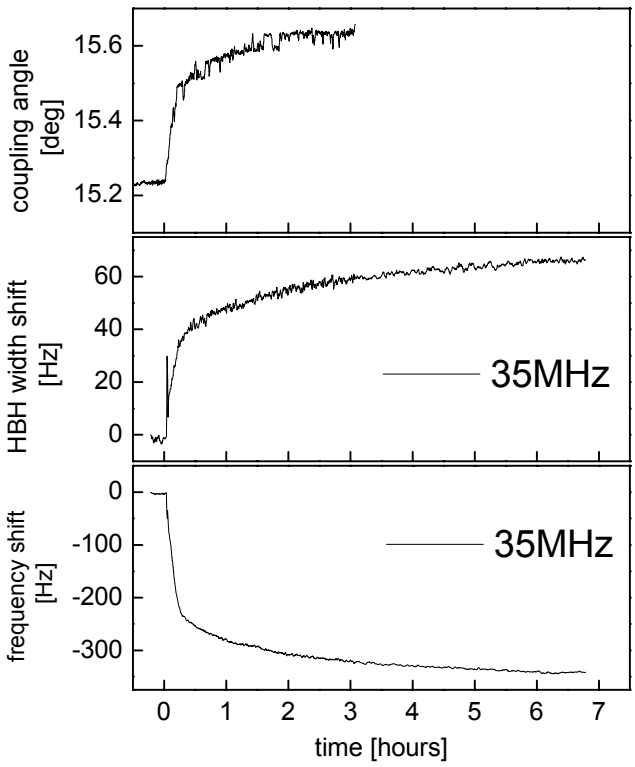

Figure 7.4: Surface plasmon coupling angle, frequency shift, and half-band-half-width as a function of adsorption time (adsorption at temperature 31 °C).

The apparent kinetics as measured by these three different parameters is very similar. In order to remove time as a variable from the adsorption plot it is possible to plot the QCM results as the change in energy loss (δΓ) versus the negative of the measured frequency change (–δ*f*). As a first approximation, this is a good way to investigate the build-up of surface adsorbed layers in terms of conformation and viscoelasticity since it is a plot of the energy loss as a function of the adsorbed mass. This is shown in Fig.7.5a with a straight line included to illustrate the linearity during the initial adsorption. A linear relation is also found in the plot of the surface plasmon coupling angle versus the frequency shift (Fig. 7.5b). The surface plasmon coupling angle by and large reflects the adsorbed amount: It is not affected by trapped water.

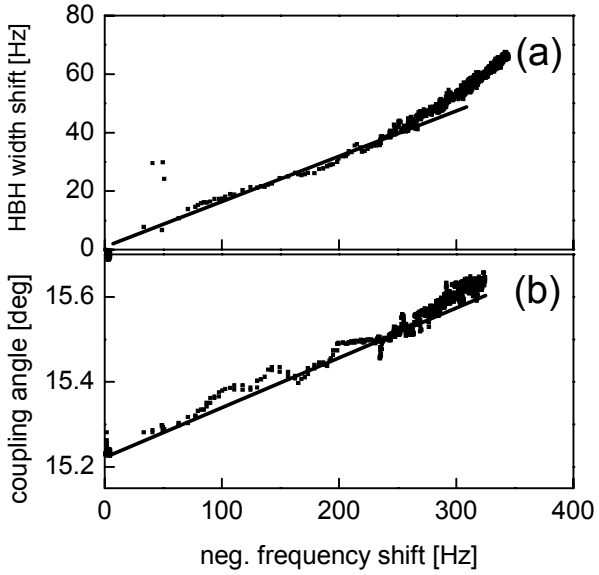

Figure 7.5: a) Half-band-half-width (proportional to the dissipation) and b) SPR coupling angle versus negative frequency shift –δf for the adsorption of pNIPAm onto a hydrophobized gold surface as a function of time. The linear relation observed at low coverage suggests a thickness growth mode. The fifth overtone, i.e. 35 MHz was used in this graph.

7.2.2 Temperature induced conformational changes

Fig. 7.6 shows the raw data for the effect of temperature on the QCM responses of the crystal with and without adsorbed polymer. Panel (a) displays how the frequency response varies over a temperature range of 24 to 36°C. There is a clear hysteretic effect even in absence of polymer which is entirely attributed to instrumental considerations. For each data point during warming up, the instrument first reads the temperature value, then it measures the resonance value (frequency and bandwidth), at this time, the real temperature is a little

higher than the read value, so each data point at a specific temperature during warming up in Fig.7.6 is indeed the measured value at a slightly higher temperature point. Vice versa, for the cooling down process, the data point is measured at a slightly lower temperature than the read temperature value. More complex hysteresis behavior is observed when the polymer is present in solution and adsorbed to the surface and this is the convolution of the instrumental hysteresis and the polymer behavior. An additional complexity to the behavior is introduced by the fact that adsorption and desorption both occur depending on the direction of temperature change. The dissipative behavior (Fig.7.6b) is considerably simpler since there is no obvious instrumental hysteresis in this case because the bandwidth is not sensitive to temperature change. In this measurement, only the fundamental overtone, i.e. 5 MHz was measured.

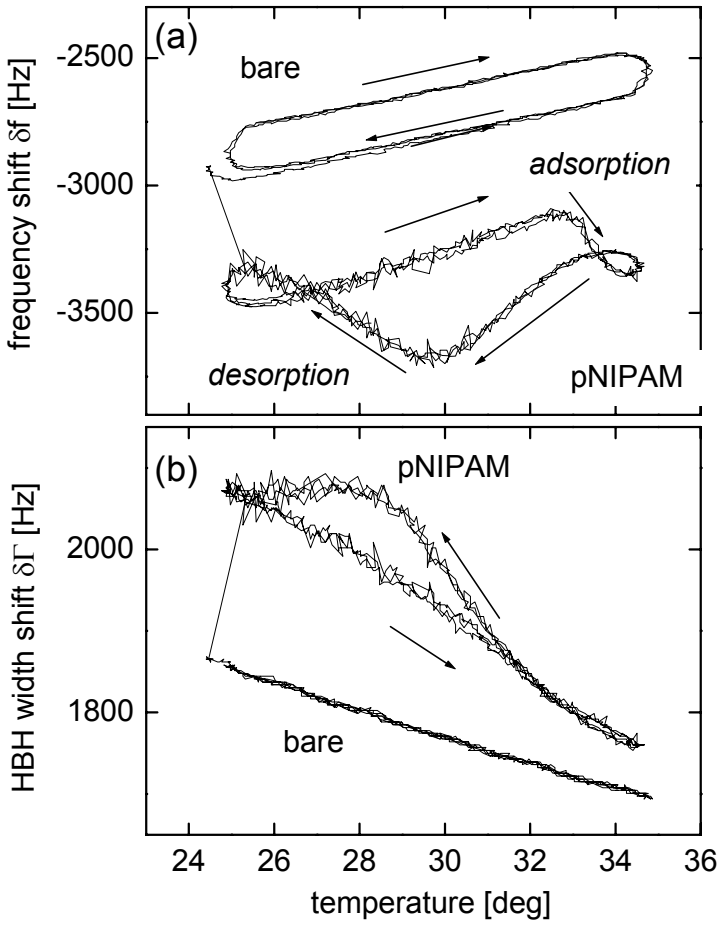

Figure 7.6: a) Frequency shift δf vs. temperature and b) shift of half-band-half-width δΓ vs. temperature for a preadsorbed layer of pNIPAm. A small quartz wafer (14 mm in diameter) and a special temperature controlling system (for controlled cooling down) from Sweden were used in the measurement. The fundamental overtone, 5 MHz was measured.

The instrumental contribution to the frequency and dissipation changes can be accounted for simply by subtracting them from the respective polymer cases and the result of this treatment is shown in Fig. 7.7. A simple averaging technique was employed. (This subtraction does not account for increased viscosity of bulk caused by the presence of the polymer.) It is now much simpler to interpret the behavior.

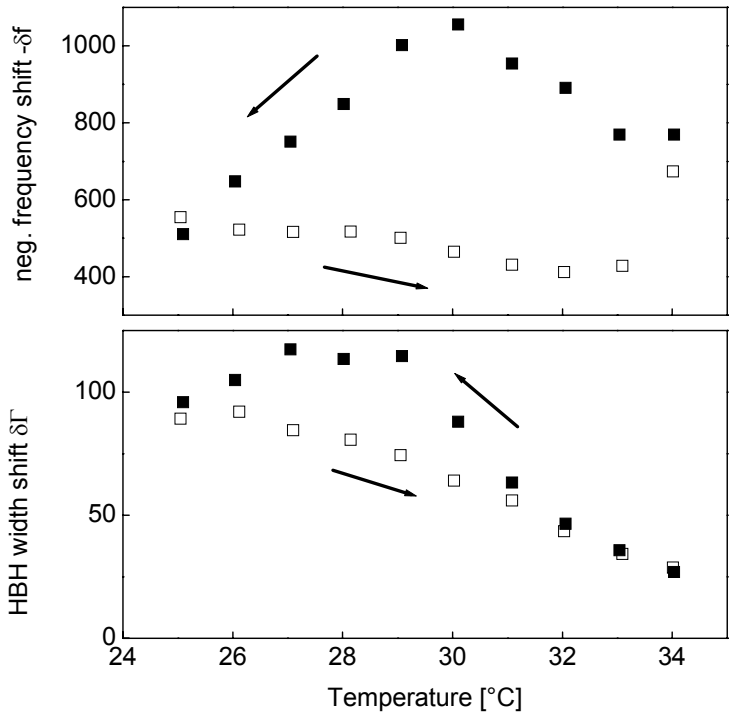

Figure 7.7: Change in a) frequency and b) dissipation associated with the adsorption of pNIPAm as a function of temperature.

Fig. 7.7(a) shows how the frequency shift varies with temperature. As the temperature is raised from 25°C the acoustic thickness ("mass") decreases slowly up to about 32°C (approximately the lower critical solution temperature, LCST) after which it rises steeply. Two competing processes are at work. Below the LCST the adsorbed polymer is gradually collapsing and releasing solvent, whereas at the LCST the dissolved polymer becomes insoluble and deposits onto the surface, leading to a sudden mass increase. (A decreased viscosity of the bulk caused by a collapse of the chains in the bulk would have the opposite effect.) Interestingly the reverse process follows a different path. A *further* increase of acoustic thickness occurs. Most likely, the deposited polymer swells as the solvent quality improves. Adsorption of material from the bulk and a viscosity increasing with decreasing temperature are conceivable explanations, as well. Then, at a temperature (30°C) below the

LCST, there is a decrease in acoustic thickness with decreasing temperature as the excess polymer desorbs, so that finally the layer returns at 25°C to the same state.

This argument is supported by the complementary dissipation data in figure 7.7(b). The dehydration/collapse of the polymer with increasing temperature from 25°C is observed as a steady decrease in the dissipation. Interestingly, the dissipation appears insensitive to the deposition of polymer at 32°C. However, the subsequent swelling of the layer is clearly observed as the temperature decreases and once again is relatively insensitive to the mass change as the polymer desorbs.

7.3 Discussion

The performance of a polymer bearing surface is directly related to the conformation of the adsorbed polymers. For instance, extended polymer cushions are soft and permeable to small molecules, whereas collapsed layers modify the chemical nature of the surface but are mechanically and hydrodynamically inactive. As a general rule, a strong adsorption favors a pancake conformation of collapsed chains, whereas weak adsorption leads to a more extended structure. Given a final thickness of the adsorbed layer of 10 nm as inferred from the frequency shift, one would conclude that pNIPAm is weakly adsorbed and forms a soft, extended polymer cushion. The thickness of the adsorbed layer is comparable to the radius of gyration, R_g, although it is somewhat difficult to put down exact numbers for R_g due to the rather large polydispersity of the material.

The growth mode of such dilute layers is usually thought to be a densification process. [FSS$^+$93] Initially the coverage is low. The adsorbed molecules have few attachment sites and remain Gaussian coils with little disturbance of their structure by the interface. As more and more chains adsorb, the interface gets crowded but the thickness of the film remains about constant and equal to the diameter of the chains. This growth mode is different from the layer-by-layer thickness growth mode, where the first chains adopt a flat conformation and subsequent chains then deposit as pancakes on top of these chains.

Interestingly, our data indicate a *thickness growth mode*, rather than a densification process. This interpretation is based on two findings: the fact that optical and acoustic thicknesses go parallel and the fact that frequency shift and dissipation are largely parallel as well. We first argue why an acoustic thickness proportional to the optical thickness is not expected for the densification mode. Acoustic thickness and optical thickness differ in their

contrast function, which are $(G_f - G_a) / G_f$ for the acoustic thickness and $(\varepsilon_f - \varepsilon_a) / \varepsilon_f$ for the optical thickness. The dielectric constant typically varies by a few percent, while the shear modulus may vary by orders of magnitude if polymer strands are added to a liquid. As a consequence, the contrast function in optics is by and large proportional to the density, whereas the term $(G_f - G_a) / G_f$ comes close to unity for moderate polymer concentrations and does not increase much upon further increase of the polymer volume fraction (Fig.7.3). The acoustic contrast saturates. Were the film to grow via densification, one would expect the acoustic thickness to increase rapidly in the early phases of adsorption and remain constant later on, as part of the trapped water is replaced by polymer chains. This is not the case.

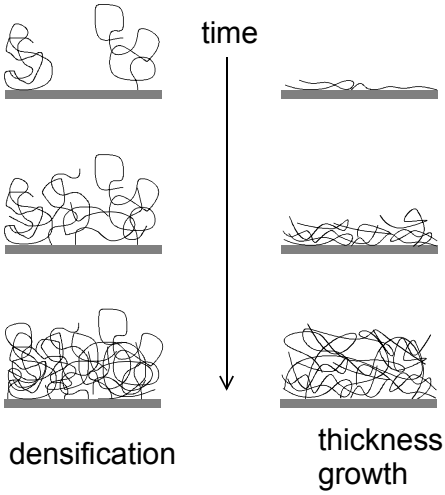

Figure 7.8: Schematic description of the limiting cases of the densification growth mode and the thickness gradual growth mode.

The comparison of frequency shift and shift in half-band-half-width leads to the same conclusion. Frequency and bandwidth are proportional to each other for the first hour of adsorption. This suggests that the viscoelastic properties of the film remain unchanged during the film growth. Strictly speaking, this statement only applies to the combination of parameters Im $((G_f - G_a)/G_f)$ / Re $((G_f - G_a)/G_f)$. However, it is quite unexpected that the viscoelasticity should change in such a way that this ratio remains constant.

There is some deviation from linearity in the final stages of adsorption. While one might attribute these changes to variations in the viscoelasticity of the material (caused by densification), this is not necessarily the case. Eqn. 2.3.6 was calculated for the long-wavelength-limit, that is, for layers much thinner than the wavelength of sound. The penetration depth of shear sound in water at $f = 35$ MHz is 60 nm, which is larger but not

much larger than the final film thickness of 10 nm. For films which are thinner but not much thinner than the wavelength of sound, there is a perturbation calculation giving higher order corrections to $\delta f^* / f$ in areal mass density m_f. This calculation predicts

$$\frac{\delta f^*}{f} \approx -\frac{m_f}{m_q}\left[1-\left(\frac{Z_q^2}{Z_f^2}-1\right)\frac{Z_a^2}{Z_q^2}\right]+\left(\frac{m_f}{m_q}\right)^2\left[1-\left(\frac{Z_q^2}{Z_f^2}-1\right) i\sqrt{2}n\pi\,\frac{Z_a}{Z_q}\right] \qquad (7.1)$$

For the real part of $\delta f^*/f$ the second order term in eqn. 7.1 can safely be ignored. For the imaginary part, however, this is not the case. The ratio $2^{1/2}\, n\, \pi\, m_f / m_q / (Z_a/Z_q)$ quantifying the relative importance of the second order term is about 10%. The curvature seen at high coverage in Fig. 7.4(a) may either be attributed to a change of the viscoelastic properties of the layer or to a violation of the long-wavelength approximation and the corresponding second order correction. However, closer inspection of Fig. 7.4a shows that the data do not lie on a parabola. Rather, there is a kink at $\delta f \sim -250$ Hz, which would give support to the idea that the viscoelastic properties of the layer change for high adsorbed amounts.

A layer build-up via thickness growth seems counterintuitive because it is not clear why a layer-by-layer growth should stop at a film thickness equal to the diameter of the unperturbed chain. We argue that this peculiar growth mode is caused by the fact that the adsorption is done close to the lower critical solution temperature, where phase separation into a polymer-rich and a solvent-rich phase is imminent. We interpret our findings as a wetting phenomenon. The hydrophobic gold surface favors the polymer-rich phase and induces the formation of layer of this phase at its surface. Initially, the layer is rather flat. This pancake conformation is not primarily caused by a multitude of attachment sites; it is the consequence of the fact that there is phase boundary at the film–liquid interface. When the wetting layer grows in thickness, there is rearrangement of chain conformations, such that the chains arriving later also find points of attachment to the substrate. The rearrangement occurs under conditions of constant intramolecular interaction – the shape of the coils alters without an observable change in their viscoelastic properties. These rearrangements take time, making the adsorption a slow process. The growth of the wetting layer is arrested when the chains on top of the layer can no longer reach the substrate. At this point, there is a slight decrease in density, leading to the upward curvature in the $\delta\Gamma$–δf plot and in the plot of optical versus acoustic thickness. The film does not grow to infinite thickness because we have a situation of *partial* wetting. Partial wetting often is the result if a delicate balance, in this case the temperature being just below the phase transition temperature.

In order to better understand the variation of the viscoelastic properties of the adsorbed film with temperature, we have plotted the dissipation normalized by the effective mass. Thus we probe directly the change in viscoelastic properties. This is shown in Fig.7.9 for both the increasing (upper curve) and decreasing (lower curve) temperature traces. Not unexpectedly, there is a hysteresis between the two curves. We believe that this is due to the dynamics of the re-conformation of the polymer layer being slower than the rate at which the temperature is changed.

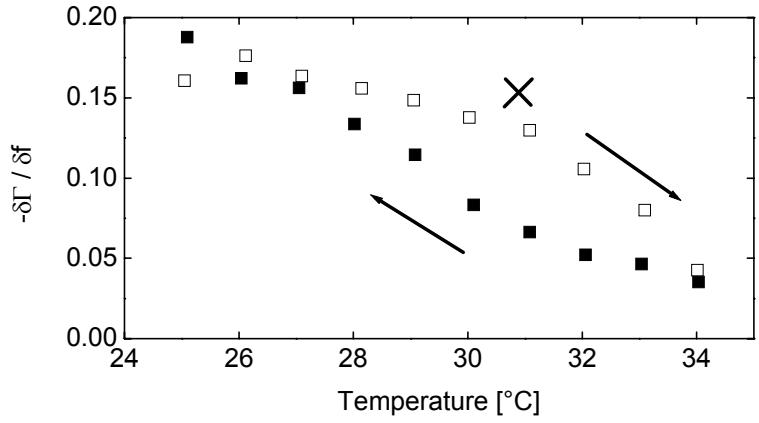

Figure 7.9: Change in dissipation normalized by the negative change in frequency as a function of temperature.

We note that each point can be interpreted as the gradient of a δΓ–δf plot such as in Fig. 7.5a. In that figure the adsorption was performed at constant temperature and the gradient (*dn/dc = 0.167cm³/g*) should therefore represent the equilibrium value for the ratio at that temperature. This point appears as a cross on Fig. 7.9 and lies above both curves, suggesting that the layers have undergone some irreversible densification during the cycling process.

7.4 Conclusions

From the combined analysis of the in-situ QCM and SPR measurements we conclude that the adsorption of the pNIPAm occurs by an increase in the thickness of the adsorbed polymer layer. Only in the final stages of the adsorption does there seem to be some deviation from this adsorption mecanism. The results indicate a consistent rigidity and solvent content over the majority of the adsorption, only slowly decreasing in rigidity in the final stages (final 30%) of the adsorption process.

The QCM technique is sensitive to any mass oscillating with the crystal, which includes hydrodynamically coupled solvent. This is in contrast to the SPR technique which is dependent on the difference in refractive indexes and is thus not sensitive to solvent contributions. It is thus a considerable advantage to run these techniques in-situ to gain a better understanding of the entire adsorption process, as seen in these measurements. Contrast between different adsorption processes can thus be observed by measuring with the full range of techniques.

The effect on the polymer conformation, of changing the temperature, could also be investigated with the QCM. This novel experiment demonstrates the possibility of running the QCM experiments as a function of temperature by removing inherent temperature dependent crystal responses. It was possible to determine separately the processes of adsorption/desorption, in addition to swelling/de-swelling phenomena for the pNIPAm system.

8 Temperature effect of photo cross linked PNIPAM films in water monitored by SPR and QCM[9]

Temperature-sensitive polymer gels have been proposed as "smart materials" in a number of different contexts. [JG02] On the one hand, they can form soft actuators, valves, levers. In a reverse mode, the volume change related to the collapse can turn the gel layers into transducers for sensing applications. In many cases, the transition temperature can be shifted by pH, ion concentration, or other additives. At fixed temperatures, the transition can in this way be driven by a wide range of parameters. Because the collapse is easily detected with high accuracy, the gel layer forms a transducer, which can be matched to the target of sensing by means of polymer synthesis.

Poly-n-isopropyl-acryl amide (pNIPAm), in particular, has been investigated in much detail. [Sch92] pNIPAm has a reversible lower critical solution temperature (LCST) in water at about 31°C. Since this temperature is between room temperature and body temperature, biological applications are envisioned. The temperature-induced collapse is a consequence of an entropy gain following the dehydration of the amide moieties. The transition temperature can be affected by the addition of salt, alcohol, or surfactants, and by the variation of the solution pH. [Gra00] In the bulk, aqueous solutions of pNIPAm phase separate at $T > T_{LCST}$ into a polymer-rich and a polymer-arm phase. For cross-linked gels, the LCST results in shrinkage in size. [AKR00] [KVW02] Kuckling et al. have reported on the synthesis and possible applications of photo-cross-linked pNIPAm gels. [HKF03] [HKF02] Here the transition behavior of films made from these materials was measured by a combined optical and acoustic approach. A quartz crystal microbalance (QCM) [HRB+98] [LMJ00] and a

[9] Partly adapted from Zhehui Wang, Dirk Kuckling, Diethelm Johannsmann Temperature effect of pNIPAM Film on gold surfaces measured in situ by QCM and SPR Soft Materials 1, **(2003)** 353.

surface plasmon resonance (SPR) spectrometer [Kno97] were used in parallel on the same sample.

8.1 Materials and Sample Preparation

Details of the synthesis of the gels are provided elsewhere. Photo-cross-linkable copolymers of *N*-isopropylacrylamide (NIPAm) and 2(dimethylmaleimido)-*N*-ethylacryl-amide (DMIAm) as the cross-linker, were prepared by free radical polymerization, and provided by Dr. Kuckling. [KHF02] Aqueous solutions of the copolymers showed lower critical solution temperature (LCST) behavior. The corresponding phase transition temperature was detected by differential scanning calorimetry. The resulting polymers were shown to be photo-cross-linkable via a [2+2]-cyclo-addition (Fig. 8.1). With 2 wt% thioxanthone as the photo sensitizer, nearly full conversion was achieved.

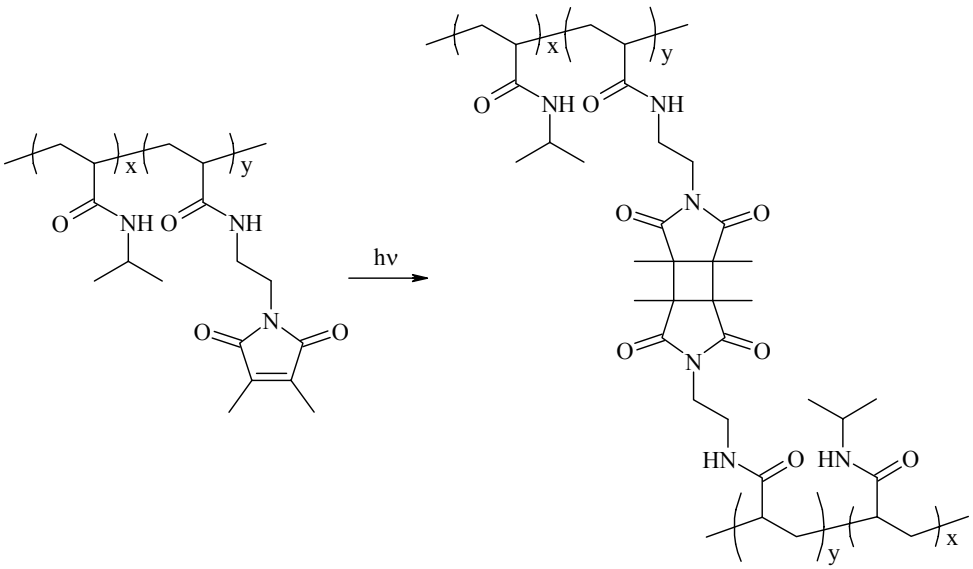

Figure 8.1: Photo-cross-linking reaction of pNIPAm.

The films were prepared in the following way: The comonomers (with crosslinker-content 2, 5, and 7.2 wt %) was dissolved in cyclohexanone at a concentration of 5 wt%. Thiooxanthone was added to the solution in a concentration of 2 wt % (of polymers) for

photo-sensitization. The solution was kept in refrigerator for at least one day before use. The films were spin-cast onto the quartz wafers at room temperature. The speed of rotation was 250 rpm for the first 30 s and was increased to 3000 rpm for another 3 minutes. Then the films were vacuum dried at room temperature for one hour to avoid separation of crosslinker and photosensitizer from the film. Crosslinking was achieved by irradiation with UV-light (75 W for one hour) after vacuum drying. The film thickness got in this way was about 250nm. Using 1.25-wt. % of comonomer in cyclohexanone for spin coating, we got a film thickness around 50nm.

8.2 Data Analysis

8.2.1 Surface Plasmon Resonance Spectroscopy

For prism coupling, SPR data are usually modeled with Fresnel formalism. Such formalism cannot be straightforwardly applied to grating coupling because the grating is not a planar surface. The Pockrand-approximation, [Poc78] on the other hand, is inapplicable because it is based on a perturbation analysis with the film thickness as the small parameter, whereas the films investigated here are comparable in thickness to the decay depth of the surface plasmon. We use a mixed approach, where we apply the Fresnel equations to a hypothetical planar gold surface covered by the polymer film and derive a *shift* in coupling angle induced by the film. In a second step, we assume that the shift in coupling angle on the surface with a corrugation grating is the same as on the planar surface.

Because the refractive index of the film decreases with increasing swelling, there is a net decrease of the coupling angle with swelling. The penetration depth of the optical wave is about 150 nm.

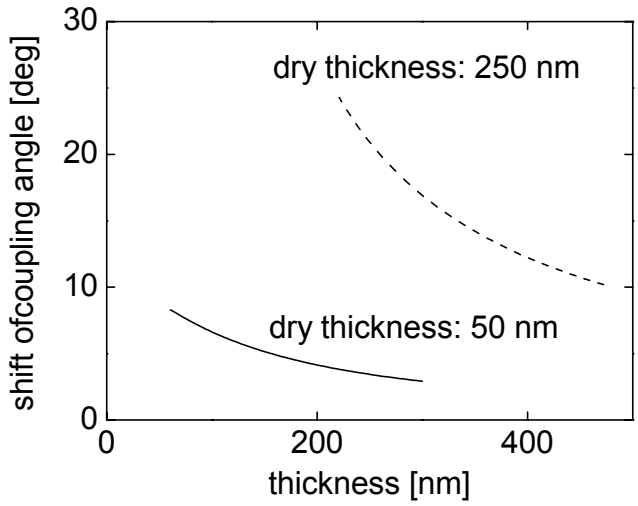

Figure 8.2: Model calculations of the shift of the coupling with swelling of a film.

Fig. 8.2 shows the outcome of the calculations for two different dry thicknesses, which are 50 and 250 nm. It was assumed that the refractive index inside the film is $n_f = n_{water} + (n_{dry} - n_{water})\, t_{dry}/t_f$, where n_f is the thickness of the swollen film, $n_{dry} = 1.48$ is the refractive index of the dry film, [GW97] $n_{water} = 1.334$ is the refractive index of the water, t_{dry} is the dry thickness of the film as determined with the QCM, and t_f is the film thickness in the swollen state. The calculation shows that the coupling angle *decreases* with increasing film thickness in both cases. While this result may seem counterintuitive at first sight, it is a consequence of the fact that the decay depth of the surface plasmon (~ 150 nm) is comparable to the film thickness or even smaller. The expansion of the film upon lowering the temperature is accompanied by a decrease in refractive index. This decrease in refractive index outweighs the effect of the thickness increase. Note that the opposite is true for very thin swollen films: the effect of increasing thickness – tending to increase the coupling angle – slightly overcompensates the effect of decreasing refractive index and, as a consequence, the coupling angle slightly increases upon swelling for very thin films.

8.2.2 Quartz Crystal Microbalance

In principle, we can predict the frequency shift and the shift in bandwidth induced by planar films in water. The equations are in analog to the Fresnel formalism in optics. However, there is the usual inversion problem: the film properties can only be derived from the experimental shifts in frequency and bandwidth if the film thickness is much less than the wavelength of shear sound (~1 μm in water). The films investigated here are not thin in this sense and we do not provide quantitative analysis. The general phenomenology, nevertheless, is rather clear.

For the 250 nm samples, the film thickness is comparable to the wavelength of shear sound, as evidenced by the occurrence of a "film resonance" in Fig. 8.3. [GM94] [JMW$^+$92] A film resonance occurs when the film thickness is equal to $\lambda/4$ with λ the wavelength of shear sound. The film resonance is caused by destructive interference between the waves reflected at the quartz–film interface and at the film–liquid interface. Around the film resonance the dissipation goes through a maximum, whereas the frequency shift displays an antisymmetric pattern. Since the wavelength of sound scales as the inverse overtone order, the film resonance occurs at different temperatures (that is, different film thicknesses) on the different harmonics. A film resonance is clearly visible for 250 nm thick sample with crosslink density of 2% (Figs. 8.3 and 8.5): Upon lowering the temperature, the frequency first decreases, indicative of an increase in thickness. However, below the transition temperature the reverse trend is found: the frequency increases, even though the film thickness presumably continues to increase. Such a situation only occurs for conditions where the film is thicker than the wavelength of sound.

The occurrence of the film resonance proves that the acoustic wave does indeed reach the top of the film – at least in the collapsed state. If the wave was confined to an evanescent tail within the film (as in the case of the surface plasmon) frequency and bandwidth would

only depend on the viscosity inside the film. For the set of thin films (Fig. 8.4), the QCM data can even be interpreted within the Sauerbrey picture: the frequency decreases with increasing thickness. [Sau64]

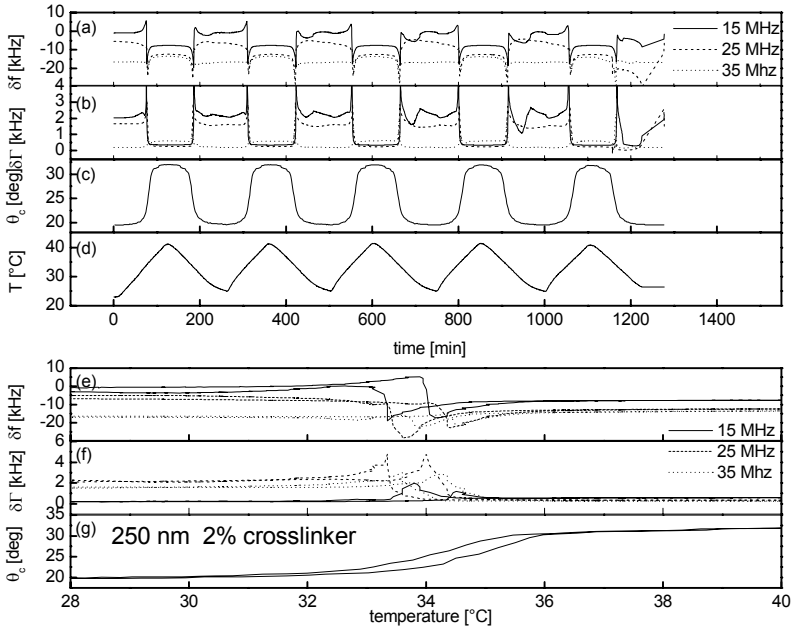

Figure 8.3: (a) Frequency shift, (b) shift of half-band-half-width, (c) SPR coupling angle, and (d) temperature as a function of time. The transition is reversible with good reproducibility. The temperature-dependent data (panels e–f) are only shown for the second cycle for clarity. The sample had a dry thickness of 250 nm, the content of cross linker was 2%.

8.3 Results and Discussion

Fig. 8.3 shows the results of a typical measurement versus time. In this case the dry film thickness was 250 nm, the fraction of crosslinker was 2%. The temperature was ramped between 28 °C and 42 °C at a rate of about 0.2 °C/ min. Panel (d) displays the temperature in the cell. As panels (a) – (c) show, the evolution of frequency, bandwidth, and SPR coupling angle is largely reversible. Panels (e) – (g) show the same data as panels (a) – (c) versus temperature. Only the second cycle is shown for clarity. Figures 8.4 and 8.5 also show the

second cycle of a measurement with many cycles. The first cycle in some cases was a little different from the following ones.

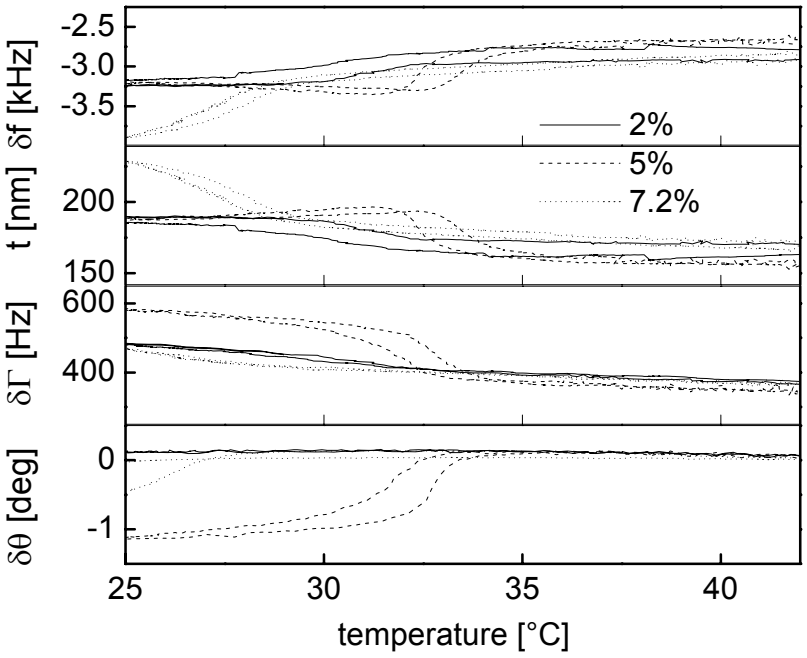

Figure 8.4: Temperature dependence of (a) frequency shift, (b) Sauerbrey thickness, (c) bandwidth and (d) coupling angle for three "thin" samples. The cross linker content is indicated in the figure. The dry thicknesses as determined from QCM data on the dry films were 50nm, 70 nm, and 50 nm for a crosslinker content of 2%, 5%, and 7.2%, respectively.

Fig. 8.4 shows the transition behavior of films with a dry thickness of about 50 nm. The SPR coupling angle shows that there is a transition for cross-linker content of 5 and 7.2%. For the 2% sample the transition is not detected. We always find that the coupling angle increases at the transition temperature. This finding may appear counterintuitive, because the film collapses, that is, decreases in thickness at the transition. Note, however, that the collapse is accompanied by an increase in refractive index. In this case, the increase in refractive index outweighs the effect of the thickness change because the film is thicker than the decay length of the surface plasmon.

The QCM data in all cases give evidence of a swelling transition. Both the QCM data and SPR data suggest that the amplitude of the transition is by no means dramatic. The shift in SPR coupling angle is in the range of 1degree. Using the model calculation displayed in Fig.8.2 (bottom curve) this suggests that swelling ratio is less than 1.5. This estimate is confirmed by the QCM data. For thin films, the bandwidth does not go through a maximum, that is, there is no film resonance. In the absence of the film resonance one can define an "equivalent acoustic thickness" t_{ac} via the relation

$$\frac{\delta f}{f} = -\frac{\delta m}{m_q} = -t_{ac}\frac{2f_0\rho_f}{Z_q}$$

where δf is the frequency shift, f is the frequency, δm is the areal mass density of the film, $m_q = Z_q/(2f_0)$ is the areal mass density of the quartz wafer, f_0 is the frequency of the fundamental, ρ_f is the density of the film, and $Z_q = 8.8 \times 10^6$ kg m^{-2} s^{-1} is the acoustic impedance of AT-cut quartz. Again, t_{ac} is not a true thickness in the geometric sense, it is an approximation based on the outcome of the QCM-measurement. This acoustic thickness as function of temperature is shown in Fig. 8.4b. In the collapsed state, the gel layers are still swollen to a thickness of about 150 nm, that is, the polymer volume fraction is about 0.3. This statement holds independent of the crosslink density. In the swollen state at low temperatures, the thickness increases to a value between 180 and 250 nm, consistent with the SPR data.

Fig. 8.5 shows the same data for the thick samples. In this case we have not converted the data to a Sauerbrey thickness because of the presence of the film resonance. As expected, the transition is strongest for the lowest cross-linker content of 2%.

There is no clear correlation between the transition temperatures and the amplitude of the transition as a function of cross-linker content. Possibly, the process of crosslinking is perturbed by the presence of the gold substrate. Kuckling and co-authors have also found that the swelling behavior of thin films differs from the swelling of thick samples. These authors

find a cross-over thickness between “thin” and “thick” samples at a thickness range between 280 and 500 nm.

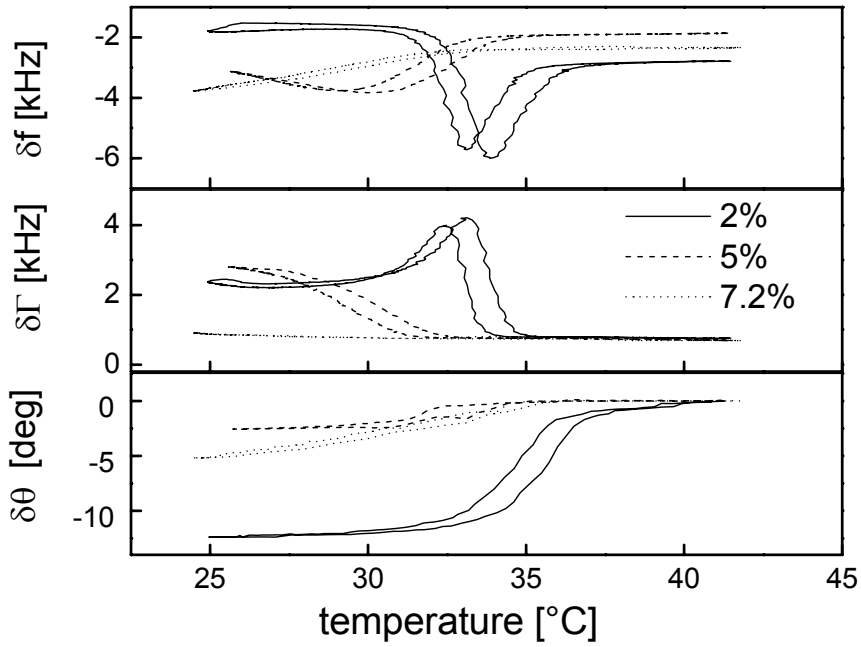

Figure 8.5: Temperature dependence of frequency shift (a), bandwidth (b), and coupling angle (c) for three “thick” samples. The cross linker content is indicated in the figure. The dry thicknesses as determined with the QCM were 250nm, 270 nm, and 250nm for a cross linker content of 2%, 5%, and 7.2%, respectively.

With regard to application as transducers for sensing, a balance has to be found between sensitivity on the one hand, and stability, reproducibility, and a straightforward interpretation, on the other. Both the crosslink density and the film thickness can be adjusted in order to achieve an optimum balance. Both a large film thickness and a low crosslink density are beneficial for sensitivity. By far the strongest effects are found for the 250 nm film with a cross-linker content of 2%. The frequency shifts more than 20 kHz over a temperature range of less than 1 °C, the coupling angle varies by more than 10 deg, over a temperature range of

about 2 °C. Given the instrumental resolution of about 1 Hz (QCM) and 10^{-3} deg (SPR) this translates to very good overall sensitivity. As Fig.8.3 shows, the strong effect in the frequency is caused by a film resonance. When a dry quartz plate is coated with a soft layer of thickness $\lambda/4$ (λ the wavelength of shear sound) the frequency shift induced by an adsorbed film is resonantly enhanced. In Fig. 8.3 we see the same kind of resonant enhancement for a wet film. The presence of the film resonance induces complications with regard to the interpretation. Firstly, there is an interplay between the effects of thickness and effects of viscosity, and secondly, the frequency shifts as a function of temperature in a non-monotonous way. On the other hand, the instruments provide several independent parameters and therefore a large amount of redundancy: Firstly, one has frequency and bandwidth on three different harmonics available for analysis, and secondly, the SPR coupling angle *does* shift in monotonous way. If a single frequency was the only measured quantity, the film resonance should certainly be avoided in the context of sensing. With the added information from the bandwidth, the overtones, and the SPR coupling angle the resonant enhancement of sensitivity caused by the film resonance can be exploited without sacrificing reliability.

As the data show, the strength of the film resonance can be adjusted by the cross-link density. At a cross-link density of 5%, the film resonance is still present, but much less pronounced. The shift in coupling angle is 1.5 deg over a range of 2 °C, which is still more than enough. Both the shift in frequency and the shift in bandwidth are less steep. In comparison to the sample with 2% crosslinker content, this implies a decrease in sensitivity, on the one hand, but an increased reliability, on the other.

8.4 Conclusions

Spin-cast films of cross-linked pNIPAm have been prepared and investigated with respect to their use as transducers for sensing. The swelling transition (which can be induced by parameters other than temperature, as well) was probed by combination of an acoustic and optical technique, namely the quartz crystal microbalance (QCM) and surface plasmon resonance (SPR) spectroscopy. This combination provides a number of different parameters, which – in conjunction – allow for the use of layer thickness for sensing applications. The SPR coupling angle is mostly sensitive to the refractive index of the film material. The frequency shift and the bandwidth, on the other hand, strongly depend on the film thickness. For certain particularly interesting cases, there is an intermediate situation where the film thickness equals a quarter of the wavelength of sound, inducing a film resonance. Around this condition, the sensitivity of the QCM is resonantly enhanced. While certain complications result in terms of data analysis, the instruments redundancy aids in unambiguous interpretation. The sharpness of the film resonance can be adjusted by the cross-linker content. For higher cross-link density the film resonance is less pronounced, which decreases the sensitivity of pNIPAm film as a sensing material but, on the other hand, increases its reproducibility and reliability.

9 In Situ Investigation of the Electropolymerization and Doping / Dedoping of Poly(pyrrole)

An in situ combination of surface plasmon resonance (SPR) spectroscopy and quartz crystal microbalance (QCM) is used to study the electropolymerization and the doping/dedoping behavior of thin poly(pyrrole) films in aqueous solutions. A mixed anion and cation exchange behavior is observed. The mass determined by QCM continuously increases during redox cycling. The combined QCM/SPR measurements reveal that this is caused by a relatively slow process occurring when polypyrrol is in the oxidized (polaronic) state. This behavior is interpreted as an accumulation of neutral salt and solvent in the film.

9.1 Introduction[10]

Conducting polymers are promising candidates for a variety of applications such as antistatic coatings, sensor layers, or matrixes for catalyst particles.[RJ97][IPS$^+$00] Many of these applications make use of the fact that the electric conductivity of the polymer can be controlled by its redox state. Polypyrrole is insulating or semi conducting in the reduced state and a metallic conductor ("synthetic metal") in the oxidized form. Upon oxidation, positive charges in the polymer chains are generated, which are compensated by the incorporation of anions (doping process). [Li97][GGP01] Given their complex behavior, it is desirable to have as much information available on these films as possible. Because there is considerable variability between different samples (for instance, induced by surface roughness), one wishes to combine complementary techniques in situ on the same sample. The combination of the quartz crystal microbalance (QCM) and surface plasmon resonance (SPR) spectroscopy provides such an approach. [LMJ00] Furthermore, it has been shown by SPR imaging that conducting polymer layers with thicknesses in nanometer range can be used as DNA sensors [GLM$^+$00] or as a matrix for the electro catalysis of redox enzymes.[RKB$^+$02] When applied as thickness monitors, QCM and SPR yield an "acoustic thickness" and an "optical thickness", respectively. Here, we apply this concept to the doping/dedoping characteristics of conducting polymers. The electropolymerization of pyrrole was studied by tracking the

[10] Text partly adapted from: Bund, A.; Baba, A.; Berg, S.; Johannsmann, D.; Luebben, J.; Wang, Z.; Knoll, W. Combining Surface Plasmon Resonance and Quartz Crystal Microbalance for the in Situ Investigation of the Electropolymerization and Doping/Dedoping of Polypyrrole *J. Phys. Chem. B.;* 107 (2003) 6743.

frequency shift of a QCM and the reflectivity in SPR at the same time. [BKK+02] Here, we extend the investigation to the doping/dedoping behavior of thin polypyrrole films (5-10 nm).

Electropolymerization reaction of pyrrole can be separated into the following steps: [Li97]

$$\text{H-N-H} \rightarrow (\text{H-N-H})_{ad}$$
$$(\text{H-N-H})_{ad} + A^- - e \rightarrow A^-(\text{H-N-H})^+_{ad}\bullet$$
$$2\,A^-(\text{H-N-H})^+_{ad}\bullet \rightarrow \text{H-N-N-H} + 2A^- + 2H^+$$
$$\text{H-N-N-H} + A^- - e \rightarrow A^-(\text{H-N-N-H})^+_{ad}\bullet$$
$$A^-(\text{H-N-N-H})^+_{ad}\bullet + A^-(\text{H-N-H})^+_{ad}\bullet \rightarrow \text{H-N-N-N-H} + 2A^- + 2H^+$$
$$\text{H-N-N-N-H} + A^- - e \rightarrow (\text{H-N-N-N-H})^+ A^-$$

.....

where H-N-H represents the pyrrole molecule with two α-H; A^- represents solution anion; $A^-(\text{H-N-H})^+_{ad}\bullet$ means some complex of solution anion and pyrrole cation radical; $(\text{H-N-N-N-H})^+ A^-$ represents the doped polypyrrole where the positive charge is delocalized on the conjugated polypyrrole chain and the anion is doped beside the chain.

In electrochemical experiments, the areal mass density m_f can be calculated from $m_f = \rho_f d_{ac,f}$ and related to the transferred charge density Q.[BS02] In the case of electropolymerization of pyrrole, the theoretical value of the ratio m_f/Q can be calculated from eqn. 9.1.

$$\frac{m_f}{Q} = \frac{(M_M - 2M_H) + x_A M_A + x_S M_S + x_N M_N}{(2 + x_A)F} \qquad (9.1)$$

where M_M, M_A, M_H, M_S, and M_N are the molar masses of monomer, incorporated anion, hydrogen, solvent, and neutral salt, respectively, x_A, x_S, and x_N are the molar equivalents of doping anions, solvent, and neutral salt per monomer, and F is the Faraday constant (96 485 C mol^{-1}). The product of m_f/Q and the Faraday constant represents the mass change associated with the exchange of one mole of electrons and is sometimes called the apparent molar mass M_{app} involved in an electrochemical reaction.

In the case of polypyrrol, transfer of solvent and coions has been clearly verified.[GGP01] Reviewing the actual literature, one learns that $x_A \approx 0.3$ seems to be a reasonable value.[HIS02][EWS01] The parameters x_S and x_N strongly depend on the preparation conditions.[ZPG+02] If side reactions (reactions that consume charge but do not change the mass on the quartz surface, such as formation of soluble oligomers or cross-linking of the

polymer chains) occur, the experimentally observed ratios m_f/Q will be lower than the theoretical values.

9.2 Experimental

The SPR measurements for the synthesis and the doping/ dedoping process of the polymer layers were performed at a fixed angle, which was chosen prior to the experiment according to the whole SPR spectra scans of the original Au electrode or the polypyrrol film (Figure 9.1).

To separate the rf voltage (network analyzer) and the dc voltage (potentiostat), a combination of a capacitance and an inductance was used as described in ref [BS00]. An EG&G 263A potentiostat (Princeton Applied Research) controlled by the CorrWare Software (Scribner Associates, North Carolina) was used for the electrochemical experiments. One gold electrode of the quartz crystal (electrochemically active area 1.4 cm^2) served as the working electrode in a three electrode arrangement. The counter electrode was a Pt foil (purity 99.99%, Good Fellow, Cambridge, England). All potentials were measured versus commercial reference electrodes: either a saturated calomel electrode, SCE, (Meinsberg Sensortechnik, Meinsberg, Germany) or an Ag/AgCl electrode (BAS scientific, Congleton, U.K.).

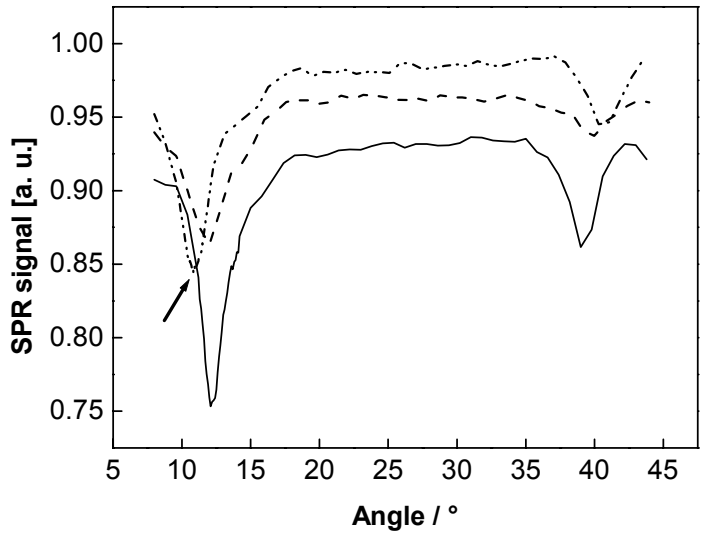

Figure 9.1: SPR spectra of the original quartz without film (solid line) and with a thin polypyrrol film in the reduced (---) and oxidized state (— · · —). The arrow indicates the fixed angle for the dynamic SPR measurements.

In the text, potentials are quoted with respect to the reference electrode by taking into consideration the potential difference of 40 mV. All solutions were prepared from analytical grade chemicals and ultra pure water (Milli-Q). The measuring PTFE cell was home built. Because of the limited space in the cell and in order not to block the optical path, inert gas purging was not applied.

9.3 Results

9.3.1 Synthesis of Thin polypyrrol Films

The electropolymerization of pyrrole was initiated by stepping the potential to +0.5 V (SCE) after 30 s at the open circuit potential (OCP). The current transient (Figure 9.2) shows the typical large peak due to double layer charging. Afterward the current density remains at $i \approx 7.5\ \mu A/cm^2$ and slowly increases after about 200 s. The cell was switched back to OCP after 332 s, at which i reached a value of 16 $\mu A/cm^2$. (Figure 9.2, arrow) At that point, QCM signal indicated that a polymer layer with an areal mass density of approximately 1 $\mu g/cm^2$ had been deposited, which corresponds to a layer thickness of 6.7 nm, assuming a polymer density of 1.5 g/cm^3. [SKH99] Because the imaginary part of δf^*(eq 2.3.5) was only 50 Hz (measured at fifth harmonic), the Sauerbrey equation could be used to relate frequency shifts to mass changes.

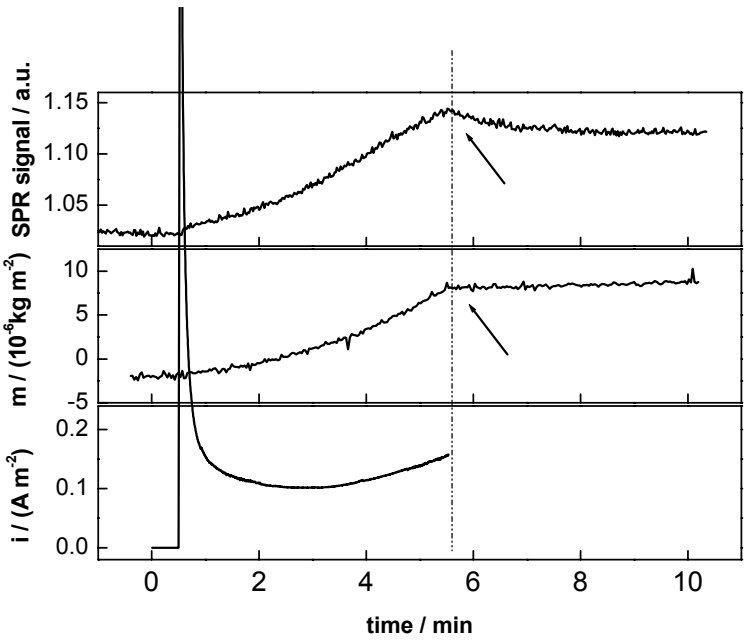

Figure 9.2: Current transient of polypyrrol deposition from 0.1 M pyrrole, 0.1 M KCl, and accompanying changes of mass and reflectivity (10.5°) for potential step from OCP to 0.5 V (SCE) and back to OCP (arrow).

The electropolymerization was stopped at this relatively small thickness because the film absorbs light at λ=633 nm and the plasmon becomes shallow. During the deposition, the reflectivity increased. Because the measurement was carried out at an angle below the angle of minimum reflectivity, an increase of the reflectivity indicates an increase of the coupling angle and hence an increase of optical thickness. The increase of reflectivity should be proportional to the increase of the thickness, provided that the dielectric constant of polypyrrol is constant during electropolymerization.

After the current had been switched off, the frequency shift of the QCM immediately leveled off, whereas the reflectivity slowly decreased (Figure 9.2). Table 9.1 summarizes the resulting values of m_f, Q, m_f/Q, and $x_S M_S + x_N M_N$ (eq 9.4) for two different polypyrrol films, prepared under similar conditions.

TABLE 9.1: Results of the Electropolymerization of Two Different polypyrrol Films

film	m_f (μg cm^{-2})	Q (mC cm^{-2})	m_f/Q (mg C^{-1})	$x_S M_S + x_N M_N$ (g mol^{-1})
1	1.024	4.17	0.246	0.1
2	0.709	2.39	0.297	11.5

m_f , areal mass density of the film as determined by the EQCM; Q, passed electrical charge; $x_S M_S + x_N M_N$) amount of solvent (S) and neutral salt incorporated into the film.

The electrical charges Q have been roughly corrected for the double-layer contribution by subtracting the charge determined from a potential step experiment with the native Au electrode in 0.1 M KCl (background measurement). These experiments also showed that there is no Au dissolution at the relatively moderate polymerization potential of 0.5 V (SCE). Because the expression $x_S M_S + x_N M_N$ is small for film 1, the incorporation of neutral salt and solvent seems to be absent. In the case of film 2, there is an additional net mass increase of about 11 g/faraday, which means that some solvent or neutral salt or both is incorporated during the electropolymerization. This limited reproducibility is often encountered with the electropolymerization of conducting polymer films.

9.3.2 Characterization of Thin polypyrrol Films

After the freshly prepared polypyrrol films were washed several times with 0.1 M KCl, their doping / dedoping behavior was characterized by potential step and cyclic voltammetry

(CV) in 0.1 M KCl. It must be noted that for the characterization of the ion-exchange behavior step experiments are better suited than CV experiments.

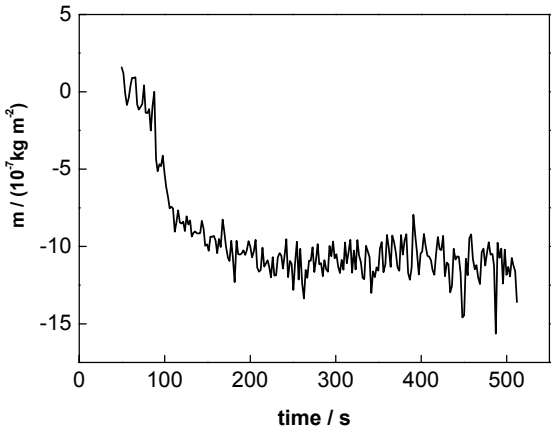

Figure 9.3: Mass change during the first reduction step (-0.5 V (SCE)) of a freshly prepared polypyrrol film in 0.1 M KCl solution.

The first reducing step (at -0.5 V (SCE)) was always accompanied by a mass decrease (Figure 9.3). Angle scans of the reflectivity (SPR spectra) showed that SPR can easily distinguish between the reduced (Figure 9.1, dashed line) and the oxidized states (Figure 9.1, dash-dot-dot-dash line) of polypyrrol. In the subsequent cycles, a continuous mass increase was observed (Figure 9.4).

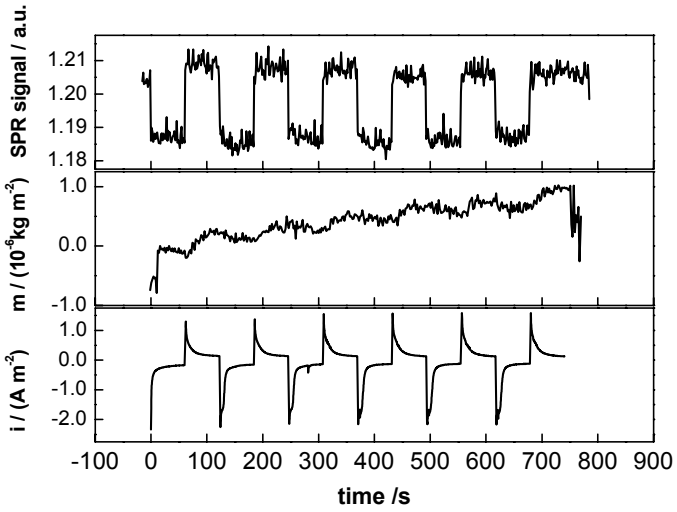

Figure 9.4: Current transients, mass change, and SPR signal of a thin polypyrrol film accompanying a sequence of potential steps between -0.5 and 0.3 V (SCE).

Bruckenstein et al. point out that the response function in CV experiments is more complex and not completely interpreted. [BH98] As described above, the electrical charges have been corrected with the help of background measurements. Cathodic charges contain the contribution from both the double layer and the oxygen reduction reaction. The latter is difficult to be taken into account, and it must be borne in mind that the correction procedure may introduce systematic errors.

The damping of the quartz and therefore of the film did not change during the redox switching (Figure 9.5). In CV experiments, the same behavior was observed. The SPR signal followed the potential steps instantaneously. The mass increase with increasing cycle number was found in all experiments. In some cases, this behavior was accompanied by a weak decrease in the optical reflectivity, mostly occurring in the oxidized state.

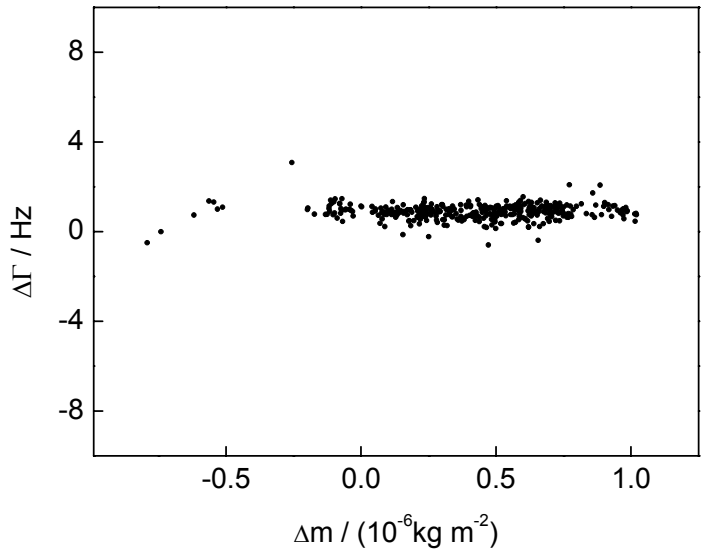

Figure 9.5: Damping change of the polypyrrol film during the redox switching shown in Figure 9.4.

9.4 Discussion

9.4.1 Electropolymerization of polypyrrol

The results on the electropolymerization of polypyrrol are in accordance with the previous study.[BKK+02] In that paper, a drift of the SPR signal after switching off the current (Figure 9.2, arrow) had also been observed and had been explained with relaxation processes in the polymer film. These processes cause a change in the dielectric constant and thus the SPR signal but no mass change. Because we observed no change in the dissipation of the quartz,

the changes in the mechanical impedance Z_f (eqn. 2.3.5) and thus the complex shear modulus G^* accompanying the relaxation processes seem to be small.

9.4.2 Doping/Dedoping Behavior of Thin polypyrrol Films

The first reduction steps of freshly prepared polypyrrol films always showed mass decreases (Figure 9.3), corresponding to $M_{app} \approx$ -5 g/mol. This value is definitely too small for a pure anion exchange, which would correspond to -35.5 g/mol (chloride). It is well known that for polypyrrol the apparent molar mass of the exchanged species depends on the preparation conditions [ZPG$^+$02] and the redox state (i.e., the actual potential).[GGP01] In other words, polypyrrol films can act as anion or cation exchange membranes or a combination of both. Transfer of solvent further complicates the situation. According to Gabrielli et al., the exchange of Cl^- has the smallest time constant for polypyrrol films at -0.55 V (SCE).[GGK$^+$02] An exchange of Na^+ with two water molecules also occurs, but it is a little bit more sluggish. At 0.3 V (SCE), the redox reaction involves only the anion.[GGK$^+$02] Obviously, in our case the ejection of anions (-35.5 g/mol) is counterbalanced by the ingress of cations (+39 g/mol, potassium) and the exchange of solvent ((18 g/mol, water). Bruckenstein et al. found that the transfer of the cation (sodium in their case) requires water transfer in the same direction [BBH00], and the work of Gabrielli shows that the number of solvent molecules transferred depends on the redox state of polypyrrol with a tendency to higher hydration numbers in the cathodic state.[GGK$^+$02] The constant damping behavior of the film during the redox switching (Figure 9.5) would indicate that the exchange of solvent (swelling and deswelling of the film) might play a minor role in our case. However, to further corroborate this statement more experiments are needed. One promising approach would be to include the determination of the frequency dependent electrogravimetric transfer function, $\Delta m/\Delta E$. It has been shown by Gabrielli et al. that this technique is capable of separating the individual contributions of solvent and ion transfer during redox cycling of conducting polymers.[GGK$^+$02] The increase of the reflectivity in the doping steps (Figure 9.4) could be interpreted as an increase of the film thickness.

However, it must be borne in mind that the angle of minimum reflectivity in the SPR curve shifts to larger angles when the film is switched from the reduced to the oxidized state (Figure 9.1). Furthermore, the minimum reflectivity increases, indicating less energy transfer to the surface plasmon when the film is in the oxidized state. This shows that the imaginary part of the dielectric constant ε'' (eqn. 9.1) increased with oxidation as a consequence of the

formation of the polaronic band and the "metallic" state of oxidized polypyrrol. In this study, the variation of the optical properties of the film during formation and doping/ dedoping processes are particularly strong. Because the details of the variation of the dielectric constant ε_f with the state of the film are not known, we do not analyze our data quantitatively here.

At the moment, we cannot make detailed statements about the mechanism giving rise to the continuously increasing mass seen in Figure 9.4. It seems that the incorporation of cations and solvent become more and more dominating as the film is rapidly switched between its reduced and oxidized form. From the SPR data, we can conclude that the film is already in the oxidized (i.e., polaronic) state when the mass increase occurs. This would indicate that a neutral species is involved because the electroneutrality condition requires a fast exchange of charged species. From a thermodynamic point of view, this means either that the film is not in equilibrium after its preparation or that it changes its structure or reactivity or both during the doping/ dedoping process.

9.5 Conclusions

This work shows that the electrochemical in situ combination of QCM and SPR is a powerful tool for the investigation of doping/dedoping behavior of conducting polymer films. Future work will aim at a fine-tuning of the experimental conditions (e.g., laser wavelength) and an analysis of the frequency dependence (transfer functions) of the individual signals. The aim is to extract more quantitative information from the SPR data such as the optical thickness and the dielectric constant of the film.

10 Electropolymerization and Doping/dedoping Properties of Polyaniline Thin Films

The electropolymerization and doping/dedoping properties of polyaniline ultra thin films on Au electrode surfaces were investigated by a combination of *in-situ* electrochemical techniques, i.e., electrochemical surface plasmon spectroscopy (EC-SPR), and the electrochemical quartz crystal microbalance (EC-QCM). In the EC-SPR measurements, we employed two wavelengths, i.e. 632.8 nm and 1152 nm in order to distinguish independently the electrochromic behavior. In addition, we used spectroelectrochemical transmittance measurements in order to further probe the optical properties of the polymer films as a function of the applied potential. The real and imaginary parts of the dielectric constant of the polyaniline thin film at several doping levels were quantitatively determined by taking into consideration the thickness values obtained from the EC-QCM measurement. The combination of both techniques provides a powerful method for probing the electrical, optical, and dielectric properties of conjugated ultra thin polymer films.

10.1 INTRODUCTION[11]

The electrochemical and optical quantitative analysis of π-conjugated polymer ultra thin films upon oxidation/reduction and doping/dedoping is of great interest in a number of applications. This includes electrochromic displays, [KYT84] battery electrodes, [MMS+85] sensors, and others. Because of many factors affecting the transition between doped and dedoped states of these polymer films, it is very difficult to quantitatively analyze each electrochemical event. A number of *in-situ* experimental techniques on the doping/dedoping process of conjugated polymers have been introduced, such as quartz crystal microbalance (QCM), [OB87] [CP99] FTIR, [ZD97] scanning probe microscopy (SPM) [NAS+95], etc.

Surface Plasmon Resonance Spectroscopy (SPR) has become a widely accepted method for the characterization and study of ultra thin films, interfaces and kinetic processes at surfaces. [Kno98] The combination of SPR with electrochemical measurements has been demonstrated as a powerful technique for the simultaneous characterization and manipulation of electrode/electrolyte interfaces. [TKK80] With electrochemical-SPR measurements, the

[11]Text partly adapted from: Akira Baba, Shengjun Tian, Fernando D. Stephani, Chuanjun Xia, Z. Wang, R.Advincula, D. Johannsmann and W.Knoll Electropolymerization and Doping / dedoping Properties of Polyaniline Thin Films as Studied by Electrochemical Surface Plasmon Spectroscopy and by Quartz Crystal Microbalance J.Electroanal. Chem. 562 (1): 95-103 JAN 15 2004

gold substrate that carries the optical surface mode is simultaneously used as the working electrode in the electrochemical experiments. One advantage of using the EC-SPR technique is that the electrochemical and optical properties are obtained *simultaneously* from films at the nanometer thickness scale. Recently, the EC-SPR technique has also been applied for the characterization of a variety of conducting polymer films. [BAK01] This involves in-situ monitoring of film swelling/deswelling and the measurement of electrochromic properties during electropolymerization or anion doping/de-doping. The EC-SPR technique has also been combined with surface plasmon field enhanced light scattering (SPFELS) and the quartz crystal microbalance (QCM) technique for the characterization of conducting polymer films. There are already several papers published on polymeric interface studies using combined QCM/SPR techniques, [LMJ00][PWR$^+$03] and the first attempt to combine the QCM/SPR with electrochemical measurements was reported by Bailey et al. [BKK$^+$02] We investigated the electrochemical process of polyaniline using the combined technique to obtain information on the morphological transition corresponding to the electrochemical and dielectric properties during in-situ electropolymerization.

Polyaniline (PANI) has been known and studied extensively since the 1980's. [MCR$^+$87] During the past two decades, the chemical and physical properties of polyaniline have been studied extensively under different conditions and, together with polypyrrole, [BBB$^+$03] this material has become one of the most popular conducting polymers. A complete review of the tremendous advances in the chemistry, electrochemistry, physics, theory and processing of polyaniline has been given by MacDiarmid. [Mac97] The interest in this conducting material and its derivatives is mainly due to its interesting electrical and optical properties together with its chemical tunability, ease of derivatization, solubility in a variety of solvents, low monomer cost and high yield in polymerization, ease of processing into fibers and films, and its excellent environmental stability. However, a complete characterization of their thermal, electrical, dielectric and structural properties is lacking thereby prohibiting their use in a variety of applications.

Polyaniline has three main stable oxidation states: fully reduced "leucoemeraldine" form, the 50% oxidized "emeraldine" form and the fully oxidized "pernigraniline" form. The most stable of those oxidation states is emeraldine base (EB), having equal amounts of reduced and oxidized repeating units (Fig.10.1). Each of them can exist in the form of its base or in the form of its protonated (doped) salt. Oxidative doping of the "leucoemeraldine" or protonic acid doping of the "emeraldine" produces the conducting form, with an increase in

conductivity, which can reach up to 10 orders of magnitude; the conductivity of the emeraldine salt can vary from 0.5 to 400 S/cm depending on the preparation. [CTS+92]

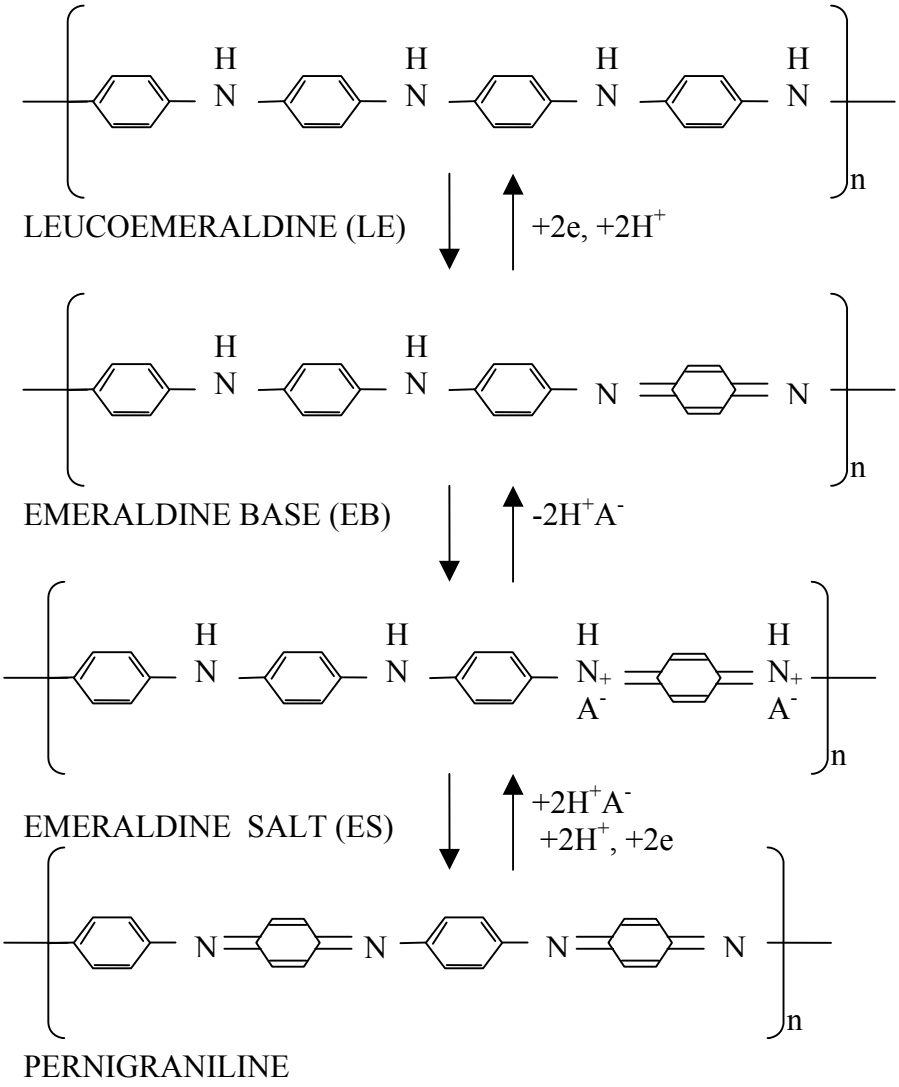

Fig.10.1 Proposed molecule formulas of polyaniline, which has several non-conductive oxidation states: the fully oxidized form is pernigraniline, and the fully reduced form is leucoemeraldine, and the half oxidized state is called emeraldine. Doping emeraldine base with acid (dopant) results to a conductive emeraldine salt (ES).

In this study, the quantitative investigation of an ultra thin polyaniline film during the oxidation/reduction and the doping/dedoping cycles is reported using EC-SPR and EC-QCM techniques. Firstly, aniline electropolymerization process was investigated. The deposition process was monitored by the QCM measurement, which allowed for the determination of the amount of charge transferred to each monomer during the electropolymerization. Secondly, oxidation/reduction and doping/dedoping of polyaniline films were investigated. The SPR reflectivity during the electropolymerization and subsequent doping/dedoping processes was

strongly affected by the changing dielectric constant of the deposited polyaniline film. Upon oxidation and reduction and upon doping and dedoping, the polyaniline films underwent a substantial increase and decrease, respectively, in conductivity. These changes occur simultaneously in the dielectric constants and thickness of the films, as probed by SPR and QCM. The film properties, i.e. thickness, real part and imaginary part of the dielectric constant upon doping/dedoping could be quantitatively determined by these techniques.

10.2 Experimental

10.2.1 Materials:

Aniline and Sulfuric acid were purchased and used as received from Aldrich and Riedel - de Haën, respectively. Freshly produced Milli-Q water (ultra pure water machine from Millipore, resistivity R ≥18.2 MΩ cm at 25°C) was used.

10.2.2 Electrochemistry:

All potentiostatic and cyclic voltammetry measurements were carried out using a one compartment, three-electrode cell driven by an EG&G PAR Potentiostat (Model 263A). In all the measurements, the working electrodes consisted of gold films (d ~ 50 nm) vacuum evaporated onto an LaSFN9 glass substrate (with an adhesion layer of 2nm Cr previously evaporated onto glass). The counter electrode was a Platinum wire and the reference was an Ag/AgCl aqueous electrode. All the potentials reported here are relative to this reference electrode. The solutions were carefully purged with Nitrogen before usage. All electrochemical measurements were performed without any potential cycling in background solution.

10.2.3 Electrochemical-Surface Plasmon Resonance Spectroscopy (EC-SPR) Measurement

The SPR set-up combines a three-electrode electrochemical cell with a Kretschmann configuration for the excitation of surface plasmons. Surface plasmons are excited by reflecting p-polarized laser light off the Au-coated base of the prism. The excitation sources employed were two different He-Ne lasers: $\lambda = 632.8\ nm$ and $\lambda = 1152\ nm$. Kinetic measurements were performed in order to monitor the formation of polyaniline film and the oxidation /reduction and doping/dedoping properties of deposited polyaniline thin film via reflectivity changes as a function of time. Angular measurements were also performed by scanning an incident angle range while the potential was held constant. For these experiments,

the gold film thickness was chosen for optimum excitation of the surface plasmon with both wavelengths (42 - 45 nm). The electrode surface area was 0.785 cm^2.

10.2.4 Electrochemical-Quartz Crystal Microbalance (EC-QCM) Measurement

Commercial 5 MHz AT-cut quartz crystals with Au electrodes and a crystal holder (Maxtek Inc. USA) were used. The front electrode of the crystal was used as the working area, and the back electrode was grounded, and both electrodes were connected at the back side to an impedance analyzer. On both sides of the crystal O-rings were used to prevent cell leakage.

The crystals were plasma cleaned before measurement. In order to separate the RF voltage signal (from the network analyzer) and the DC voltage signal (from the potentiostat), a combination of a capacitor and an inductance was used. [BS00] In EC-QCM measurement, the QCM front electrode (working electrode) surface area was about 1.4 cm^2. For thin films (where the film thickness is much less than the acoustic wavelength inside the piezoelectrical quartz material) a simplified form of mass-frequency relation (Sauerbrey equation) applies.

10.2.5 Transmittance Measurement

In order to complement the information obtained by the EC-SPR and the EC-QCM experiments, transmittance measurements were carried out with both lasers during the potential cycling (cyclic voltammetry), between -0.2 and 0.9 V at a scan rate of 20 mV/s. In this case, the gold film thickness was reduced to 20nm to allow transmission measurements on the glass substrates.

10.3 Results and Discussion

10.3.1 Electropolymerization of Aniline

Aniline was electrochemically polymerized onto the gold surface using a cyclic voltammetry (CV) program with a potential cycling between –0.2 V and 0.9 V at a scan rate of 20 mV/s. The cyclic voltammogram measurement obtained during the electropolymerization up to 7^{th} cycle is shown in Figure 10.2a. Similar measurements in aqueous H_2SO_4 with the above described potential range, has been finished by many others with similar results in redox behavior and good reproducibility. [ZCC88] [DMK95] [PM01] [PM02]

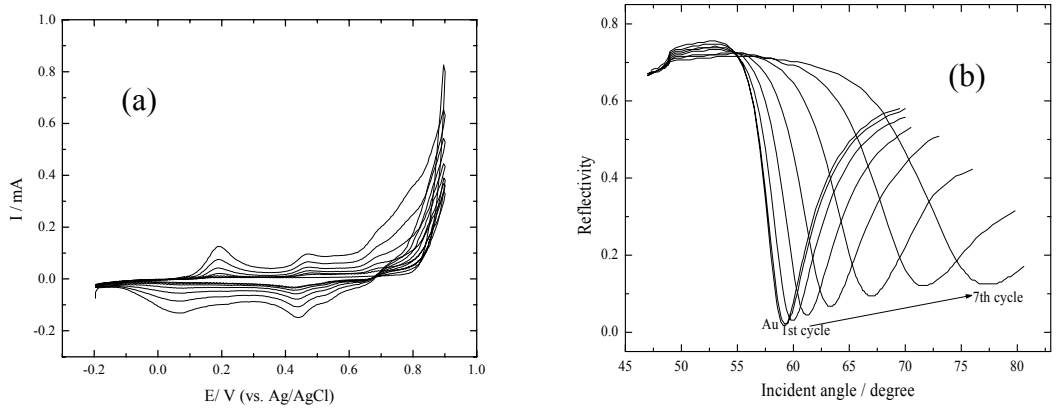

Figure 10.2: Cyclovoltamogram of the electropolymerization of aniline (0.02 M) in H_2SO_4 (0.5 M) solution and angular SPR reflectivity curves measured after each potential cycling.

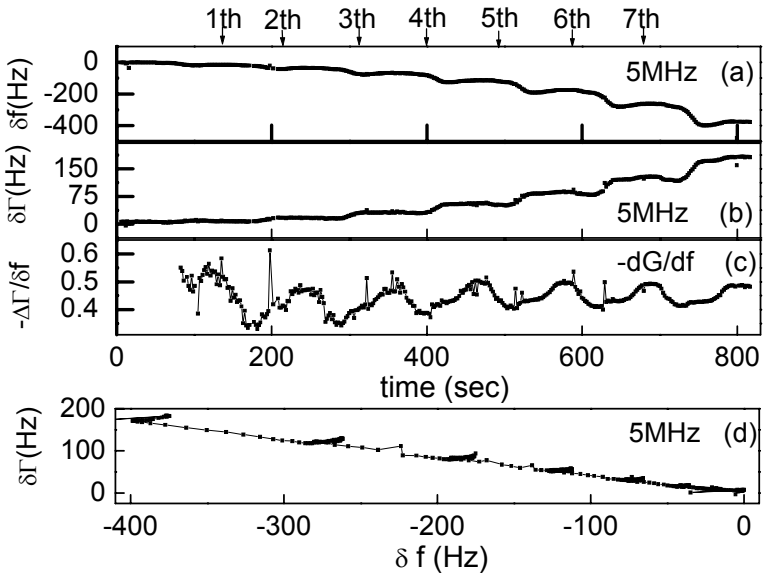

Figure 10.3: In situ monitoring of complex frequency change: (a) resonance frequency shift δf, (b) half-band-half-width shift δΓ, (c)-δΓ/δf change, (d) δΓ- δf plot , during cyclovoltametry measurement of aniline electropolymerization with potential cycling between -0.2 and 0.9 V at a scan rate of 20 mV/s.

The in situ formation of the PANI film on the gold electrode surface was monitored by the measurement of the transferred charge, by QCM and by SPR. Figure 10.3 shows the complex frequency change during electropolymerization by cycling the potential between –0.2 and 0.9 V at a scan rate of 20 mV/s. Each arrow shows the starting point of each potential cycle, i.e. -0.2V. In QCM measurements, Sauerbrey-approximation was used for analysis of frequency

shifts, stating that the frequency shift is mostly caused by deposition of mass on the crystal surface. Thus one obtains: $\delta f/f \approx -\delta m/m_q = -\delta m\,(2f_0/Z_q)$, with δf the frequency shift, f the frequency, f_0 the fundamental frequency, δm the areal mass density for the film, $m_q = Z_q/(2f_0)$ the areal mass density of the quartz plate, and $Z_q = 8.8 \times 10^6\ kg\ m^{-2}\ s^{-1}$ the acoustic impedance of the AT-cut quartz crystal.

The Sauerbrey approximation does not account for viscous losses or viscoelastic effects. In air, such viscoelastic effects scale as the cube of the film thickness and can be neglected. In liquids this is not the case. Because the liquid exerts a lateral stress onto the moving upper surface of the film, there are viscoelastic effects which scale *linearly* with the mass. This leads to a modified Sauerbrey equation, which is

$$\begin{aligned}\frac{\delta f + \mathrm{i}\,\delta\Gamma}{f} &\approx -\frac{\delta m}{m_q}\left\{1-\left(\frac{Z_q^2}{Z_f^2}-1\right)\frac{2\pi\,\mathrm{i}\,f\rho_l\eta_l}{Z_q^2}\right\}\\ &\approx -\frac{\delta m}{m_q}\left\{1-\frac{2\pi\,\mathrm{i}\,f\rho_l\eta_l}{Z_f^2}\right\}\\ &= -\frac{\delta m}{m_q}\left\{1-J_f\frac{2\pi\,\mathrm{i}\,f\rho_l\eta_l}{\rho_f}\right\}\end{aligned} \qquad (10.1)$$

where ρ_l is the density of the liquid, η_l is the viscosity of the liquid, Z_f is the acoustic impedance of the film, ρ_f is the density of the film, and $J_f = J_f' - i\,J_f''$ is the complex compliance of the film. In the second line the relation $Z_q \gg Z_f$ (film is softer than quartz plate) has been used. Note that the above expression is only the first term of a Taylor expansion in the film's mass δm. More complicated equations apply for films with a thickness comparable to the wavelength of sound.

For the analysis of conventional QCM data, the above equation is of limited use because it does not allow for a separation of mass effects and viscoelastic effects (the second term in the curly brackets). One defines a "Sauerbrey mass" which is the true mass times the unknown correction factor in curly brackets. If, on the other hand, the bandwidth (HBHW) is available, it can be interpreted in the frame of this equation. The ratio of $\delta\Gamma$ and $-\delta f$ should be independent of mass. This is indeed the case for our data, as shown in Figure 10.3(d).

The quantity $-\delta\Gamma/\delta f$ corresponds to the ratio of the imaginary and the real part of the curly bracket, namely:

$$\frac{-\delta\Gamma}{\delta f} \approx \frac{J'_f}{\rho_f/(2\pi f\rho_l\eta_l) - J''_f} \qquad (10.2)$$

The above equation allows for some further conclusions. Assuming $\rho_f \approx \rho_l$, the first term

in the denominator is on the order of the viscous compliance of the liquid. Further assuming that the liquid is much softer than the film, $J_f^{''} \ll 1/(2\pi f \eta)$, (a safe assumption for most polymeric films) one reaches the conclusion

$$\frac{\delta\Gamma}{\delta f} \approx J_f^{'}(2\pi f \eta_l) \approx J_f^{'}/(30 MPa^{-1}) \qquad (10.3)$$

where $\eta_l \approx 10^{-3}$ *Pa s* and $f = 5\times10^{6}$ *Hz* has been used in the second line. The quantity $-\delta\Gamma/\delta f$ therefore provides a measure of the film's elastic compliance. Note that this interpretation contradicts simple minded intuition to some degree: while one would naively associate a shift in bandwidth to dissipation inside a film, the detailed derivation shows that it is actually the *elastic* compliance, which is measured.

The application of this formalism to our data is illustrated in Figure 10.3. Figure 10.3(a) and (b) shows the raw data of δf and $\delta\Gamma$ mostly go in parallel, but not quite. During every anodic scan, the ratio - δf and $\delta\Gamma$ drops a little bit (Figure 10.3(c)). During every cathodic scan, it increases again. This behavior is largely independent of thickness (Figure 10.3(d), the "$\delta\Gamma$- δf -plot", where "$\delta\Gamma$ " stands for "dissipation"). The above quantitative discussion suggests that the (average) elastic compliance of the film is in the range of 10 MPa. It slightly drops during an anodic scan and recovers during a cathodic scan. One possibility for this is that the PANI film becomes more porous by de-doping but recovers by doping.

As previously reported, the first redox process (ca. 0.22 V in the anodic scan and 0.05 V in the cathodic scan) corresponds to the electron transfer from/to the electrodeposited polyaniline film. In order to compensate the charge of the polyaniline film, anion transport from/to electrolyte solution, i.e. anion doping and dedoping, [MCW97][HHM8] should occur. This phenomenon is responsible for the dramatic change in conductivity of the PANI film. The electrodeposition of polyaniline on the Au electrode proceeds via a radical cation polymerization mechanism. The second redox process (ca. 0.5 V and 0.45 V, for the oxidation and reduction, respectively) probably corresponds to side reactions such as decomposition of the polymer. The large currents observed at the positive end of the CV are due to the superposition of two distinct processes: one is the electron transfer from PANI film corresponding to the oxidation of the PANI film [GT85] and the other is the electron transfer from the aniline monomer corresponding to the oxidation of the aniline monomer to produce a precursor for the PANI film. A series of angular SPR curves taken after each potential cycling were shown in Figure 10.2(b). These scans were measured in the solution at open circuit potential (OCP ≈ 0.15 V). Shifts of the dip angles in the SPR curves were observed indicating that polyaniline was deposited onto the gold film electrode during each potential cycling.

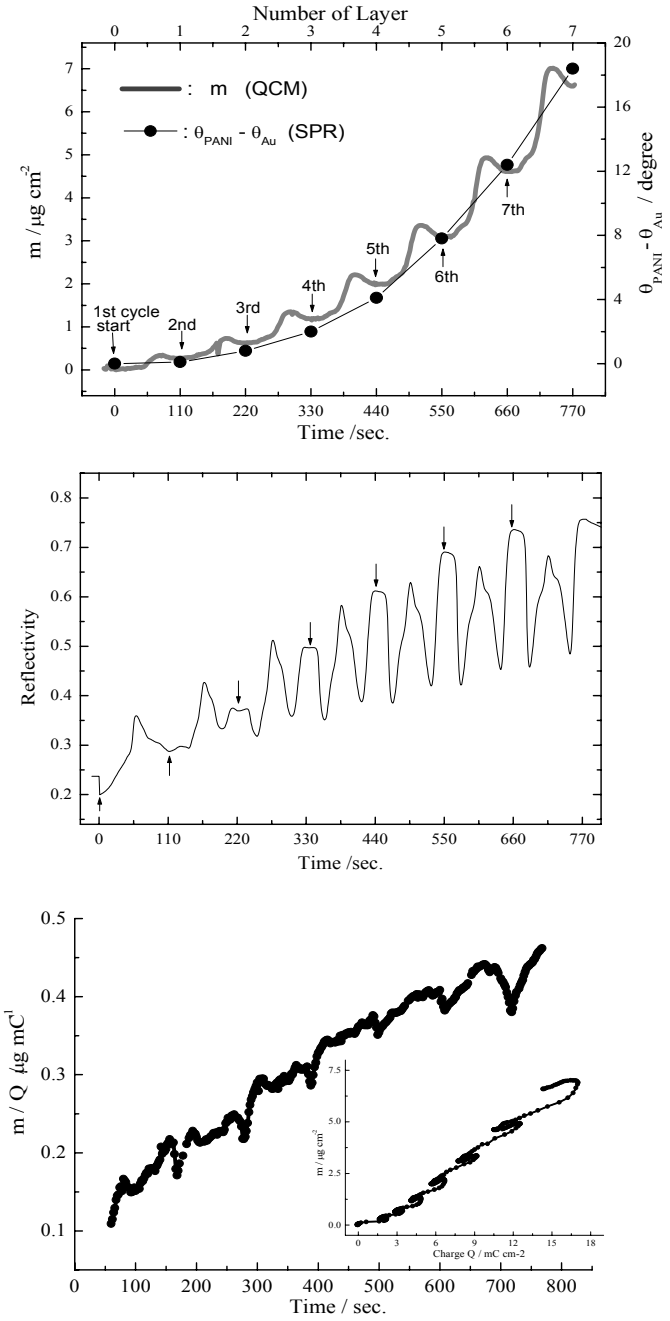

Figure 10.4: In situ monitoring of mass change during electropolymerization of aniline by potential cycling between -0.2 and 0.9 V at a scan rate of 20 mV/s, and corresponding SPR minimum angle shifts measured after each potential cycling (a) film growth monitored by QCM and SPR angle shift; (b) SPR dynamic measurement at angle 58.0 °; (c) m/Q plot during electropolymerization, with inset of mass change as a function of charge amount.

The in situ formation of the PANI film on the gold surface was monitored by measurements of the charge transferred, by QCM and by SPR. Shown in Figure 10.4(a) and (c) are the mass change as a function of time during the seven electropolymerization cycles

and corresponding SPR minimum angle shifts measured after each potential cycling. Each arrow shows the starting point of each potential cycle, i.e. -0.2V.

In observing the mass change, the increase in each of the cycles mostly corresponds to the oxidation of aniline to form the polyaniline film and the doping of anions into the deposited polyaniline film. The decrease of the curve is mostly due to the dedoping of the anions from the deposited polyaniline film. The trace of the SPR minimum angle shift was similar to the mass change at -0.2 V, i.e. at the end of each potential cycle. This indicates that the optical thickness corresponds to the acoustic mass.

The kinetic measurements for SPR were performed at a fixed angle, 58.0° slightly below the angle of the reflectivity minimum of the blank gold substrate. In the kinetic measurement of reflectivity, there is a large difference from the behavior of mass change. In the case of the SPR reflectivity, the curve is very sensitive to the thickness, the real (ε′) and the imaginary (ε′′) part of the dielectric constant. The increase in reflectivity at around -0.2 V was observed in the figure whereas no increase in charge amount and mass was found. This clearly indicates that the dielectric constant dramatically changes at this potential. Figure 10.4(c) shows the current efficiency, m/Q, during the electropolymerization process. From this plot, it was found that the current efficiency increases with time, i.e. corresponding thickness. This property is also seen in the change of mass as a function of charge passed as shown in the inset. In EC-QCM measurements, the areal mass density m_f during electropolymerization is related to the passed charge density Q. [BS00] In the case of electropolymerization for the conducting polymer, the theoretical value of the current efficiency, m_f/Q is calculated from,

$$\frac{m_f}{Q} = \frac{(M_M - 2M_H) + 0.5 \times x_A M_A}{(2 + x_A)\,F} \qquad (10.4)$$

where M_M, M_A, and M_H are the molar masses of monomer, incorporated anion, hydrogen, and x_A is the molar equivalents of the doping anion, and F is the Faraday constant, 96485 C mol^{-1}. The incorporation of water molecules and neutral salt, which can cause apparently higher m/Q values, was not included in this model. Here, if we assume x_A = 0.4, the theoretical current efficiency m/Q is expected to be 0.476 μg/mC. As shown in Figure 10.2(c), this value was much smaller than the theoretical value, but much larger (97.1 % after 7 cycles) than the initial potential cycles of electropolymerization (34.6 % after 1 cycle). This indicates that a number of side reactions, which do not correspond to mass increase, e.g. the formation of oligomers, take place with ultra thin film formation.

10.3.2 Doping/dedoping properties of deposited polyaniline thin films in monomer free solution

10.3.2 .1 potential cycling

The cyclic voltammetry and the corresponding QCM response curves are shown in Figure 10.5. The cyclic voltammetry was scanned between -0.2 and 0.9 V at a scan rate of 20 mV/s in 0.5 M H_2SO_4 monomerfree solution.

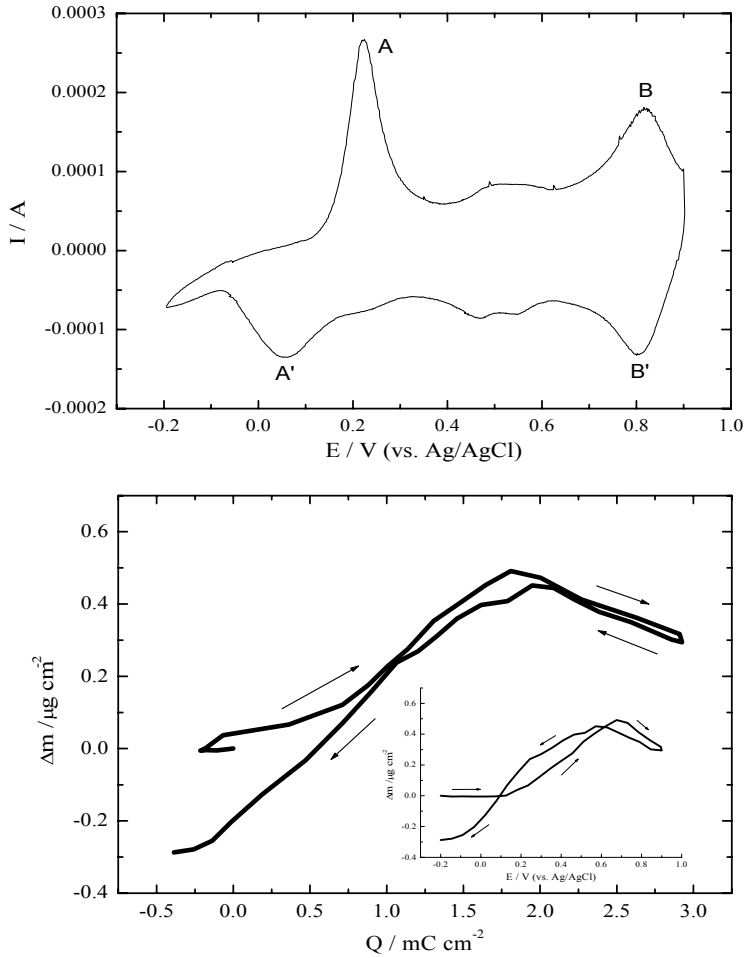

Figure 10.5: Cyclic voltammetry of deposited polyaniline film in monomer free solution and its mass response as a function of charge amount. Inset is mass response as a function of potential.

As mentioned before, the first redox peak (A, A´) is commonly assumed to correspond with the electron transfer from/to PANI film. In order to compensate the charge in PANI film, the anion doping and dedoping of the polyaniline film occurred. The second redox peak (B, B´) corresponds to a deprotonation and protonation process. The anion is expelled from the polyaniline film during deprotanation. [OB87]

The small peak at around 0.5 V is probably due to a side reaction in the polyaniline film. In the EC-QCM measurement, the mass increase at around 0.2 V corresponds to the doping of anions into the thin polyaniline film. First, the mass increased with amount of charge and then decreased. The m/Q value in this region is 0.27 μg/mC. This value is smaller than the theoretical m/Q value of SO_4^{2-} (0.50 μg/mC). This might be due to the charge compensation by participation of protons. At around 1.8 mC cm^{-2} (0.7 V), the mass started to decrease again. The m/Q value in this region is 0.18 mC cm^{-2}. This should be attributed to protonation, anion de-doping, and degradation.[KHC95] [SBE+87] The degradation leads to the dissolution of the soluble hydrolysis products from the oxidized film surface to the subphase.[OB87] This degradation could result in a mass loss after potential cycling as seen in figure 10.5. In our QCM experiments, a mass loss of 60 % of the deposited polyaniline film was observed after 10 potential cycles between -0.2 and 0.9 V.

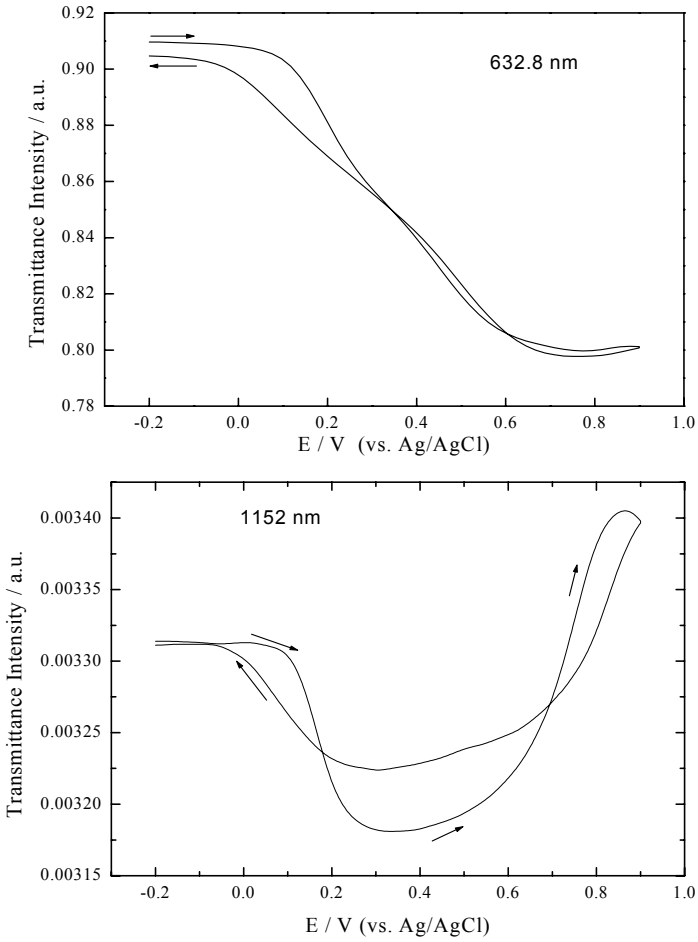

Figure 10.6: Transmittance intensity response at 632.8 nm and 1152 nm during potential cycling in monomer free solution

In the transmission measurements, the decrease of the transmitted intensity begins at around 0.1 V for both wavelengths, λ = 632.8 nm and λ = 1152 nm as shown in Figure 10.6. As can be seen from the Fresnel algorithm calculations, the transmitted intensity depends mostly on the imaginary part (ε'') of dielectric constant of the deposited polyaniline film. The absorption around 632.8 nm is generally attributed to the exciton absorption of the quinoid ring structures. [OB87][SBE+87] [SP89] Therefore, the decrease at around 0.1 V shows the oxidation of the polyaniline film from its leucoemeraldine to its emeraldine state, which contains quinoid ring structures. The absorption in the near infrared (NIR) region is known to be due to free charge carriers in a highly conductive state. [MXM95] [DL97][Kul95][SG02] At the first oxidation peak, the polyaniline film changes to the "emeraldine" form from the "leucoemeraldine" form. This "emeraldine" form is protonated in the acid solution so that it has a high conductivity. At the second oxidation peak, the polyaniline film is changed to the "pernigraniline" state from the "emeraldine" form and is deprotonated so that it is not highly conductive.

10.3.2.2 Potentiostatic measurements

In the previous section, a qualitative analysis of the imaginary part of the dielectric constant could be given for the three states of the polyaniline film. In order to be quantitative to all parameters of the films, i.e., its thickness, real and imaginary part of dielectric constant, we used EC-SPR and EC-QCM data taken under potentiostatic measurement conditions.

In Figure 10.7, the potentiostatic SPR scans are shown for both λ= 632.8 nm and λ=1152 nm, respectively. All SPR angular scans were started after each potential was applied for 2minutes in order to have the same conditions as in QCM measurements.

Some very interesting information was obtained from the analysis of these curves. It is noticed that the change in the reflectivity curves at around 0.2V occurs when the polyaniline "base" film changes, upon doping, into the corresponding conducting polyaniline salt. This process is reversible and many cycles can be performed without any noticeable variation (except for any degradation processes). If the film, in the absence of monomers, is kept at potentials higher than 0.65V, the SPR behavior is again similar to that of the insulating state and subsequent SPR scans at 0.65V, 0.4, -0.2V, 0.4V, 0.65V showed no difference. This indicates that in the absence of the aniline monomer, oxidation at potentials higher than 0.85V leads to an irreversible degradation of the electrochemical response of the polyaniline film.

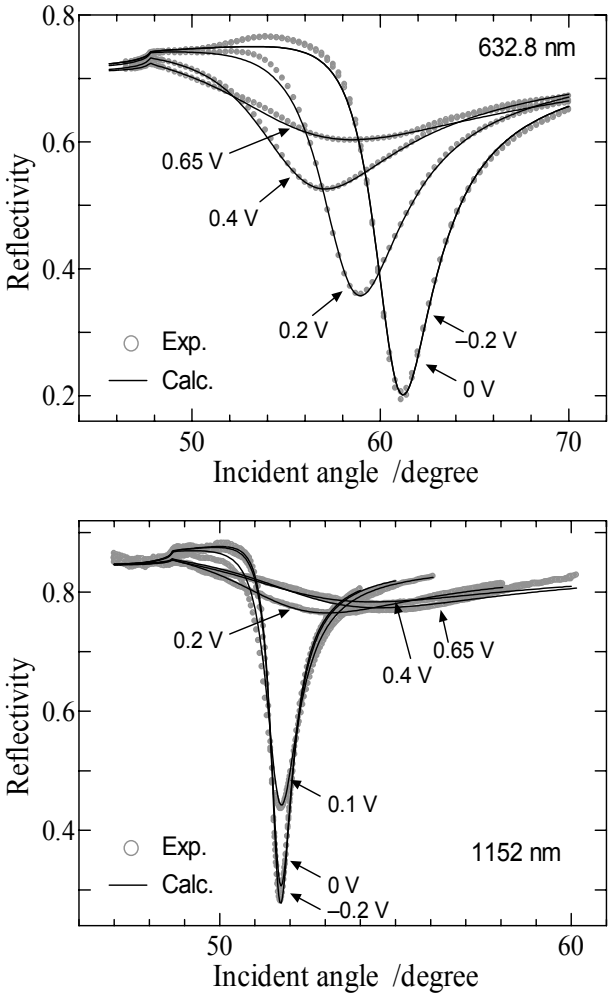

Figure 10.7: Experimental angular SPR reflectivity curve (dotted) and calculated curve (solid) under applied potential at 632.8 nm and 1152 nm.

Since it is difficult to obtain independent information on the thickness and the real part and imaginary part of the dielectric constant from mere SPR measurement, we used QCM under potentiostatic measurement conditions. Because the change of the imaginary part of the frequency, which directly corresponds to the dissipation, is 180 Hz in our experiment, the Sauerbrey equation is applied to relate frequency shifts to mass changes. [Sau59]

. Figure 10.8 shows the potentiostatic QCM measurements for several potentials and the corresponding thickness, roughly estimated on the assumption of a mass density of 1.3 g/cm^3 for comparison with EC-SPR results. [OB87][SG02]

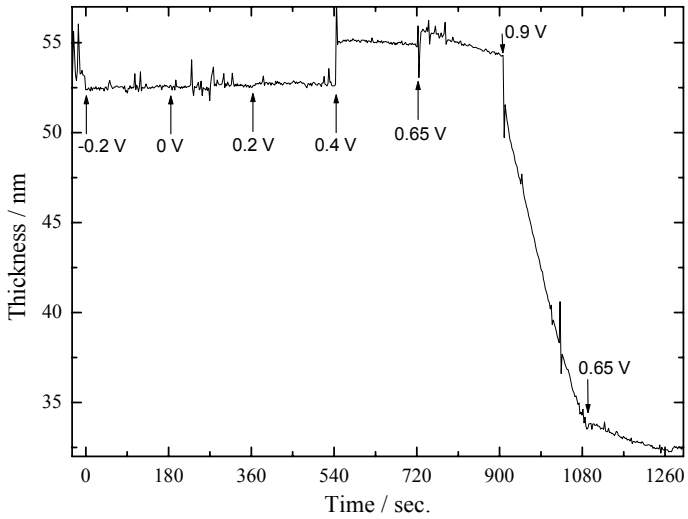

Figure 10.8: Thickness change measured by QCM under potential applied.

For changing potential, a step potential program was used. In contrast to that the SPR reflectivity curves, which has a large change at 0.2 V, the thickness from the QCM measurement was constant between 0 V and 0.2 V. As can be seen from Fig. 10.8, a substantial degradation and loss of material sets at 0.9 V so that one can not obtain a meaningful film thickness at 0.9 V. The loss of film thickness at 0.9 V was found to be 38 % after 3 minutes. Fitting the experimental SPR reflectivity results with the thickness values obtained from QCM measurement (except the value of 0.9 V) gives the theoretical reflectivity curves that are also shown in Figure 10.7. The calculation was done by using Fresnel's equations for Prism/Cr/Au/PANI/Electrolyte solution architecture. Details for fitting procedure can be found elsewhere. [Kno98] Although the SPR resonance at λ = 1152 nm is very broad at high potential, excellent fitting curves were obtained in most cases. The obtained fitting parameters are shown in Figure 10.9.

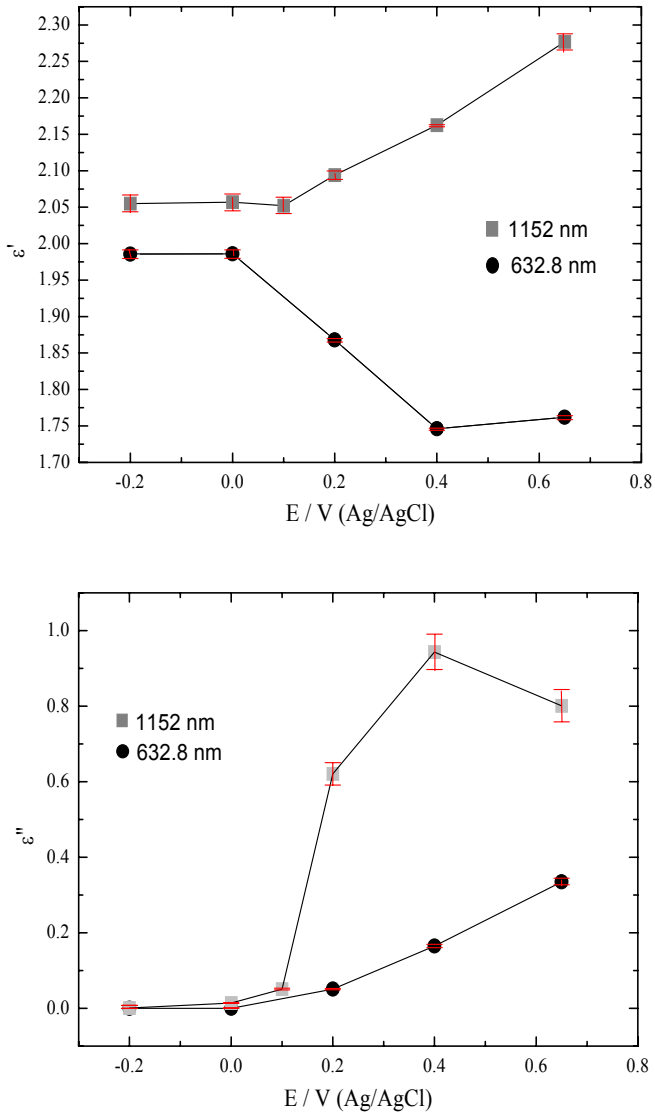

Figure 10.9: Real part (ε′) and imaginary part (ε′′) of dielectric constants calculated for several different potentials.

Dramatic changes both in real part and imaginary part of dielectric constants were determined at both wavelengths. The error bars in Figure 10.9 are based on the density fluctuation of the polymer upon doping/dedoping, that is 1.25-1.35. Based on these calculations, the accuracy for determination of complex dielectric constant is estimated to be better than ±0.02 for the real part and ±0.10 for the imaginary part of the dielectric constant in this density range, *i.e.*, EC-SPR measurements are able to determine the complex dielectric constants of the conducting polymer films in the doped/de-doped state rather independently of the film density uncertainty. Thus, the electrochromic phenomena of PANI films can be characterized by this EC-SPR technique with high sensitivity, which may lead to new designs

for SPR-based sensors/biosensors based on the electrochromism of thin conducting polymer films. Similar experiments are currently underway with other conducting polymers such as poly (3,4-ethylenedioxythiophene) (PEDOT).

10.4 Conclusions

Using the combined electrochemical-surface plasmon resonance spectroscopy (EC-SPR) and the electrochemical-quartz crystal microbalance (EQCM) techniques, it was possible to monitor quantitatively the electropolymerization and doping/dedoping properties of polyaniline films on a flat gold substrate surface. Transmittance and potentiostatic SPR measurements were carried out with two wavelengths in order to obtain independent information about the electrochromic properties of the thin polyaniline film. The change in the electrochemical/optical properties of the thin film upon doping produces a dramatic change in the SPR response primarily due to an obvious change in the real and imaginary parts of the dielectric constant. The contribution of the thickness changes can be determined independently by EC-QCM measurements. Thus, using these experimental combinations, we have demonstrated the ability to obtain independent quantitative values on thickness, real and imaginary part of dielectric constant at two wavelengths. These techniques should be a powerful combination for the quantitative analysis of other conjugated polymer ultra thin films.

11 Polyelectrolyte Multilayer formation of PSS/PAH

The consecutive adsorption of polyanions and polycations has become a widely used technique for the preparation of organic mutilayers with well defined architecture. In polyelectrolyte mutilayer the electrostatic attraction is the driving force for the adsorption, which is sterically less demanding than the formation of covalent bonds. The adsorption of polyelectrolyte leads to an overcompensation and reversal of the surface charge of supported substrates, which allows the subsequent adsorption of oppositely charged polyelectrolyte to form the next layer.

Generally speaking, for a salt free system (not considering the effect of counterions) the thickness of polyelectrolyte mutilayers increases linearly with the number of deposited bilayers. However by increasing the salt concentration (normally monovalent salts like NaCl) for some given polyelectrolyte systems, the adsorption film thickness increases superlinearly with the number of bilayers.

11.1 Materials and experimental

Polyethylenimine (PEI) produced by Sigma-Aldrich Co., which is a branched polymer with an average Mn *ca.*60,000 by GPC, and an average Mw *ca.*750,000 by Light Scattering, was used with a concentration of 2.9×10^{-2} M in water. Its monomer molecular weight is 43 g/mol.

Sulfonated Polystyrene-block-poly (ethylene-ran-butylene)-block-polystyrene (PSS, Sulfonated polystyrene accounts for 45-55%) produced by Sigma-Aldrich Co., a linear polymer with a Mw of 70,000 g/mol, was used in 0.5 M NaCl solution at a concentration of 3×10^{-3} M. Its simplified monomer molecular weight is 206.5 g/mol.

Polyallylamine hydrochloride (PAH) produced by Sigma-Aldrich Co., a linear polymer with a Mw of 70,000 g/mol, was used in 0.5M NaCl solution at the same concentration, i.e. 0.003 M, for comparison reasons. Its monomer molecular weight is 93.5 g/mol.

Before the measurement, the quartz crystal with gratings was plasma cleaned for 30 min and then it was installed inside the liquid cell. Then the cell was rinsed with water for several times and then PEI solution was injected inside the liquid cell and kept there for one night. After that the cell was rinsed for two times with water (wait a few minutes between each

injection), then with 0.5 M NaCl buffer solution for three times. The measurement was started with PSS first for 7 minutes, and then the cell was rinsed with 0.5 M NaCl solution for two times. Then the measurement with PAH was started for another 7 minutes. After that the cell was rinsed with 0.5 M NaCl solution for two times. Repeat the process, and polyelectrolyte multilayer was formed on the quartz surface.

11.2 Results and Discussion

Fig.10.1 lists the molecular formulas of Polyethylenimine (PEI), Sulfonated Polystyrene-block-poly (ethylene-ran-butylene)-block-polystyrene (PSS) and polyallylamine hydrochloride (PAH).

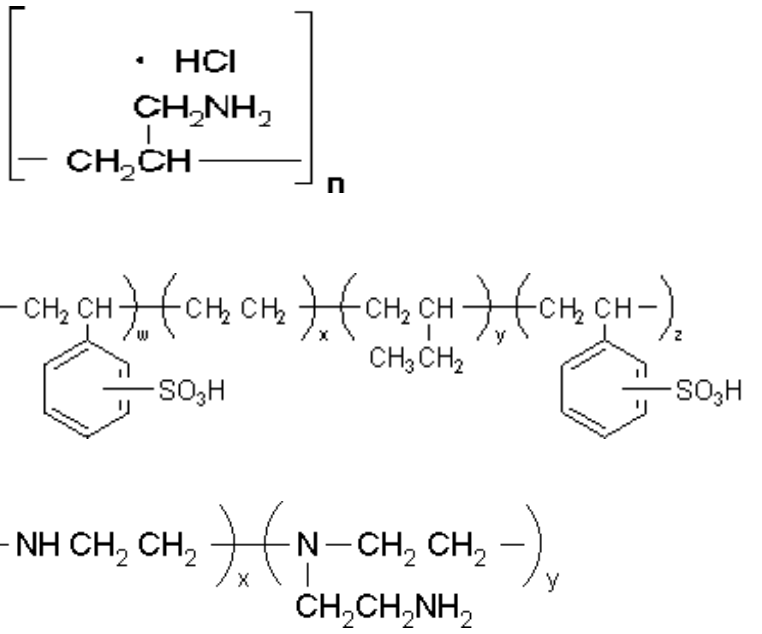

Figure 11.1: Schematic of molecular structure of PAH, PSS and PEI (adapted from company webpage of Sigma-Aldrich). In calculation of PSS concentration, its monomer molecular weight is based on its simplified form, ie. 206.5.

Figure 11.2 shows a schematic of the preparation of polyelectrolyte multilayer architecture. By consecutive solution exchange cycles (polyelectrolyte solution – pure solution – oppositely charged polyelectrolyte solution, etc.), multilayers of up to 22 PSS/PAH bilayers adsorbed to the PEI covered gold surface. There appears no limit for the number of bilayers.

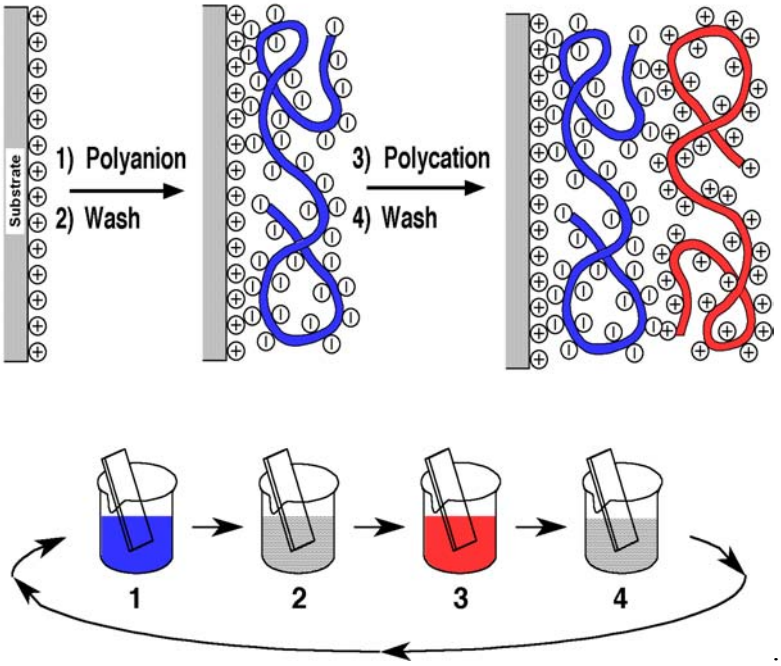

Figure 11.2: Schematic of the Layer-by-Layer Deposition Process (adapted from webpage http://www.chem.fsu.edu/multilayers/Schematic_of_the_LayerbyLayer_files/slide0002.htm)

At the first few bilayers of polyelectrolyte multilayer growth, the film thickness increases slightly in an exponential way, after that the exponential growth mode is not so obvious. The film thickness growth detected by SPR was in general parallel to that by QCM (as shown in Fig.11.3). By increasing the salt concentration for this polyelectrolyte system, the film thickness and adsorption amount can increase superlinearly with the number of deposited bilayers. Several explanations for this superlinear growth mode of multilayers have been proposed. The common concept is that in polyelectrolyte layer the electrostatic attraction is the driving force for the adsorption, which is sterically less demanding than the formation of covalent bonds. The adsorption of polyelectrolyte leads to an overcompensation and reversal of the surface charge of supported substrates, which allows the subsequent adsorption of oppositely charged polyelectrolyte to form the next layer. Ruths et al.[RED$^+$00][RSG01] and McAloney et al. [MSD$^+$01] attributed the change from linear to superlinear growth induced by increased salt concentration to roughness effects of the multilayers formed at higher salt concentrations. Voegel et al.[PLH$^+$01][BBS$^+$03]also claimed salt effects but supposed a diffusion mechanism to explain the exponential growth mode. According to their diffusion mechanism, at least one of the polyelectrolyte can diffuse in and out of the film during the mutilayer buildup process.

In each bilayer PSS seems to cause a larger thickness growth than PAH, indicating a larger amount of deposited PSS than PAH in each bilayer. This difference is mostly due to the different charge densities of a PSS layer and a PAH layer, which can be seen from their molecular formulas shown in Fig.11.1. Apparently, PAH has a much larger charge density than PSS. Owing to this difference in charge densities, PSS and PAH adopt a different conformations, and thus adsorb in different amounts. [TBL^{+}03]

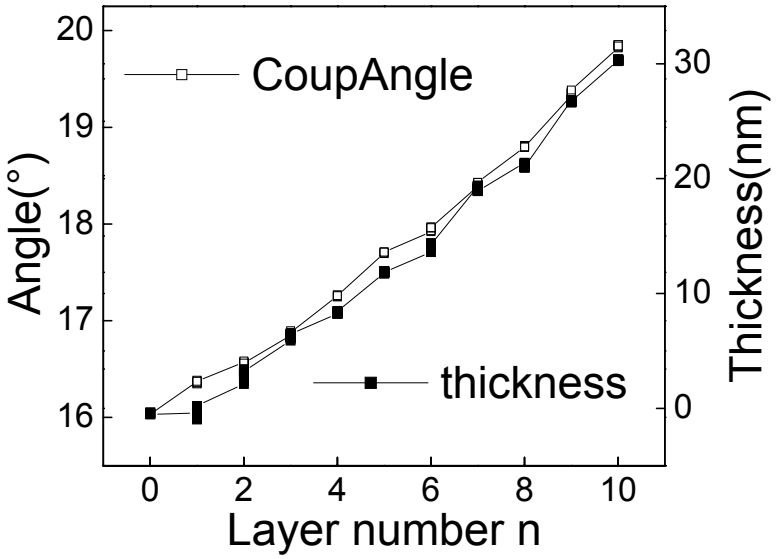

Figure 11.3: Exponential growth of polyelectrolyte multilayer thickness detected by SPR and QCM. PSS concentration: 3×10^{-3} M in 0.5M NaCl solution; PAH concentration: 3×10^{-3} M in 0.5 M NaCl solution.

For each bilayer, the PSS layer thickness is larger than that of PAH, indicating that a larger amount of PSS is deposited than PAH. PSS and PAH adopt different conformation, and thus adsorb in different amounts, because of this charge density difference. The calculated average bilayer thickness is 6 nm, assuming that the film density is 1.0×10^{3} kg/m³.

Usually the polyelectrolyte film formation is very quick. In measurement shown in Fig.11.4, we started the combined measurements of QCM and SPR before the injection of polyelectrolyte solution. From Fig.11.4 we can find that the injection of polyelectrolyte solution into the liquid cell had a much larger effect on QCM measurement than SPR result, and there was a large noise in QCM result. For QCM measurement it took a longer time to reach a new level thickness in equilibrium than that for SPR measurement. So the concentration of both polyelectrolyte solutions is less than 3×10^{-3} M, and the thickness growth

mode was linear growth mode; the calculated average bilayer thickness was 6nm (assuming that the film density is 1.0 ×10³ kg/m³); in terms of SPR coupling angle, its average value was 0.64°. Here we can also find that PSS has a larger contribution in bilayer thickness than PAH, as confirmed by both QCM and SPR measurements, because of its smaller charge density.

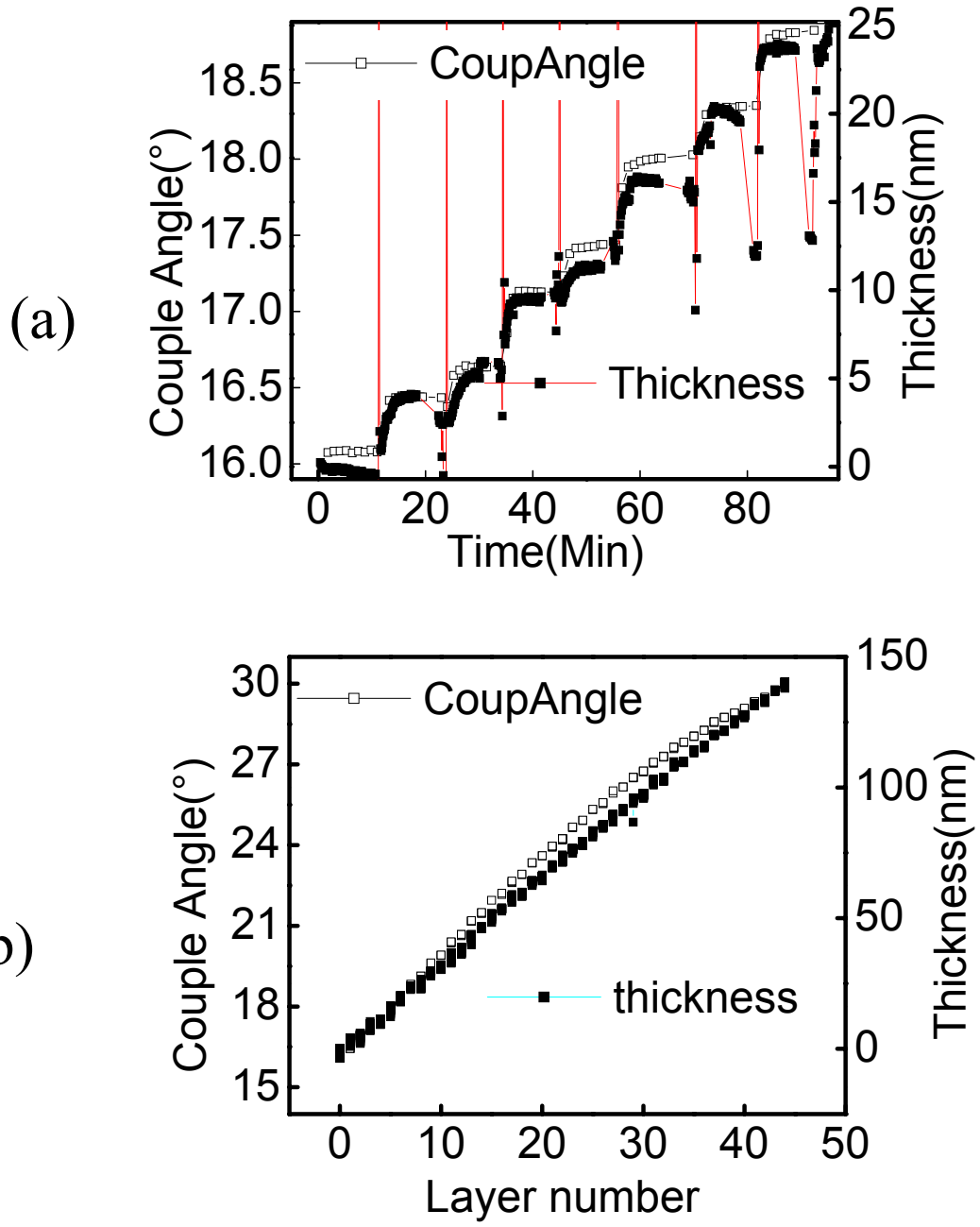

Figure 11.4: Linear growth of polyelectrolyte multilayer thickness detected by SPR and QCM. PSS concentration: less than 3×10^{-3} M in 0.5M NaCl solution; PAH concentration: less than 3×10^{-3} M in 0.5M NaCl solution. (a) plot of thickness vs. time, showing the dynamic mixing process of polyelectrolyte with NaCl buffer solution; (b) plot of thickness vs. layer number.

Lukkari et al got a similar result in polyelectrolyte (P3TOPS/P3TOPA, P3TOPS/PDADMA, PSS/P3TOPA) multilayer formation detected by using QCM measurements, see ref [LSA^{+}02]. It is revealed that all the polyelectrolyte multilayers appeared very soft. The films resembled hydrogels, and the average softness was comparable to that of adsorbed protein films.

11.3 Conclusions

Polyelectrolyte (PSS and PAH) multilayer thickness growth is concentration dependent: at a concentration 0.003M, the measured layer thickness growth mode is superlinear (exponential growth at beginning); at a smaller concentration (less than 0.003 M), layer growth is linear (exponential growth at the beginning is not obvious). For each bilayer, the PSS layer thickness is larger than that of PAH, indicating that a larger amount of PSS is deposited than PAH, because of the charge density difference. PSS (sulfonated Polystyrene) and PAH (Polyallylamine hydrochloride) adopt different conformation, and thus adsorb in different amounts. Calculated average bilayer thickness is about 6 nm, assuming that the film density is $1.0 \times 10^3 kg/m^3$; and in terms of SPR coupling angle, the average optical thickness is about 0.64° per bilayer.

12 Conclusions

The Quartz Crystal Microbalance (QCM) is designed to measure the mass as well as the viscoelastical properties of thin films deposited onto its electrode surface. Thickness measurements in liquids are problematic because the mass includes trapped solvent, which has entered the film due to swelling. In order to get a better understanding of the QCM measurements, we use a combined measurement technique, i.e. QCM and SPR (Surface Plasmon Resonance Spectroscopy).

Shallow gratings were etched into the surface of AT-cut quartz crystals. Using these quartz crystals with shallow gratings, we can make combined in-situ measurements with the QCM and SPR. QCM and SPR measurements work independently and are controlled separately by two computers. The optical thickness as determined via the coupling angle in SPR measurements was not affected by the shear oscillation of the quartz during the QCM measurements. There was, however, a small influence of the laser beam on the apparent acoustic thickness, which is attributed to thermally induced stresses in the electrodes.

We measured the elastic shear modulus of evaporated gold and silver films using quartz crystal resonance excited across an air gap; the measured shear moduli of gold and silver were around 15 GPa and 20 GPa respectively. These values are smaller than the corresponding bulk values.

We detected the adsorption of mercury vapor onto an alkanethiol and alkanedithiol SAMs covered gold surface at room temperature and measured the liquid-solid phase transition of mercury using the quartz crystal microbalance. Around the transition point, there is an increase in the half-band-half-width, while the resonance frequency is not affected. QCM measurements show that mercury adsorbed onto SAMs covered gold surfaces is in the form of nano-droplets instead of nano-particles.

The swelling behavior of chitosan film in different pH solutions was studied using combined QCM and SPR measurements. QCM and SPR show different results: QCM shows a maximum acoustic thickness of swelling at pH=6.6; on the contrary, SPR shows a continuous swelling behavior in optical thickness with decreasing pH values.

The adsorption of linear pNIPAm on gold surfaces at 31°C was measured in situ by QCM and SPR. The SPR coupling angle (related to the optical thickness) and QCM resonance frequency shift (related to the acoustic thickness) increase in parallel for most of the adsorption process. The change in dissipation is proportional to frequency shift. It can be inferred that pNIPAm adsorption occurs via vertical growth of layer thickness.

Temperature induced swelling and deswelling of cross linked pNIPAm gels in water was detected by combined acoustic and optical measurements. The shifts in SPR coupling angle are explained in terms of decrease in refractive index of pNIPAm film at low temperatures. The acoustic data are dominated by the changes in thickness. With a higher cross linking degree, the film resonance is less pronounced, which decreases the sensitivity of pNIPAm as a sensing transducer, but improves its reproducibility and reliability.

The electropolymerization and doping/dedoping properties of conducting polymer films (such as polyaniline and polypyrrole films) on gold electrode surfaces in aqueous solutions were quantitatively investigated by QCM and SPR. It was found that the refractive indices of these films change with different redox states.

Polyelectrolyte multilayer formation was in situ detected by QCM and SPR techniques. The layer by layer thickness growth mode is linear when the polyelectrolyte solution is salt free or at a low ion concentration. The thickness growth is superlinear at the beginning of growth when a higher salt concentration is used, because of the so-called charge overcompensation effect. The polycation layer and polyanion layer have different thickness in each bilayer because of different charge densities.

Bibliography

[AAK94] J. Aarik, A. Aidla, K. Kukli, *Appl. Surf. Sci. 75* (**1994)**180.

[AB87] R.M.A. Azzam, N.M. Bashara, *Ellipsometry and Polarized Light*, Elsevier, Amsterdam **(1987).**

[AIS+94] E.F.Aust, S. Ito, M.Sawodny and W. Knoll, Trends in Polymer Science TRIP vol. 2 (9) (**1994)** 313.

[AKR00] K.F. Arndt, D. Kuckling, A. Richter, *Polymers for Advanced Technologies.* 11, **(2000)** 496.

[AWM04] A. K. Aliganga, Z. Wang, S. Mittler, Chemical Vapor Deposition of Mercury on Alkanedithiolate Self-Assembled Monolayers, J. Phys. Chem. B (**2004**)

[BAK01] A. Baba, R. C. Advincula, W. Knoll, *In "Novel Methods to Study Interfacial Layers", Ed. by Möbius, D. and Miller, R., Elsevier Science, Studies in Interface Science* 11 **(2001)** 55.

[BBB+03] A. Bund, A. Baba, S. Berg, D. Johannsmann, J. Luebben, Z. Wang, W. Knoll, J. Phys. Chem. B.; 107 (28) **(2003)** 6743.

[BBH00] S. Bruckenstein, K. Brzezinska, A. R. Hillman, *Electrochim. Acta 45* (**2000)** 3801.

[BBS+03] F. Boulmedais, V. Ball, P. Schwinte, B. Frisch, P. Schaaf, J.C. Voegel, Langmuir 19 **(2003)** 440.

[BH98] S. Bruckenstein, A. R. Hillman, J. Phys. Chem. B 102 **(1998)** 10826.

[BHM98] F.T. Buoninsegni, R. Herrero, M.R. Moncelli, *J. Electroanal. Chem.* 452 (**1998)** 33.

[BKK+02] L. E. Bailey, D. Kambhampati, K. K. Kanazawa, W. Knoll, C. W. Frank, *Langmuir* 18 (**2002)** 479.

[BS00] A. Bund, G. Schwitzgebel, Electrochim. Acta 45 (**2000)** 3703.

[BTS+04] A. Baba, S. Tian, F.D. Stephani, C. Xia, Z. Wang, R. Advincula, D. Johannsmann and W. Knoll, J. Electroanal. Chem. 562 (1) **(2004)** 95.

[CG83] J.C. Charmet, P.G. de Gennes, *J. Opt. Soc. Am.* **73**, **(1983)** 1777.

[Com89] R.G. Compton, *Comprehensive Chemical Kinetics*, Vol. 28 (Elsevier, New York) (**1989)**.

[CP99] S.Y. Cui, S.M. Park, *Synth. Met.* 105 (**1999)** 91.

[CTS+92] Y. Cao, G. M. Treacy, P. Smith, A. J. Heeger, *Appl. Phys.Lett.,* 60 **(1992)** 2711.

[DJ98] A. Domack and D. Johannsmann J. Appl. Phys.83 (3) **(1998)** 1286.

[DM92] L. Duic, Z. Mandic, *J. Electroanal. Chem.* 335 **(1992)** 207.

[DMK95] L. Duic, Z. Mandic, S. Kovac, *Electrochim. Acta* 40 **(1995)** 1681.

[DPR+97] A. Domack, O. Prucker, J. Rühe, D. Johannsmann, *Phys. Rev. E* 56, **(1997)** 680.

[DU97] L. Daikhin, M. Urbakh, *Faraday Discuss.* 106, **(1997**) 27.

[EHH99] D.L.Elbert, C.B. Herbert, and J.A.Hubbell Langmuir 15 **(1999)** 5355.

[EWS01] I. Efinov, S. Winkels, J. W. Schultze, J. Electroanal. Chem. 499 **(2001)** 169.

[FR92] J. Falbe, M. Regitz, Eds. *Römpp Chemielexikon*, 9th ed.; Thieme Verlag: Stuttgart, Germany, 5 **(1992)** 3737.

[FSS+93] G.J. Fleer, M.A. Cohen Stuart, J.M.H.M. Scheutjens, T. Cosgrove, and B. Vincent: *Polymers at Interfaces*, Chapman and Hall, London **(1993)**.

[GE80] J. G. Gordon, S. Ernst, *Surface Science* 101 (**1980)** 499.

[GGK+02] C. Gabrielli, J. Garcia-Jareno, M. Keddam, H. Perrot, F. Vicente, J. Phys. Chem. B 106 **(2002)** 3182.

[GGP01] C. Gabrielli, J. J. Garcia-Jareno, H. Perrot, Electrochim. Acta 46 **(2001)** 4095.

[GLM+00] P. Guedon, T. Livache, F. Martin, F. Lesbre, A. Roget, G. Bidan, Y. Levy, *Anal. Chem. 72* **(2000)** 6003.

[GM94] V.E. Granstaff, S.J. Martin, *J. Appl. Phys.* 75, **(1994)** 1319

[Gra00] G. Graziano, *Int. J. Biol. Macromol.* 27 **(2000)** 89.

[Gro79] P. Grosse, Freie Elektronen in Festkoerpern, Springer Verlag **1979**.

[GT85] E. M. Genies, C. J. Tsintavis, *J. Electroanal. Chem.* 195 (**1985)** 109.

[GW97] J. Gao, C. Wu,.*Macromolecules* 30 **(1997)** 6873.

[HES] A. R. Hillman, I. Efimov, M. Skompska, *Faraday Discuss. 121* **(2002)** 423.

[HGJ+88] K.E. Heusler, A. Grzegorzewski, L. Jäckel, and J. Pietrucha Ber. Bunsenges. Phys. Chem. 92 (1988) 1218.

[HHC+01] R.E. Holmlin, R. Haag, M.L. Chabinye, R.F. Ismagilov, A.E. Cohen, A. Terfort, M.A. Rampi, G.M. Whitesides, *J. Am. Chem. Soc.*, *123* (**2001)** 5075.

[HHI+99] Holmlin, R.E.; Haag, R.; Ismagilov, R.F.; Cohen, A.E.; Terfort, A.; Rampi, M.A.; Whitesides, G.M.; *Book of Abstracts, 218th ACS National Meeting*, New Orleans, (**1999).**

[HHM86] W. S. Huang, B. D. Humphrey, A. G. MacDiarmid, *J. Chem. Soc. Faraday Trans. 1 (***1986)** 82.

[HKN+01] F. Höök, B. Kasemo, T. Nylander, C. Fant, K. Sott, H. Elwing, *Anal. Chem.* 73, **(2001)** 5796.

[HKF03] M.E. Harmon, D. Kuckling, C.W. Frank, *Macromolecules* 36 **(2003)** *162.*

[HPH94] D.M. Hercules, A. Proctor, M. Houlla, *Acc. Chem. Res.* 27 (**1994)** 387.

[HRB+98] F. Höök, M. Rodahl, P. Brzezinski, B. Kasemo, *Langmuir* 14 **(1998)** 729.

[HRH+99] R. Haag, M.A. Rampi, R.E. Holmlin, G.M. Whitesides, *J. Am. Chem. Soc. 121*, (**1999)** 7895.

[HRW98] R. Haag, M.A. Rampi, G.M. Whitesides, *Book of Abstracts, 216th ACS National Meeting, Boston,* (**1998)**.

[IHM+97] Y. Iwasaki, T. Horiuchi, M. Morita, O. Niwa, *Electroanalysis* 9 (**1997)** 1239.

[IPS+00] G. Inzelt, M. Pineri, J. W. Schultze, M. Vorotyntsev, A.Electrochim. Acta 45 **(2000)** 2403.

[JG02] B. Jeong, A. Gutowska, *Trends in Biotechnology* 20 **(2002)** 305.

[JMW+92] D. Johannsmann, K. Mathauer, G. Wegner, and W. Knoll, *Phys. Rev. B* 46 **(1992)** 7808.

[Joh89] D. Johannsmann, *J. Appl. Phys.* 89 **(2001)** 6356.

[Joh99] D. Johannsmann, *Macromol. Chem. Phys.* 200 **(1999)** 501 .

[JP01] N.R. Jana, T. Pal, *Indian J. Chem. A 40 (4)* **(2001)** 403.

[KHC95] L. Kwanghee, A. J. Heeger, Y. Cao, *Synth. Met. 72 (***1995)** 25.

[KHF02] D. Kuckling, M.E. Harmon, C.W. Frank, *Macromolecules* 35 **(2002)** 6377.

[KMK+02] M. Kreiter, S. Mittler, W. Knoll, J.R. Sambles, *Phys. Rev. B* 6512 **(2002)** 5415

[KMT00] P. Krysinski, M.R. Moncelli, F. Tadini-Buoninsegni, *Electrochim. Acta* 45 (**2000)** 1885.

[Kno97] W. Knoll, in: *Handbook of Optical Properties*, R. E. Hummel, P. Wißmann (eds.) Vol II, **(1997)** 373.

[Kno98] W. Knoll, *Annu. Rev. Phys. Chem.* 49 (**1998)** 569.

[Kno91] W. Knoll, MRS Bulletin 16 **(1991)** 29.

[KSC91] J. Krim, D.H. Solina, R. Chiarello, *Phys. Rev. Lett. 66* (**1991)** 181.

[KVW02] D. Kuckling, C.D. Vo, S.E. Wohlrab, *Langmuir* 18, **(2002)** 4263.

[KYT84] T. Kobayashi, H. Yoneyama, H. Tamura, *J. Electroanal. Chem.* 161 (**1984)** 419.

[KYT84] T. Kobayashi, H. Yoneyama, H. Tamura, *J. Electroanal. Chem.* 177 (**1984)** 293.

[LC84] C. Lu, A. W. Czanderna (edts.), *Applications of Piezoelectric Quartz Crystal Microbalances*, Elsevier, Amsterdam **(1984)**.

[Lek78] J. Lekner, *Theory of Reflection*, Kluwer Academic Publishers Group, Dordrecht **(1987).**

[Lew93] L.N. Lewis, *Chem. Rev. 93* (**1993)** 2693.

[Li97] Y. Li J.Electroanal.Chem. 433 (**1997**) 181.

[Lid93] D.R. Lide, Ed. *CRC Handbook of Chemistry and Physics*, 74th ed.; 1993-1994.

[LMJ00] A. Laschitsch, B. Menges, D. Johannsmann, *Appl. Phys. Lett.* 77 **(2000)** 2252.

[LSA+02] J. Lukkari, M. Salomäki, T. Ääritalo, K. Loikas, T. Laiho, and J. Kankare, Langmuir 18 **(2002)** 8496.

[LW95] Z. Lin, M.D. Ward, Anal. Chem. 67, **(1995)** 685.

[LZF94] D. Ljerka, M. Zoran, K. Franjo, *J. Polym. Sci.*, 32 **(1994)** 105.

[Mac97] A. G. MacDiarmid, *Synth. Met.* 84 (**1997)** 27.

[MCR+87] A. G. MacDiarmid, J. C. Chiang, A. F. Richter, A. J. Epstein, *Synth. Met., 18* (**1987)** 285.

[MCW97] S. Mu, C. Chen, J. Wang, *Synth. Met.* 88 (**1997)** 249.

[MF03] J. C. Munro and C.W. Frank, Macromolecules 37 **(2004)** 925.

[MFR93] S. J. Martin, G. C. Frye, A. Ricco, J. Anal. Chem. 65 **(1993)** 2910.

[MMS+85] A. G. MacDiarmid, S. L. Mu, N. L. D. Somarisi, W. Mu, *Mol. Cryst. Liq. Cryst. 121* **(1985)** 187.

[MMG+85] X. Mai, R.; Moshrefzadeh, U. J. Gibson, G. I. Stegeman, C. T. Seaton, Appl. Opt. 24 **(1985)** 3155.

[MSD+01] R.A. McAloney, M. Sinyor, V. Dudnik, M.C. Goh, Langmuir, 17 **(2001)** 6655

[MSR93] S.J. Martin, G.C. Frye, A.J. Ricco, *Anal. Chem.* 65 **(1993)** 2910.

[Muz73] R.A.A. Muzzarelli, Natural Chelating Polymers. Pergamon Press, New York, **(1973)**.

[Muz88] R.A.A. Muzzarelli, Carbohydr. Polym. 8 **(1988)** 1.

[MWM+04] C. Monteux, C.E. Williams, J.Meunier, O.Anthony, and V. Bergeron Langmuir 20 **(2004)** 57.

[MXM95] Y. Min, Y. Xia, A. G. MacDiarmid, A. Epstein, *J. Synth. Met.* 69 (**1995)** 159.

[NAS+95] R. Nyffenegger, E. Ammann, H. Siegenthaler, O. Haas, *Electrochim. Acta* 40 (**1995)** 1411.

[OB87] D. Orata, D. A. Buttry, *J. Am. Chem. Soc*. 109 (**1987)** 3574.

[PCB83] J.W.Park, K.-H.Choi, Bull. Korean Chem. Soc. 4 **(1983)** 68.

[PLH+01] C. Picart, Ph.Lavalle, P. Hubert, F.J.G. Cuisinier, G. Decher, P. Schaaf, and J.-C. Voegel Langmuir, 17 **(2001)** 7414

[PM01] K. Prasad, N. Munichandraiah, Synth. Met. 123 **(2001)** 459.

[PM02] K. Rajendra Prasad and N. Munichandraiahz, *Electrochem. and Solid-State Lett.* 12 **(2002)** 271.

[Poc78] I. Pockrand, *Surf. Sci.* 72 **(1978)** 577.

[PWR+03] M. A. Plunkett, Z.Wang, M.W. Rutland, D. Johannsmann, Langmuir 19 (17) **(2003)** 6837.

[RD89] M. Rinaudo, A. Domard, in: G. Skjak-Braek, T. Anthonsen, P. Sandford (Eds.), Chitin and Chitosan, Elsevier Applied Science, London, **(1989)**.

[RK88] B. Rothenhaeuser, and W. Knoll, J. Opt. Soc. Am. B5, **(1988)** 1401.

[RED+00] J. Ruths, F. Essler, G. Decher, H. Riegler, Langmuir, 16 **(2000)** 8871.

[RGO97] J. Rodriquez, H.J. Grande, T. F. Otero, Applications of Polymers.In Handbook of Organic ConductiVe Molecules and Polymers: Conductive Polymers: Synthesis and Electrical Properties; Nalwa, H. S., Ed.; John Wiley & Sons Ltd: New York, 1997; Vol. 2, Chapter VI, pp 457-460.

[RKB+98] O. Raitman, E. Katz, A. Bueckmann, I. Willner, *J. Am. Chem.Soc. 124*, **(2002)** 6487.

[Ros88] J.F. Rosenbaum, *Bulk Acoustic Wave Theory and Devices*, Artech House (**1988**), 376.

[RSW98] M.A. Rampi, O.J.A. Schueller, G.M. Whitesides, *Appl. Phys. Lett.* 72 (**1998)** 1781.

[RSG01] M. Ruths, S.A. Sukhishvili, S. Granick, J. Phys.Chem. B 105 **(2001)** 6202.

[Sau59] G. Sauerbrey, *Z. Phys*. 155 (**1959)** 206.

[Sau64] G. Sauerbrey, *Arch. Elektrotech. Übertragung* 18 **(1964)** 617.

[SB93] T.W. Schneider, D.A. Buttry, *J. Am. Chem. Soc. 115* (**1993)** 12391.

[SBE+87] S. Stafstrom, J. L. Bredas, A. J. Epstein, H. S. Woo, D. B. Tanner, W. S. Huan, A. G. MacDiarmid, *Phys. Rev. Lett.* 59 (**1987)** 1464.

[Sch90] R. Schumacher, *Angew. Chem., Int. Ed. Engl.* 29 **(1990)** 329.

[Sch92] H.G. Schild, *Prog. Polym. Sci.* 17 **(1992)** 163.

[Sch92] G. Schmid, *Chem. Rev. 92* (**1992)** 1709.

[SG02] J. Stejskal, R. G. Gilbert, *Pure Appl. Chem.* 74 (**2002)** 857.

[SKH+99] E. Smela, M. Kallenbach, J. Holdenried, J. Microelectromech. Syst. 8 (1999) 373.

[SS94] T. Sun, K. Seff, *Chem. Rev. 94* (**1994)** 857.

[TBL^{+}03] S. Tian, A. Baba, J. Liu, Z. Wang, W. Knoll, M. Park, R. Advincula, Adv.Funct. Mater. 13 (**2003**) 473

[Thu84] R.N. Thurston, in C. Truesdell (edt.) *Mechanics of Solids*, vol. 4, chap. 36, Springer-Verlag, Heidelberg **(1984).**

[THZ^{+}98] J. Thome, M. Himmelhaus, M. Zharnikov, M. Grunze, *Langmuir 14* (**1998)** 17435.

[TKK80] A. Tadjeddine, D. M. Kolb, R. Kötz, *Surf. Sci.* 101 (**1980)** 277.

[WGM87] G. Wilkinson, R.D. Gillard, J.A. Mccleverty, *Comprehensive Coordination Chemistry*, Vol. 1 (Pergamon Press, Oxford, England) (**1987)**.

[WKJ03] Z. Wang, D. Kuckling, D. Johannsmann, Soft Materials 1 **(2003)** 353.

[YFL00] E. B. Yousfi, J. Fouache, D. Lincot, *Appl. Phys. Lett. 153 (***2000)** 223.

[ZCC88] G. Zotti, S. Cattarin and N. Comisso, *J. Electroanal. Chem.,* 239 **(1988)** 387.

[ZD97] A. Zimmermann, L. Dunsch, *J. Molecular Structure* 410 (**1997)** 165.

[ZGS86] F. Zaera, A.J. Gellman, G.A. Somorjai, *Acc. Chem. Res. 19* (**1986)** 24.

[ZRH02] H. Zheng, M.F. Rubner, and P.T. Hammond, Langmuir 18 **(2002)** 4505.

[ZPG^{+}02] M. Zhou, M. Pagels, B. Geschke, J. Heinze; *J. Phys. Chem. B 106* **(2002)** 10065.

Publications:

The following papers were published during my doctoral education period:

1 Bund, A.; Baba, A.; Berg, S.; Johannsmann, D.; Luebben, J.; Wang, Z.; Knoll, W. Combining Surface Plasmon Resonance and Quartz Crystal Microbalance for the in Situ Investigation of the Electropolymerization and Doping/Dedoping of Poly(pyrrole) *J. Phys. Chem. B. ;* 107**(28);** pp 6743-6747; **2003**;

2 Akira Baba, Shengjun Tian, Fernando D. Stephani, Chuanjun Xia, Z. Wang, R.Advincula, D. Johannsmann and W.Knoll Electropolymerization and Doping / dedoping Properties of Polyaniline Thin Films as Studied by Electrochemical Surface Plasmon Spectroscopy and by Quartz Crystal Microbalance J.Electroanal. Chem. 562 (1): 95-103 JAN 15 2004

3 Shengjun Tian, Akira Baba, Jianyun Liu, Zhehui Wang, Wolfgang Knoll, Mi-Kyoung Park, and Rigoberto Advincula Electroactivity of polyaniline mutilayer films in neutral solution and their electrocatalyzed oxidation of □-nicotinamide adenine dinucleotide Advanced Functional Materials, 13, No. 6, June. Pp.473 – 479, 2003.

4 Mark A Plunkett, Zhehui Wang, Mark W Rutland, Diethelm Johannsmann Adsorption of pNIPAm layers on hydrophobic gold surfaces, measured in situ by QCM and SPR *19*(17) pp 6837 - 6844; Aug19 2003, Langmuir.

5 Zhehui Wang, Dirk Kuckling, Diethelm Johannsmann Temperature effect of pNIPAm Film on gold surfaces measured in situ by QCM and SPR Soft Materials **1**, 353 (2003).

6 A. K. Aliganga, Z. Wang, S. Mittler, Chemical Vapor Deposition of Mercury on Alkanedithiolate Self-Assembled Monolayers, J. Phys. Chem. B 2004

Lebenslauf

Persönliche Informationen

Name:	Zhehui Wang
Adresse:	Marktstr.35, 38678 Clausthal-Zellerfeld
Geburtsdatum:	04.11.1970
Geburtsort:	Shandong, China

Schulausbildung

09.1976 – 07.1981 Grundschule, Xiaolizhuang

09.1981 – 07.1984 Grundstufe Mitteschule, Luquantun

09.1984 – 07. 1987 Oberstufe Mitteschule Nr. 1, Wucheng

Hochschulausbildung

---

09. 1987 – 07.1992 Qingdao Institute of Chemical Technology

1992 Bachelor's Degree: Plastics Engineering

09.1992 – 07.1993 Beijing University of Aeronautics and Astronautics

08.1993 – 03.1995 Institute No. 43, China 4th Academy of Aerospace

1995 Master's Degree: Composite Materials

09.1999 – 07.2000 Guangzhou Institute of Foreign Studies

08.2000 – 10.2002 Max-Planck-Institut für Polymerforschung, Mainz

11.2002 – heute Technische Universität Clausthal

Berufserfahrung

---

04. 1995 – 08.1999 Institute No. 43, China 4th Academy of Aerospace Industry

1997 Title of Engineer